SPACE RESEARCH COORDINATION CENTER

ROCKET INVESTIGATION OF THE AURORA BOREALIS:

SOME OF ITS PROMINENT OPTICAL FEATURES AND ITS ION COMPOSITION

BY

TRUMAN DAVID PARKINSON

DEPARTMENT OF PHYSICS

SRCC REPORT NO. 97

UNIVERSITY OF PITTSBURGH
PITTSBURGH, PENNSYLVANIA

29 MAY 1969

The Space Research Coordination Center, established in May, 1963, has the following functions: (1) it administers predoctoral and postdoctoral fellowships in space-related science and engineering programs; (2) it makes available, on application and after review, allocations to assist new faculty members in the Division of the Natural Sciences and the School of Engineering to initiate research programs or to permit established faculty members to do preliminary work on research ideas of a novel character; (3) in the Division of the Natural Sciences it makes an annual allocation of funds to the interdisciplinary Laboratory for Atmospheric and Space Sciences; (4) in the School of Engineering it makes a similar allocation of funds to the Department of Metallurgical and Materials Engineering and to the program in Engineering Systems Management of the Department of Industrial Engineering; and (5) in concert with the University's Knowledge Availability Systems Center, it seeks to assist in the orderly transfer of new space-generated knowledge in industrial application. The Center also issues periodic reports of space-oriented research and a comprehensive annual report.

NGL-39-011-002

The Center is supported by an Institutional Grant (~~NsG-416~~) from the National Aeronautics and Space Administration, strongly supplemented by grants from the A. W. Mellon Educational and Charitable Trust, the Maurice Falk Medical Fund, the Richard King Mellon Foundation and the Sarah Mellon Scaife Foundation. Much of the work described in SRCC reports is financed by other grants, made to individual faculty members.

ROCKET INVESTIGATION OF THE AURORA BOREALIS: SOME OF ITS PROMINENT OPTICAL FEATURES AND ITS ION COMPOSITION

by

Truman David Parkinson ,

B. S. Carnegie Institute of Technology, 1964

Submitted to the Graduate Faculty of Arts and Sciences in partial fulfillment of the requirements for the degree of Doctor of Philosophy

University of Pittsburgh

1969

ROCKET INVESTIGATION OF THE AURORA BOREALIS: SOME OF ITS PROMINENT OPTICAL FEATURES AND ITS ION COMPOSITION

Truman David Parkinson, Ph.D.

University of Pittsburgh, 1969

Analysis of data from a series of three sophisticated Aerobee rocket experiments flown into auroral displays has yielded much information concerning the excitation mechanisms of several optical emissions. Laboratory measured cross sections for the N_2^+ (0-0) first negative band, its observed volume emission rate, and measured secondary electron spectra allow calculation of the electron fluxes responsible for the N_2 first positive bands, the O_2^+ first negative bands, and the OI green line at 5577Å. The molecular emissions can be accounted for in terms of direct electron impact excitation from the appropriate neutral molecule. The classical source of the green line, direct electron impact excitation of O, is shown inadequate. Dissociative excitation of O_2 (with an average cross section of 6-10 x $10^{-17}cm^2$) and dissociative recombination of O_2^+, each dominant in its own region, are capable of producing the green line. Further confirmation of this dual source comes from a measurement of the quenching of the $O(^1D)$ state as indicated by the OI red line at 6300Å, and from the phase and amplitude relations between the N_2^+ (0-0) band and the green line. Measurement of the ion composition shows the need of a reaction which, in an aurora, removes O_2^+ and produces NO^+. A value of 4 x $10^{-13}cm^3/sec$ for the reaction rate for O_2^+ on vibrationally excited N_2 is capable of providing the needed channel, if vibrational temperatures in excess of 1200°K are not needed.

PREFACE

The author is deeply indebted to Professor E. C. Zipf for his friendship, guidance, and encouragement throughout this program. The author is also indebted to Professor T. M. Donahue for many usful discussions. Dr. K. A. Dick, Mr. W. G. Fastie, and Dr. J. P. Doering of Johns Hopkins University have also contributed valuable discussion and data. Support for the experiments provided by the Sounding Rocket Branch of Goddard Space Flight Center and the Churchill Research Range is also greatly appreciated. Design and construction of the payload packages has been well executed by the Ray Lee Machine Company of Baltimore, Maryland. Finally, the author would like to thank his wife, Margaret, for her tolerance of his extended field trips and for assistance in preparation of this manuscript.

TABLE OF CONTENTS

1.0 INTRODUCTION

The aurora borealis has a long record of observation. There has been much written on this subject in the scientific literature since the seventeenth century.[1] It was not until 1869 that Ångström[2] published the first auroral spectra and found the prominent green line. In 1923, Babcock[3] performed the first accurate determination of its wavelength in a study of the airglow. McLennan and Shrum[4] showed the green line came from the metastable ^1S state of the oxygen atom. Vegard[5] identified the negative bands of molecular nitrogen about 1913. Almost all of the spectral features have now been identified.

Now that the identification of the spectral features is essentially complete, attention has been turned to the identification of the sources of excitation. Much theoretical work in this area was done by Bates[6] for the nitrogen bands and by Seaton[7-10] for forbidden transitions.

Only recently have these mechanisms been investigated in the emitting regions of the aurora by sounding rockets. The experiments resulting in this dissertation originated in an investigation of the detailed sources of the auroral green line at 5577Å emitted by the oxygen atom in the metastable ^1S state. Historically, direct electron impact excitation of ground state atomic oxygen [7-9] has been invoked to explain this emission. As a consequence of this research, two separate mechanisms, dissociative excitation of O_2 and dissociative recombination of O_2^+, each dominant in its own region, explain this most prominent feature of the visible aurora. A complementary measurement of the altitude profile of the oxygen red line (6300Å) in an IBC class II^+ aurora has

invalidated Seaton's[10] analysis of the excitation and collisional deactivation of the $O(^1D)$ state. This removes a discrepancy of several orders of magnitude in the quenching rate which had existed between dayglow[11] and auroral observations.

Recent laboratory measurements of the inelastic electron cross sections for excitation of the (0-0) band of the first negative system of nitrogen have allowed normalization of the electron spectra measured as part of this experiment. From the (0-0) band emissions and the measured electron energy spectra, appropriate exciting fluxes have been determined. Discussion includes the first and second positive systems of molecular nitrogen and the first negative system of the molecular oxygen ion. Data will be presented in support of the electron impact excitation model for these emission features.

The ion composition was also measured for a weak aurora. The excessive NO^+ density is discussed, as well as the expected ion composition based on the ionization rate determined from the (0-0) band emission and the most recent reaction rates as measured in the laboratory. A reaction which in an aurora removes O_2^+ and enhances NO^+ is necessary to explain the ion distribution observed.

2.0 EXPERIMENT

2.1 Payload Development

W. G. Fastie of Johns Hopkins University flew several ultraviolet spectrometer payloads into auroras during the early 1960's. With them, he observed the LBH bands of nitrogen, Lyman α, and the resonance lines of atomic oxygen and measured their altitude profiles.[12-15]

In 1966, he invited several other experimenters to put instruments on his rocket. The payload was built around Fastie's half meter ultraviolet spectrometer. An extreme ultraviolet photometer, two continuous reading photometers observing visible features, and a filter wheel photometer for additional visible features looked forward. A secondary electron spectrometer[16] and a pitch angle electron flux detector were located on a pair of deployable booms. A primary electron spectrometer was also carried.

In 1967, the continuous photometers in the visible were removed, and an up-down photometer added.[17] This unit looked at the 2972Å transauroral line of oxygen and several bands of nitrogen. At this wavelength, there is no ground albedo so that the sum of the up-signal and the down-signal at any time indicates the state of the aurora. By using a flipping mirror and only one filter and photomultiplier tube, the summation signal is independent of any absolute calibration. To a first approximation, this experiment tells how steady the observed aurora was during the flight. Further pertinent discussion of the up-down photometer is in Section 3.5.

After the 1967 flight, it was obvious that the number of experimenting groups had to be reduced to ease the problems of design, integration, and preparation. The 1968 rocket became a joint effort of the Johns Hopkins group and the Pittsburgh group. The Johns Hopkins group flew four experiments: primary and secondary electron spectrometers, a far ultraviolet filter wheel photometer, and an improved up-down photometer. The Pittsburgh group flew a three channel continuous reading photometer and an ion mass spectrometer.

The Aerobee 150 rocket was the vehicle used for all the experiments. It can carry payloads of approximately 260 pounds to 170 km, well above most auroral emissions. The maximum axial acceleration is 12 g, a gentle ride compared with the 35 or more g of the various Nike rockets. The comparatively gentle ride eases design problems and increases reliability of the instruments. The 16-inch diameter of the rocket allows considerable frontal area for necessary forward facing experiments. Two FM-FM telemeters can be carried allowing up to 27 full-time analogue data channels, and a commutator for monitor purposes. A DOVAP transponder can be carried for improved tracking during the flight. The biggest drawbacks to use of the Aerobee are the inconvenience of a liquid fueled rocket, the large group of field personnel attendant, and the greater cost.

Figure 1 shows the layout of the 1968 payload.

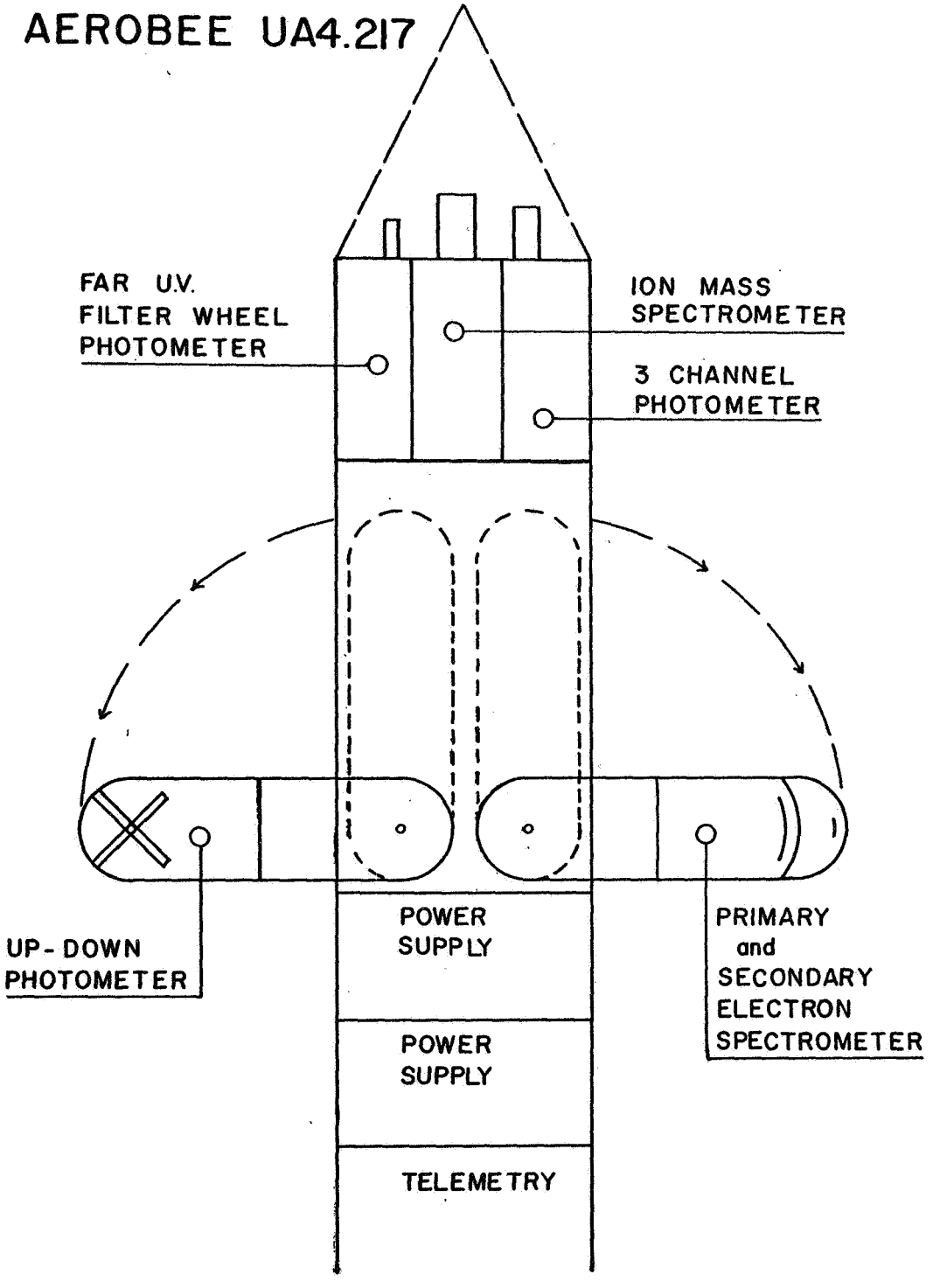

Figure 1. Schematic of the 1968 experimental payload. The tip and doors were ejected at about 70 km. The booms were deployed shortly thereafter.

2.2 The University of Pittsburgh Photometers

A three channel photometer was part of the University of Pittsburgh's contribution to the 1968 payload. It looked at the OI(^1S-^1D) forbidden transition at 5577Å, the $N_2^+(B^2\Sigma_u^+ - X^2\Sigma_g^+)$ first negative (0-0) band at 3914Å, the $N_2(B^3\Pi_g - A^3\Sigma_u)$ first positive (5-2) band centered about 6685Å.

Figure 2 shows a cross section of the photometer unit. All three photometers were in the same rectangular, pressurized housing supported on the front plate of the rocket. The Hruska VS-5 high voltage supplies, VT series electrometers, and NI slave amplifiers were also contained in the housing. Figure 3 shows the circuit for one of the three photometers. Each unit returned two channels of data, a 1x from the electrometer and a 10x from the slave amplifier. The slave amplifier took the first half volt of the 1x signal and multiplied it by 10. Each amplifier was zener diode limited to prevent overloading of the telemeters. A monitor of the high voltage was also telemetered.

Appendix A presents a detailed discussion of interference filter photometers. The theoretical sensitivities, noise levels, and absolute sensitivities for the flight photometers are listed in Table I. As originally conceived, a gain changing circuit was to have been added. It automatically switched the high voltage when the signal registered either too high or too low. Three operating ranges were provided. Pre-flight time limitations caused this system to be abandoned.

The photometer performed very well except for some zero drift problems closely related to the payload temperature. It was a very

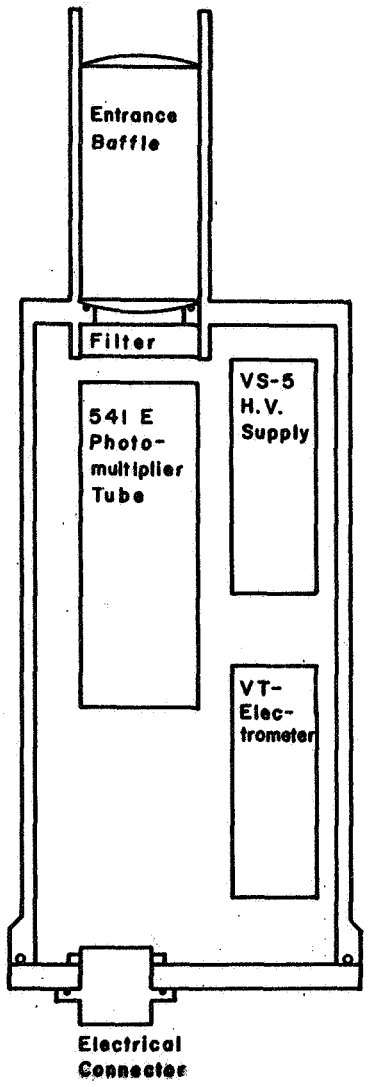

Figure 2. Schematic cross section of the three channel photometer flown in 1968.

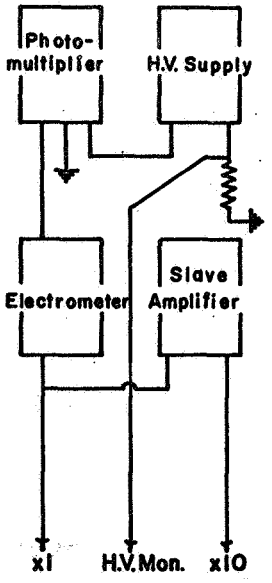

Figure 3. Schematic of the electronics of one channel of the three channel photometer.

TABLE I. Operational parameters of the 1968 photometer.

Nominal wavelength	5577	3914	6685
Calibrated sensitivity, full scale, x 1 (kR)	120	62	12.5
Calculated sensitivity, full scale, x 1 (kR)	99	87	6.2
S/N at 1 per cent full scale, x 1	19	19	3.6

TABLE II. Operational parameters of the 1967 filter wheel photometer.

Nominal wavelength	3914	5279	5577	5618	6685
Calibrated sensitivity, full scale, x 1 (kR)	61.1	13.8	58.6	17.8	24.8
Calculated sensitivity,* full scale, x 1 (kR)	57.2	13.6	59.2	18.1	24.7
S/N at 1 per cent full scale, x 1	1.1	1.1	1.1	1.1	1.1

*The calculated sensitivities for this photometer agree much better with the absolute sensitivites than was the case for the unit described by Table I. This is because there was time to measure all the appropriate parameters for the components and deviations from manufacturers specifications were found. Practical experience with these photomultiplier tubes shows that occasionally the gain deteriorates as the tube ages; this may explain the differences between the calculated and calibrated sensitivities shown in Table I.

decided improvement over the filter wheel photometers flown by the University of Pittsburgh on the 1966 and 1967 experiments.

The previously flown filter wheel photometers were compromises as all filter wheel photometers must be. A geneva movement rotated a five position filter wheel between a simple baffle aperture tube and the photomultiplier tube. It spent roughly 14 percent of each cycle stationary in each position. Once the gain is set for the least sensitive wavelength, usually in the red, the only way to adjust sensitivities is through decreasing the field apertures carried with the filters in the wheel. This, of course, greatly decreases the signal to noise ratio, not at all desirable, but unavoidable. The high voltage monitor returns an index of the filter wheel position. Table II gives the sensitivities of the 1967 unit and calculated signal to noise ratios. These are clearly much lower than those of the 1968 units caused in part by the compromise nature of the unit and part by the lack of lenses in the aperture system. The use of lenses alone would have increased the signal to noise ratio by a factor of four.

2.3 The University of Pittsburgh Ion Mass Spectrometer

A quadrupole ion mass spectrometer, designed by E. C. Zipf, was the major addition to the 1968 payload. It was designed to measure the densities of ions from mass 3 to mass 40. The properties of quadrupole mass spectrometers are discussed by Woodward and Crawford,[18] Narcisi and Bailey,[19] Mosharrafa and Oskam,[20] and Paul et al.[21] A brief outline follows.

An ideally hyperbolic potential of the form

$$\phi = \phi_o \frac{x^2-y^2}{r_o^2} \tag{1}$$

is generated by four appropriately dimensioned parallel round rods equally spaced on a cylinder about the instrumental axis (Figure 4). Opposite pairs of rods are electrically connected. A voltage consisting of a DC portion and an RF portion of the form

$$\phi_o = U + V \cos \omega t \tag{2}$$

is applied to the poles.

The equations of motion in the x and y directions are

$$\frac{d^2x}{d\gamma^2} + (a + 2q \cos 2\gamma)\, x = 0 \tag{3}$$

and

$$\frac{d^2y}{d\gamma^2} - (a + 2q \cos 2\gamma)\, y = 0 , \tag{4}$$

where $\gamma = \frac{\omega t}{2}$, $a = \frac{8e\ U}{m\ r_o^2\ \omega^2}$, and $q = \frac{4e\ V}{m\ r_o^2\ \omega^2}$. These equations are of the normal form of the Mathieu equation,

$$\frac{d^2x}{d\gamma^2} + (a - 2q \cos 2\gamma)\, x = 0 \tag{5}$$

Solutions to the Mathieu equation are stable or unstable depending on the values of a and q. In Figure 5, the stable region of interest is sketched in the a-q plane.[20] A line of constant a/q, and hence U/V,

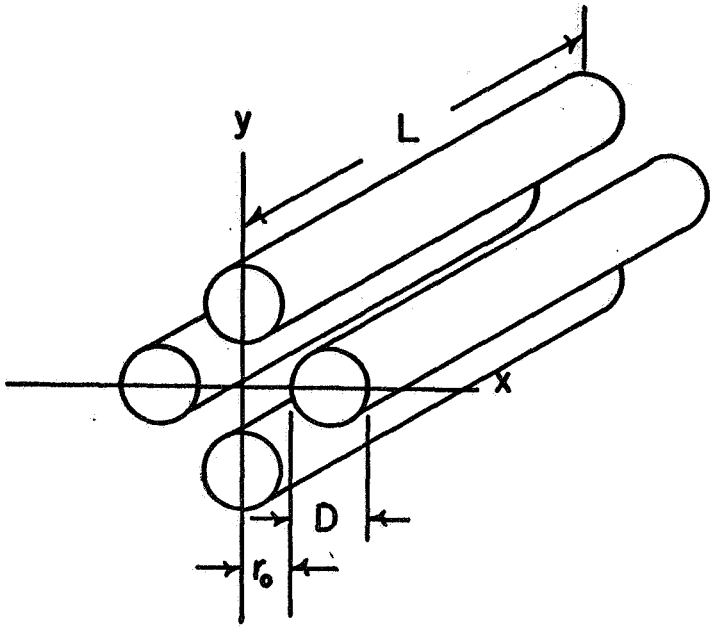

Figure 4. The four rods which produce the hyperbolic field of the quadrupole mass spectrometer.

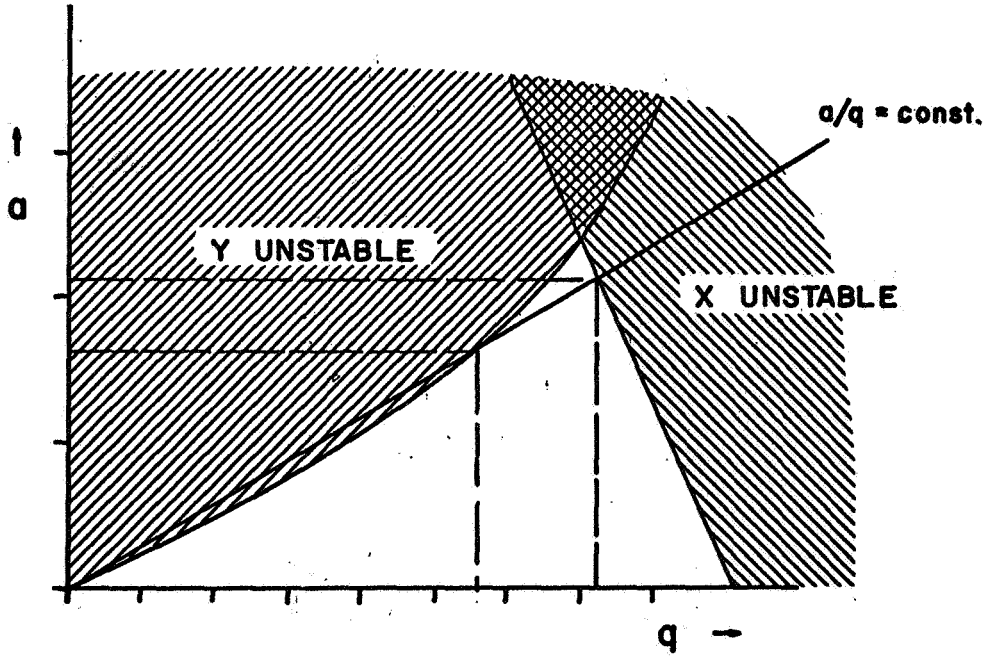

Figure 5. A sketch in the a-q plane of the stable region of operation of the quadrupole mass spectrometer.[20]

is also shown. Masses for which a and q are in the region of stability are transmitted. As the slope of the a/q constant line is increased, the permissable values of a and q are decreased. This decreases the mass range transmitted and increases the resolution. For infinite resolution, U/V should be 0.16784.[18] Two methods are practical for scanning a mass spectrum. While keeping U/V constant, either the frequency ω or the voltage amplitudes U and V may be programmed to sweep a desired mass range.

Table III lists the parameters used in the 1968 unit. Figure 6 is a block diagram showing the basic circuit elements of the unit.

The four stainless steel rods were held in a stainless steel housing by nylon bushings. The housing was kept at -9.1 volts with respect to the rocket shell. In front of the injection aperture was a stainless steel ring with a stainless steel screen to give a draw-in potential between itself and the front aperture. This grid was kept at -2.58 volts. The screen was carefully centered so that the center of a hole in the square mesh was on the axis of the instrument. In this way, the most symmetric field, approximating a parallel field, was to be had between the grid and the injection aperture.

Behind the exit aperture was a Bendix Channeltron detector. Because of its ultraviolet sensitivity, it was placed so that it could not see outside its chamber. The -1340 volts applied to the cathode end provided an excellent draw-in potential for those ions transmitted. A 200 volt collector bias was used between the Channeltron anode and the stainless steel collector. An Hruska 250-25-3 electrometer recorded

TABLE III

Design parameters of the quadrupole mass spectrometer.

r_o	3.0 mm
Rod diameter	7.0 mm
Rod length	100 mm
Injection aperture diameter	0.5 mm

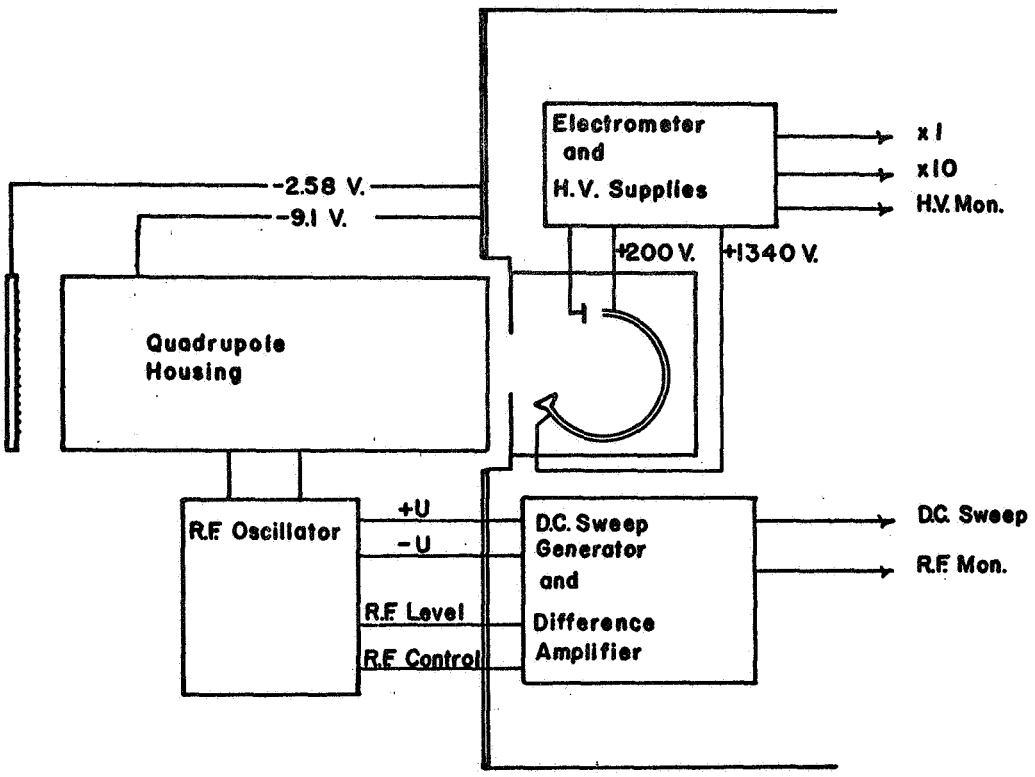

Figure 6. Circuit elements of the ion mass spectrometer.

into the 1x channel and a NI slave amplifier provided a 10x channel.

A sweep generator provided a sawtooth signal +U with a period of 1.7 seconds (Figure 7). The sweep signal was grounded for a short time at the beginning of each cycle so the total ion density could be measured. A mirror signal -U was also generated. A difference amplifier, sampling the RF amplitude V, caused that amplitude to follow the +U signal holding a constant ration.

Table IV gives the theoretical values of U, V, and $\Delta m/m$ for each mass seen. The absolute calibration for zero vehicle velocity is also given. Unfortunately, calibration was much more hurried than desirable. It was accomplished by means of an electron gun incorporated in a vacuum housing which fit over the quadrupole unit (Figure 8). This electron gun ionized the residual gas in the chamber.

The dominant ion found was 18^+ presumably from water vapor. Other ions seen during calibration contributed negligibly. The current density of ions in front of the grid was assumed constant over a sufficiently large region that the current density j could be written as

$$j = i / A \qquad (6)$$

where i was the current to the grid and A was the area of the grid. It was found that j was 10^{-8} amps/cm^2. Since only one ion was considered responsible, this immediately gave the ion flux $n\bar{v}$ equal to 6.3×10^{10}/cm^{2}sec. Assuming a velocity caused only by the 2.58 volt accelerating potential, the ion density was found to be 1.2×10^5 ions/cm^3. Thermal velocities are small compared to the velocity due to the accelerating grid.

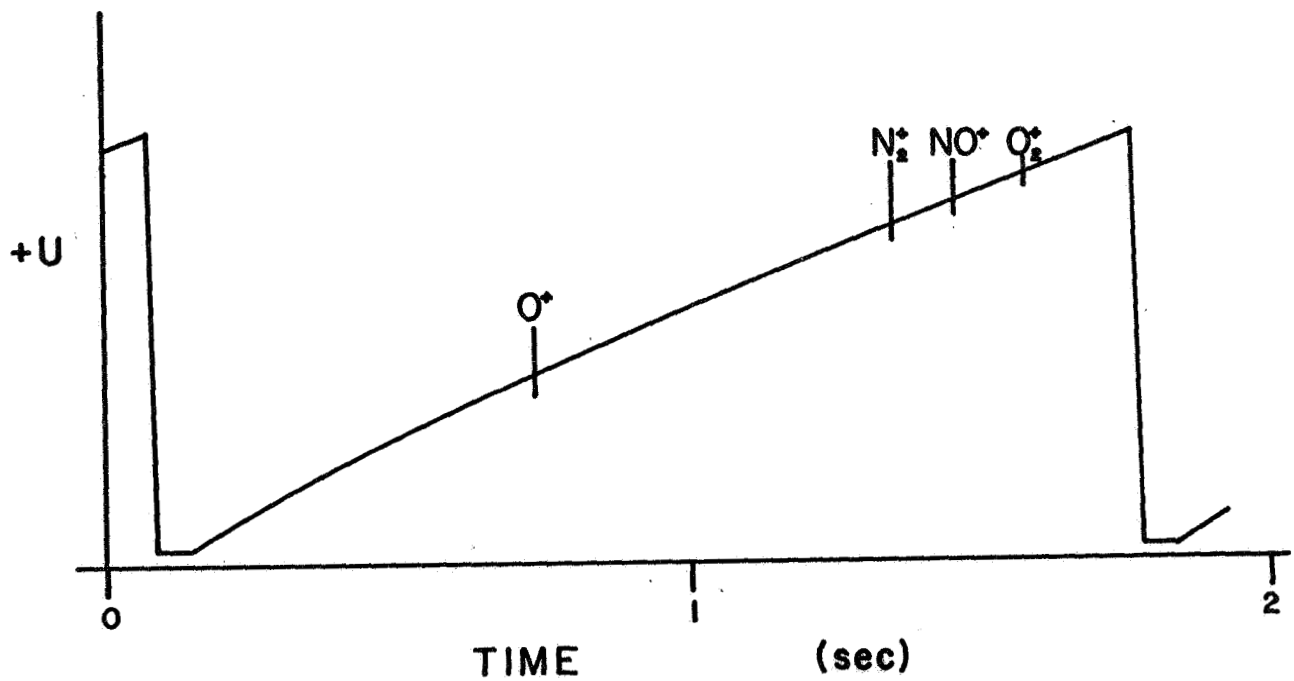

Figure 7. Sweep voltage +U generated by the ion mass spectrometer. Also indicated are positions where masses are expected.

TABLE IV.

Electrical parameters of mass spectrometer.

Mass (amu)	4	16	18	28	30	32
V (volts)	23.4	93.4	105	164	175	187
U (volts)	3.90	15.6	17.5	27.3	29.2	31.2
$\Delta m/m^{18}$	.01	.01	.01	.01	.01	.01

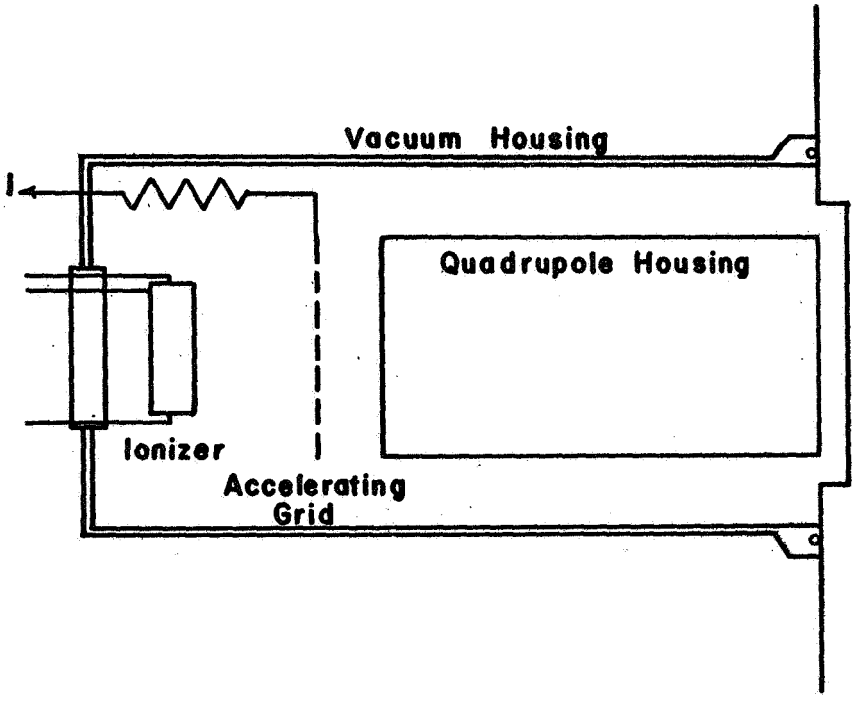

Figure 8. Schematic of calibration set up and vacuum housing.

For the above density, the Channeltron output was 8.4×10^{-10} amps. This gave the 10x channel a sensitivity of 5.7×10^{4} ions/cm^3/volt, at mass 18. The product $n\bar{v}$ is a constant. So long as the operating parameters of the ion mass spectrometer remain constant, the residual density n(X) (for any species X) can be calculated if the velocity V(X) is known. V(X) is the velocity of ion summed with the velocity of the rocket. The rocket velocity is a fair percentage of the ion velocity caused by the accelerating potential, especially for the heavier ions. Thus,

$$n(X) = 5.7 \times 10^{4} \; V(18) \; / \; \sqrt{2 \, U_{acc} \; /m(X) + V^2_{rocket}} \qquad (7)$$

gives the sensitivity of the unit for each mass, including the vehicle velocity dependence.

Experience gained in testing a similar unit constructed for the 1969 experiment has indicated two problems concerning the analysis of the data obtained in 1968. Between calibration and launch (two weeks), the electronics drifted; and an increase in resolution is clearly indicated by the spectra returned. This in itself would be all right, but the increase in resolution causes a decrease in transmission. This decrease is a nonlinear function of mass. Also, during the flight, changes in resolution cause the transmission for the molecular ions to continuously increase during flight. Figure 9 shows what is now believed to be the decrease in transmission during flight referenced to the transmission during calibration. Some of this change during flight may be due to vehicle velocity effects on the transmission.

The ion mass spectrometer performed reasonably well for a proto-

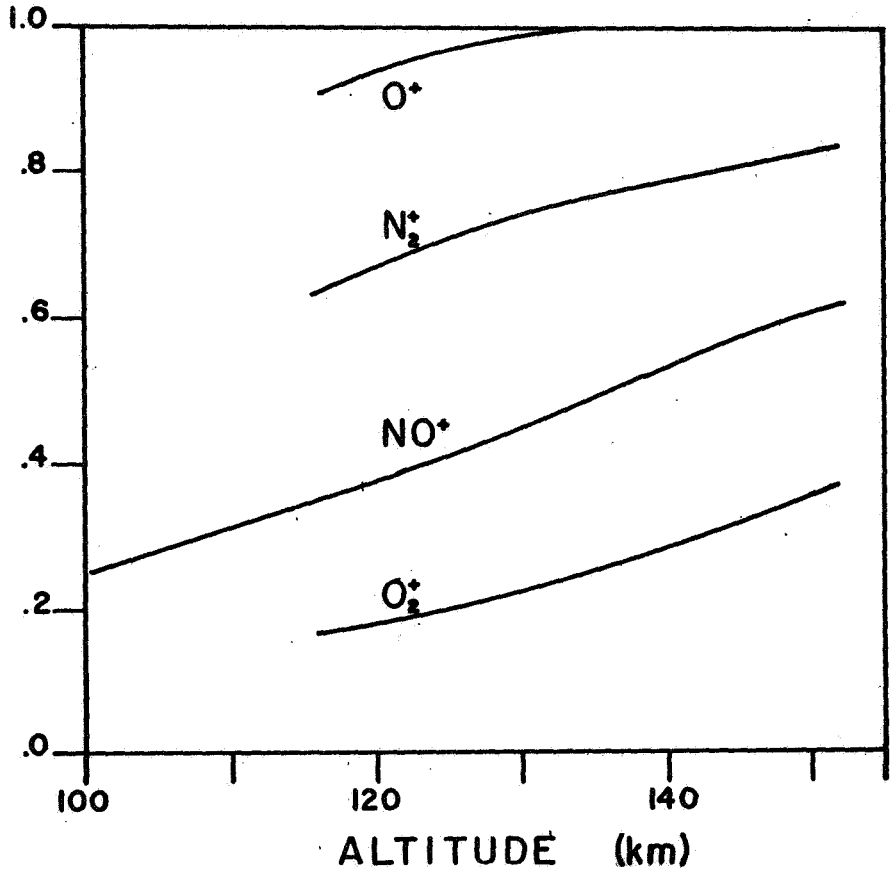

Figure 9. The post calibration decrease in transmission of the ion mass spectrometer plotted as a function of altitude.

type instrument. From the experience with this unit, several improvements have been made. The use of operational amplifiers has simplified many problems, especially those of temperature drifts and nonlinearities in the difference amplifier. The Channeltron worked, but laboratory experience of arcing at higher pressures than desired caused concern. This problem did not appear in flight; but the system was checked, and it was able to recover satisfactorily. Improved dynamic range would be a big help, and a rate meter has supplied the answer. A larger draw-in potential also appears advisable. The prototype did provide data on the upleg of the flight, but draw-in potential was insufficient for it to measure ion densities (except 4^+) once the vehicle was into the downleg.

2.4 Data Reduction

Extensive use of an IBM 7090 Computer and a Calcomp analog plotter has been made in reducing the data telemetered from the rockets. Replays of tapes recorded during the flight provide permanent records. Three or more channels of telemetered data are recorded on 12-inch paper by a CEC lightbeam oscillograph. Two pps and 100 pps timing from the tape appear on the edges of the record. Universal time can be easily determined from a BCD coding of the timing pulses. Constant reference lines from which signals can be measured are conveniently located on the record. Figure 10 shows a record for the filter wheel photometer flown in 1966. Figures 11 and 12 respectively show signals from the green line photometer and ion mass spectrometer flown in 1968.

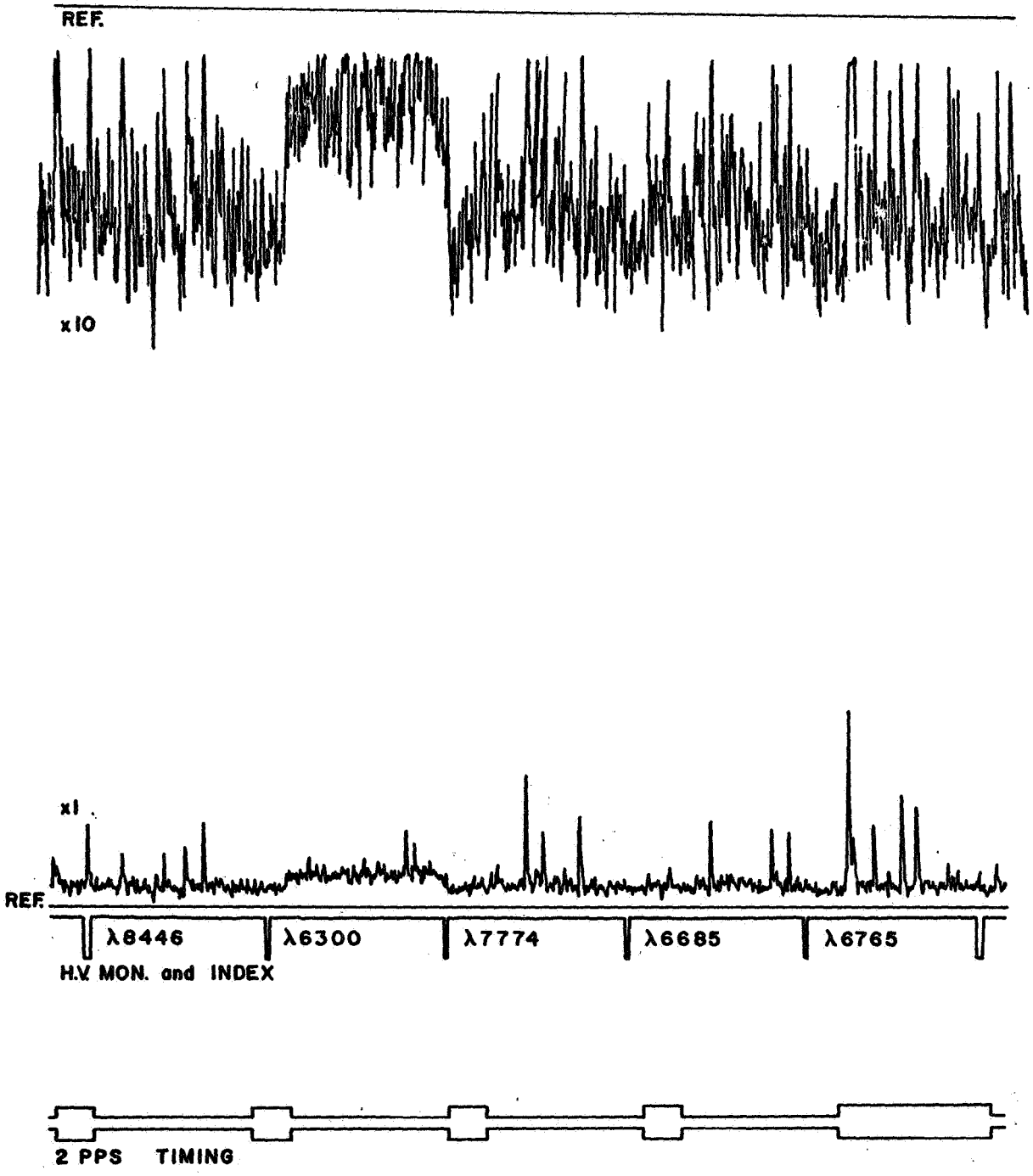

Figure 10. The 1966 filter wheel photometer data from a CEC recorder This section is near apogee. Note the strong λ6300 signal.

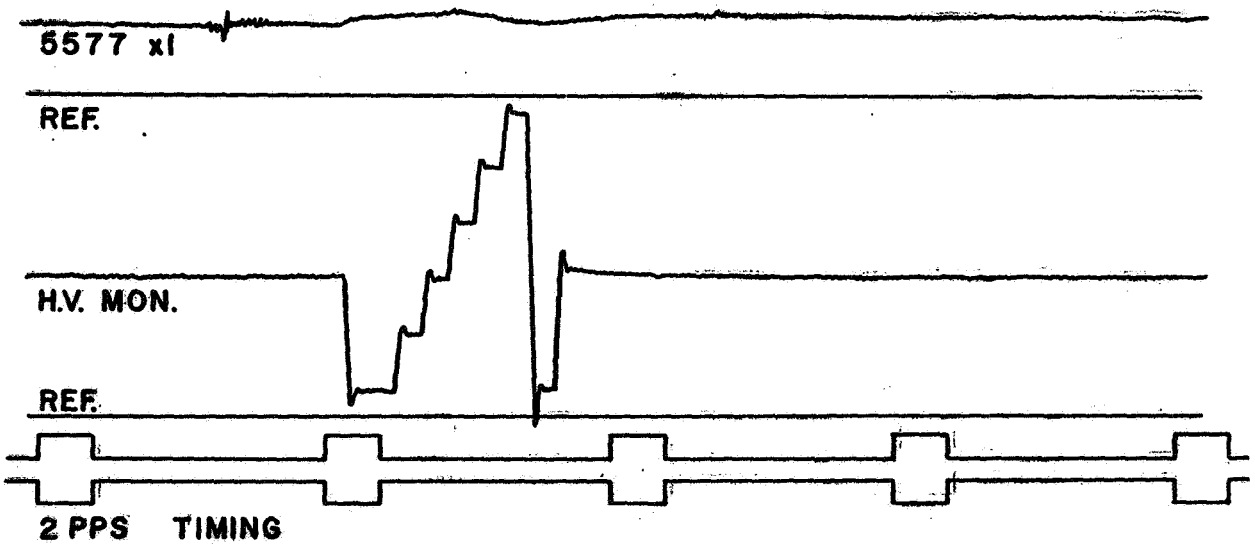

Figure 11. The 1968 green line photometer data from a CEC recorder. Notice the much improved signal to noise ratio. This is at tip eject. In-flight voltage calibration appears on bottom channel.

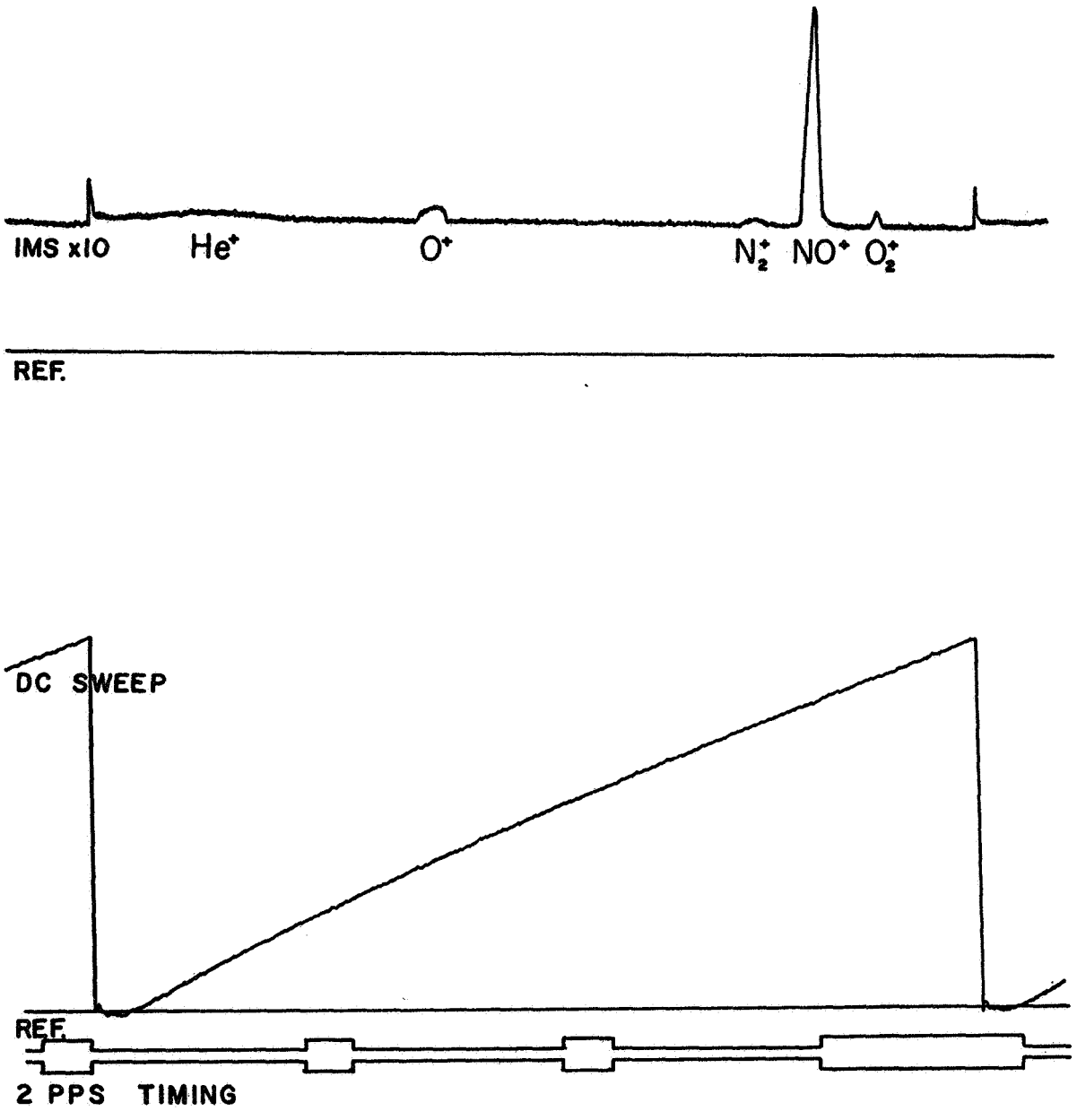

Figure 12. The 1968 IMS data at 130 km from a CEC recorder. This sweep shows the maximum N_2^+ signal seen.

For the filter wheel photometers of 1966 and 1967, an average level is drawn through the signal for each observing period. Midway through the period, the distance from the line to a reference line is measured. The universal time for the same midpoint is also recorded. The dark current level is determined at tip eject and is confirmed as often as possible when the filter wheel shifts positions. A check is also made at apogee.

There was a further complication in the 1966 unit. An extreme mechanical shock at rocket burnout disturbed the photocathode, causing a tremendous increase of the dark current. By tip eject twenty seconds later, the level was just back on scale but the dark current clearly did not stabilize until apogee. A time dependent expression for the dark current,

$$I_{DC} = A\, e^{-t/\tau 1} + B\, e^{-t/\tau 2} + C\, e^{-t/\tau 3} + D, \qquad (8)$$

was finally used to correct the raw data. The constants were determined from several reasonable dark current measurements throughout the flight. That this correction was reasonable can be seen from the behavior of the OI(λ6300) signal. Because of the quenching of the $O(^1D)$ state,[11] the λ6300 is expected to come from high altitudes. The raw data confirmed this expectation as the signal level for the λ6300 emission obviously remained high throughout the flight, while the other signals disappeared (Figure 10). Also, because of the 110 sec radiative lifetime of the $O(^1D)$ state, this signal is relatively immune to small, fast temporal variations. Adjustment for the dark current using Equation 8 showed the λ6300 signal to be symmetric on the upleg and the downleg, except for the very earliest portion of the

upleg where all signals imply insufficient correction. In addition, there is a small periodic variation of instrumental origin common to all signals measured by the filter wheel photometer. This variation is not seen in the signals from Miller and Fastie's independent photometers discussed below.

In the analysis of the continuous photometers, average signal levels are drawn and measured to a reference line. For the OI(λ5577) and N_2^+ING(λ3914) photometers of Miller and Fastie carried in the 1966 experiment, the data samples were taken at the same times as those of the OI(λ6300) channel of the filter wheel photometer. Dark current was referenced to tip eject, and its constancy confirmed at apogee.

For the 1968 photometers, the sample was taken midway between scans of the ion mass spectrometer. Dark current decreased during flight and a linear (in time) approximation, determined from levels at tip eject and apogee, was used for the dark current.

For the ion mass spectrometer, the height of each peak was measured relative to the base line along with the appropriate mass number and time.

Independent of Dick and Fastie, we made our own reduction of the 1968 up-down photometer. At each flip of the mirror, the upward looking signal and downward looking signal were measured with respect to the dark current level recorded as the mirror flipped and shuttered the entrance baffle. The time was also recorded.

In-flight voltage calibrations were examined and have been found constant to a few percent throughout the flight. All the above data, with appropriate absolute calibrations, have been put on IBM cards

and run through the computer. The computer generated absolute signal levels for each set of data. It also computed the altitude from the time determinations using the formula

$$Z(t) = Z_{max} - \frac{(6370 + Z_{max})}{2} \left[\cosh \left| \sqrt{\frac{2x0.009818x(6370)^2}{(6370 + Z_{max})^3}}\ t \right| - 1 \right] \quad (9)$$

This expression is second order gravity corrected (referenced to Z max). For the ion mass spectrometer, the vehicle velocity dependence was also included using $\frac{dZ(t)}{dt}$. Data was returned on lists, punched cards, and Calcomp analog plots. The plots were made with respect to both time and altitude.

From the time plots for the integrated overhead intensities, smooth lines were drawn to best fit the points plotted. In some cases, what are believed to be temporal and/or spatial variations are disregarded and the smooth line drawn as if these small events had not occurred. Whenever this is done, mention will be made of that fact. The smooth curves were analyzed by an opaque projection digitizer (1200 points per inch resolution) which put the hand drawn curves on computer cards. From these curves, the volume emission rate (equal to $\frac{dI}{dZ}$ under constant excitation and spatial conditions) was computed and plotted as a function of time and altitude.

For the photometers (except the up-down photometer), absolute calibration is good to $\pm$20 percent (Appendix A).[22] Problems of determining the slope of the integrated overhead intensity cause varying

errors in the volume emission rate. Error is greatest for the sharp lower edges. Peak values of the volume emission rates should be better than 30 percent. Absolute calibration of the ion mass spectrometer is believed good to a factor of two. The plots given are hand drawn fits of the scattered data points. The He^+ data has by far the worst scatter. The absolute values given for the up-down photometer are only approximate, although relative values should be good to 10 percent. This data will be discussed for the relative picture it gives. Detailed discussion of the up-down photometer data will be left for Dick and Fastie.

3.0 DISCUSSION

3.1 Model Atmospheres

Three model atmospheres have been investigated for use in the analysis to follow. They are considered for the representation of the atmosphere which they give in the 120 to 200 km region. Common parameters for the atmospheric models are the exospheric temperature, and the temperature and number densities at a reference altitude chosen above the turbopause. One hundred twenty km is usually chosen for this reference altitude and diffusive equilibrium assumed above that level. Differences in the various models arise from the different temperature profiles that are chosen.

The exospheric temperature T_{ex} has been calculated using the formulas of Jacchia.[23] Table V gives the appropriate parameters for each rocket flight and the resulting temperature.

Model Atmosphere VII was developed by Zipf[24] to fit the existing optical data. It consists of a numerical integration of the diffusion equation. The densities are calculated every kilometer from 120 km. The integration utilizes a tenth order fit between the one km levels. The temperature dependence of this model was chosen to best fit the existing optical measurements. It exhibits a much smaller temperature gradient at its lower altitudes (5°K/km) than the models which base the temperature dependence on satellite drag and show much higher gradients (20-30°K/km) in the same region.[23,25] Because of the cooler nature of this model, it is less dense than those based on satellite drag.

TABLE V.

Geophysical parameters appropriate to determine exospheric temperature for each yearly experiment.[23]

Rocket Number	1966 UA4.162	1967 UA4.163	1968 UA4.217
$\bar{F}_{10.7}^{ave}$	80.2	129.2	171.8
$F_{10.7}$	82.2	122.2	151.5
Day of year	51	48	40
Universal time for apogee	05:34:02.33	04:21:53.0	04:45:09.0
ψ geographic latitude	58.75°	58.75°	58.75°
$\delta_\odot$ solar declination angle	-11.75°	-12.25°	-15.0°
Geomagnetic index a_p	14	14	15
Exospheric temperature T_{ex}	813	968	1087

Walker[25] presented an analytic expression for the temperature which very closely fit Jacchia's[23] empirical temperature measurements based on satellite drag. Walker's expression was integrable in closed form for the solution of the diffusion equation. The Walker Model exhibits the 20°K/km gradient characteristic of satellite drag measurements, and below 140 km varies less than about 10 percent from Model VII.

The Bates Model[26] uses a simple temperature dependence based on the early satellite drag measurements. It too is a closed form expression of the density of each constituent species; and in the region of interest in this work, it is identical with the Walker Model.

Below 120 km, models become more difficult because of the turbopause. This is a region of minimum temperature and is the transition region from an atmosphere controlled by eddy diffusion and turbulent mixing to one controlled strictly by molecular diffusion.

Table VI gives the model atmosphere assumed for this investigation. Below 120 km the densities are smoothed to the 100 km values given by Anderson and Francis' semitheoretical model.[27] Above 120 km, Model VII is used with an exospheric temperature of 813°K characteristic of the exosphere for the 1966 experiment. Comparison of Model VII for 968°K and 1087°K characteristic of the 1967 and 1968 experiments respectively shows no significant variation below 170 km. The absolute value chosen for the densities at the reference altitude of 120 km provides the biggest unknowns. Table VI also shows the Walker Model.

TABLE VI

Model Atmosphere VII (Walker model is in parenthesis).

Altitude (km)	Number Densities (cm^{-3}) n(O)		n(O_2)		n(N_2)		Temperature °K	
100	5.8^{11}*		1.90^{12}		7.8^{12}			
102	4.6		1.25		5.2			
105	3.3		7.3^{11}		3.0			
110	2.0		2.9		1.30			
113	1.45		1.80		8.1^{11}			
116	1.10		1.10		5.2			
120	8.0^{10}		6.0^{10}		3.0		310	
125	5.6	(5.0)	3.1	(2.9)	1.70	(1.55)	337	(378)
130	3.9	(3.5)	1.70	(1.60)	9.8^{10}	(9.1)	368	(437)
135	2.8	(2.6)	9.9^{9}	(9.7)	6.0	(5.8)	402	(488)
140	2.1	(2.0)	5.8	(6.3)	3.7	(3.9)	440	(532)
145	1.60	(1.55)	3.6	(4.2)	2.4	(2.7)	480	(570)
150	1.20	(1.25)	2.3	(2.9)	1.65	(1.95)	521	(603)
155	9.6^{9}	(1.05)	1.55	(2.1)	1.15	(1.45)	560	(631)
160	7.7	(8.8)	1.05	(1.50)	8.1^{9}	(1.10)	598	(656)
165	6.3	(7.4)	7.5^{8}	(1.15)	5.9	(8.4)	633	(677)
170	5.2	(6.3)	5.4	(8.5)	4.4	(6.5)	665	(695)

*5.8^{11} means 5.8×10^{11}

3.2 The Nitrogen Analysis

All three rockets carried photometers which measured the overhead integrated intensity of the (0-0) band of the first negative system of N_2^+ at 3914Å and the (5-2) band of the first positive system of N_2 at 6685Å. The 1966 experiment also measured the (4-1) band of the first positive system at 6765Å. On both the upleg and downleg of the 1966 rocket flight, almost identical bilayering was observed in the λ3914 and λ5577 OI(^{1}S-^{1}D) signals and not seen in either of the first positive signals or in the λ7774 OI(3^5P-3^5S) signal (Figures 13 and 14). Emission of the λ7774 and the first positive bands is definitely between the two apparent layers which emit the λ5577 green line and λ3914 blue band. It is this fact that makes temporal variations unreasonable answers to what was observed. The similarity of what was seen on the upleg and downleg would also cause concern for temporal variations, as a freak coincidence would be necessary to cause the same effect on the downleg as occurred on the up. The bilayering observed is believed real,[28] but at present no mechanism is understood which could cause such layering in the λ3914 signal and not cause it in the first positive system or λ7774.

In 1968, interference from the moon destroyed any detail which the λ6685 band might have contained. The λ3914 signal and the λ5577 signals were unaffected by the moon, but the aurora was quite weak. Discussion of these signals will be deferred to a later section on the oxygen emissions.

The 1967 optical data is complete, and there are also some

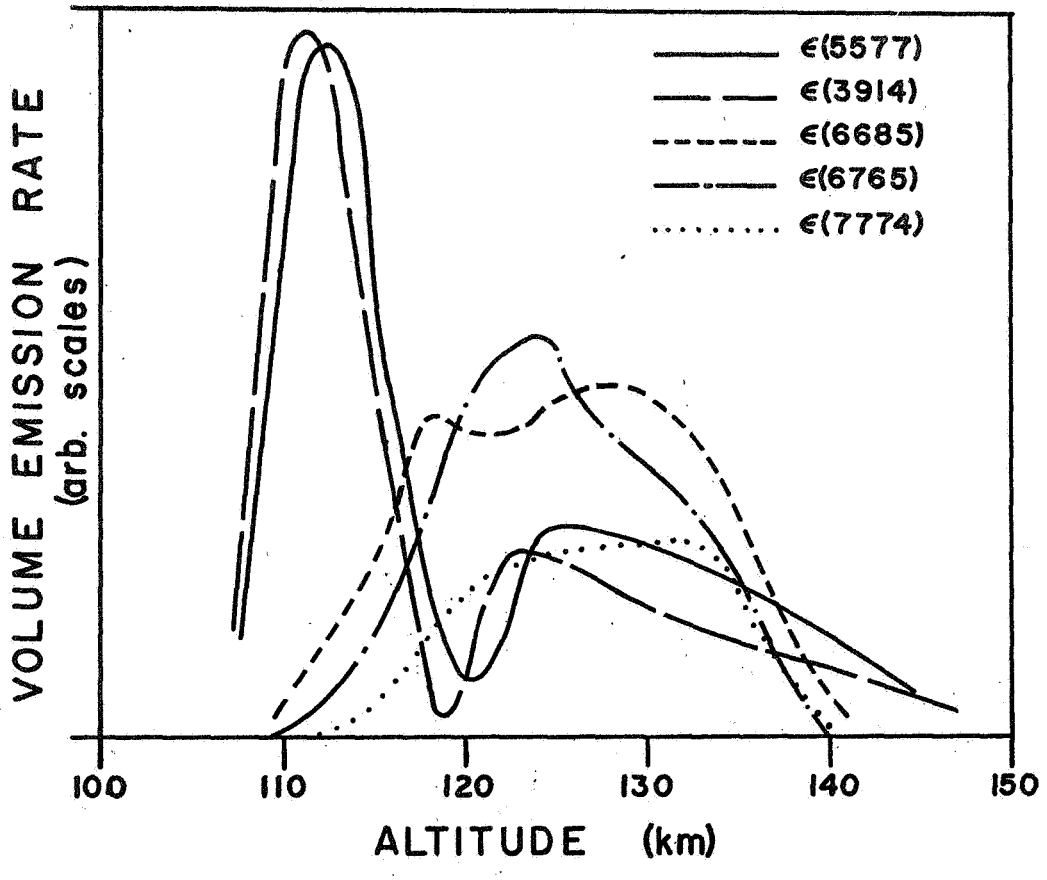

Figure 13. The volume emission rate measured in the 1966 experiment on the upleg. The individual scales are arbitrary.

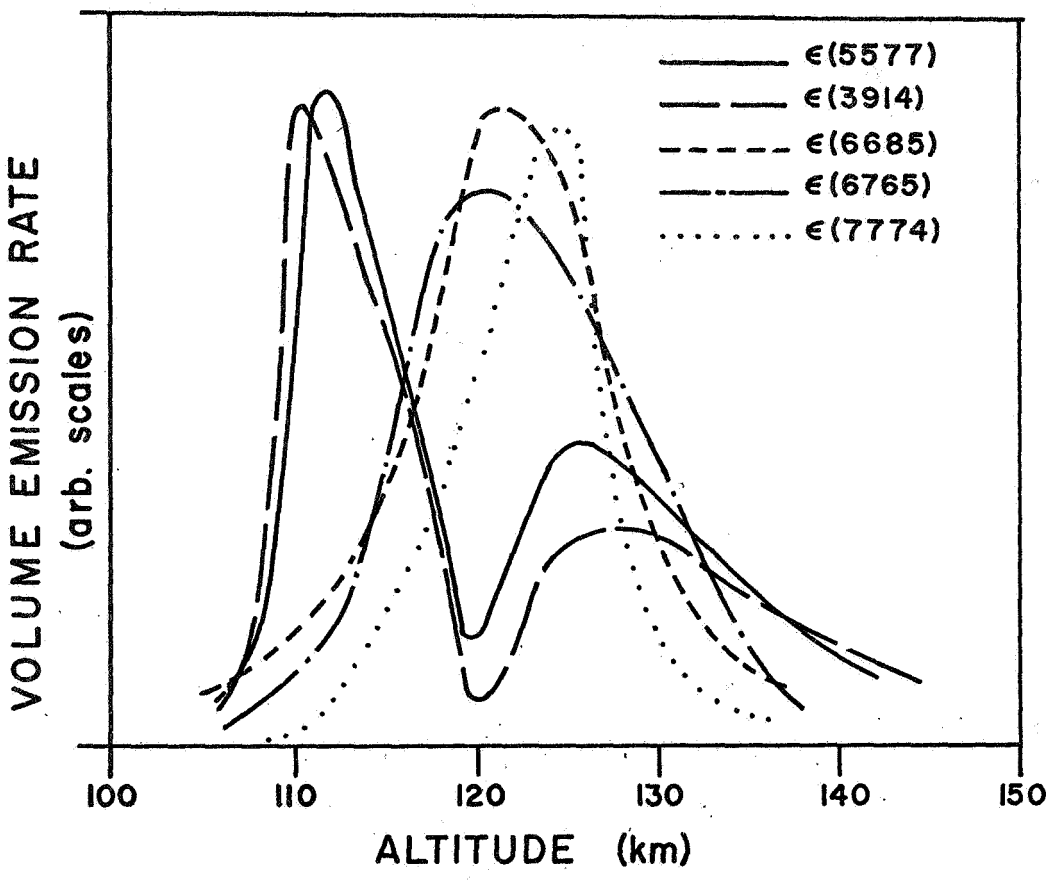

Figure 14. The volume emission rates measured in the 1966 experiment on the downleg. The individual scale are arbitrary.

secondary electron spectra from below 105 km on the upleg and a total electron flux measurement from 105 km on the upleg.[29]

Between 110 km and 120 km on the upleg, a small spatial or temporal variation was seen above the rocket by all photometers. There is no clear indication from the total electron signal that the electrons causing this variation were ever local to the rocket. The up-down photometer also saw this variation above the rocket, but saw no related enhancement below the rocket.[30] Contrast this picture with that observed in 1968 where a temporal variation was seen above the rocket by the photometer, at the rocket by the electron spectrometers and ion mass spectrometer, and finally below the rocket by the down looking portion of the up-down photometer (Section 3.5). The pulse observed in 1967 is considered to be a temporal and/or spatial variation above the rocket only and was not at all seen locally. For this reason, the line drawn to indicate the overhead intensity measured by the photometers ignores this pulse and is drawn as a smooth curve joining the points measured while traversing the stable layer below where the pulse was seen and those measured afterwards, also during a stable period of emission.

During the downleg of this flight, the intensity of the aurora as indicated by the up-down photometer[30] and the total electron flux measured by Doering[29] decreased by a factor of three while the rocket traversed from 130 km to 105 km. In spite of this decrease, this data will be analyzed since the lifetimes of the excited atoms, except possibly the $O(^1S)$, are small.

Doering's electron spectrum[29] for 105 km is shown in Figure 15. Those for 103 and 100 km are the same, and the one for 97 km is decreased in magnitude by a factor of about 2.5. Very clearly, the differential

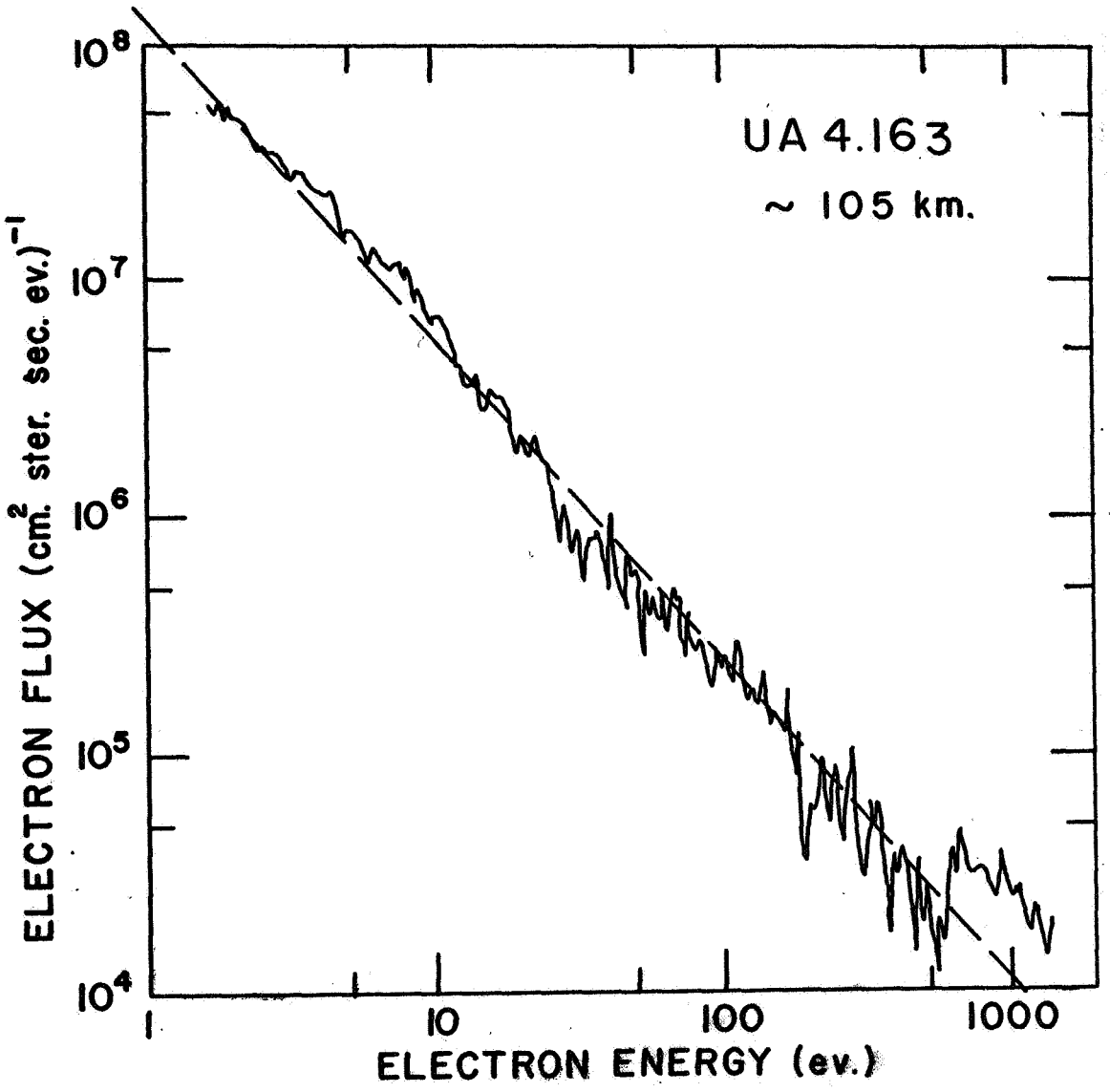

Figure 15. Electron energy spectrum measured by Doering in 1967 on the upleg of the experiment.

flux $\phi(E)$ can be approximated by

$$\phi(E) \propto E^{-A} \quad , \tag{10}$$

where A is the appropriate exponent and has the value 1.36. At 105 km, the volume emission rate of the λ3914 is found by

$$\varepsilon(3914) = 4\pi\, n(N_2) \int_{\text{threshold}}^{\infty} \phi(E)\sigma(3914|E)\, dE \tag{11}$$

where $\varepsilon(3914)$ is the volume emission rate, $n(N_2)$ is the number density of N_2 at 105 km, and $\sigma(3914|E)$ is the excitation cross section for the (0-0) band as recently measured by McConkey, Woolsey, and Burns.[31] This cross section is in good agreement with other recent measurements.[32,33] This integration has been numerically performed on the 7090 computer to 2 kev using the absolute calibration indicated by Doering (Figure 15). The calculated value of $\varepsilon(3914)$ is a factor of six too large, but in discussion with Doering, it was decided that his calibration could be that far off because of geometric and other problems during calibration which affect the absolute sensitivity. The magnitude of the total flux is normalized at 105 km so the calculated volume emission rate is the same as that observed.

The computer also calculated the total flux

$$\Phi_T = 4\pi \int_{\text{threshold}}^{\infty} \phi(E)\, dE. \tag{12}$$

An average excitation cross section, $\bar{\sigma}(3914)$, can be calculated from

$$\bar{\sigma}(3914) = \frac{\varepsilon(3914)}{\Phi_T \; n(N_2)} \tag{13}$$

and has a reasonable value of $1.0 \times 10^{-17} cm^2$ at 105 km using the corrected differential flux for evaluating ϕ_T.

Throughout the flight, the secondary electron spectrum is assumed constant. Doering's experience indicates that this is so. A number of secondary electron spectra are reviewed by Pfister.[34] These have been taken for various auroral intensities and at various altitudes. The spectra presented are remarkably similar.

Assuming a constant energy spectrum, and hence a constant $\bar{\sigma}(3914)$, the total flux has been calculated from the volume emission rate of the λ3914. It is shown in Figures 16 and 17. Also given is the total flux indicated by a Faraday cup collector built into the secondary electron spectrometer.[16] This measured flux has also been normalized to the value determined at 105 km. Considering the noisy measured signal, agreement is very good on the upleg and differs by much less than a factor of two except near the very bottom of the emitting layer. On the downleg agreement is less good, the flux measurement and up-down photometer showing a factor of three change and the calculated flux showing a change of an order of magnitude.

The fluxes calculated above will be used for several further calculations. First, the volume emission rates of the λ6685 first positive band will be calculated. Figure 18 shows the energy levels of molecular nitrogen which are of interest. The excitation of the

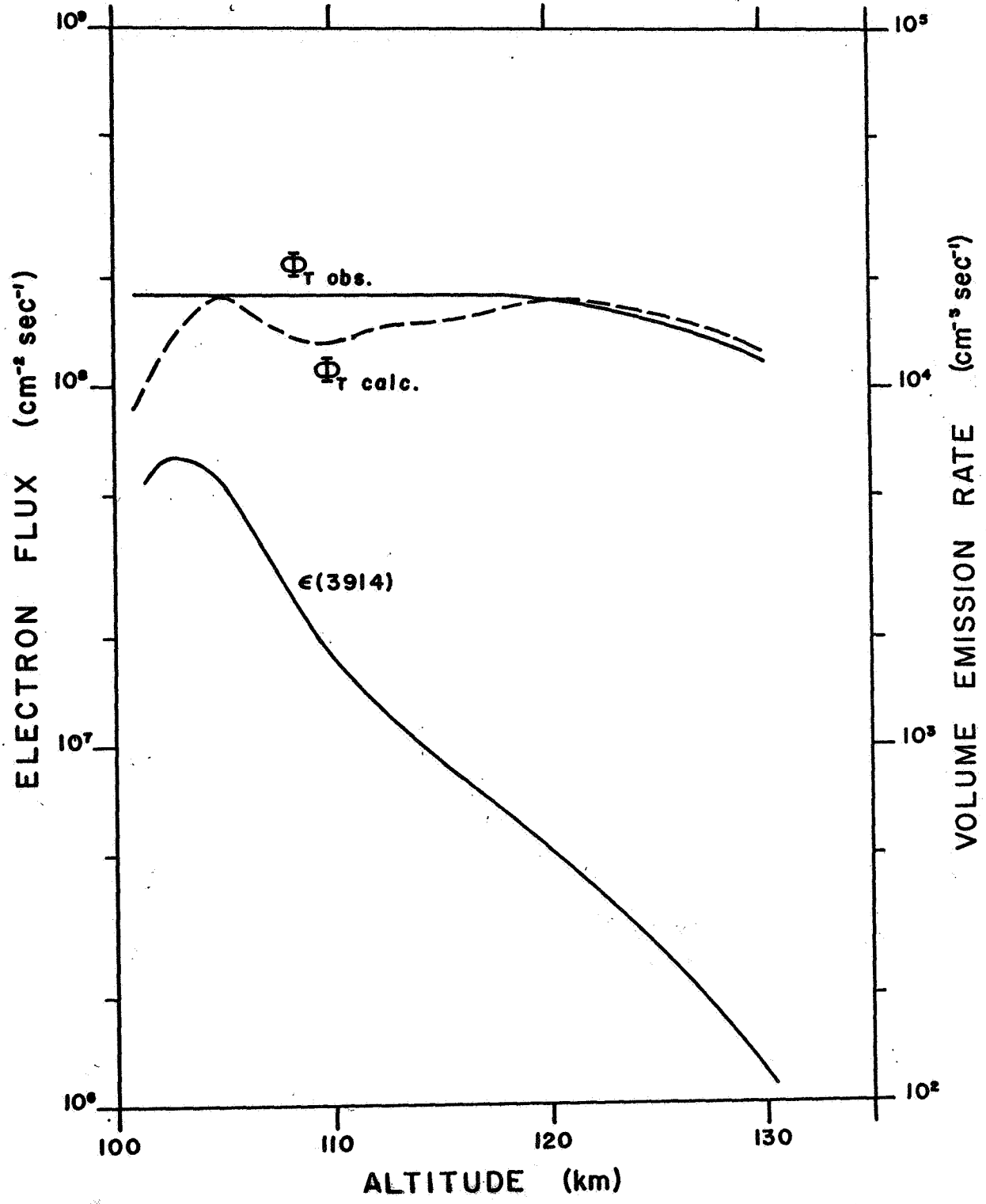

Figure 16. Total electron flux calculated from ε(3914) compared with the normalized measured total flux. This is for the upleg of the 1967 experiment.

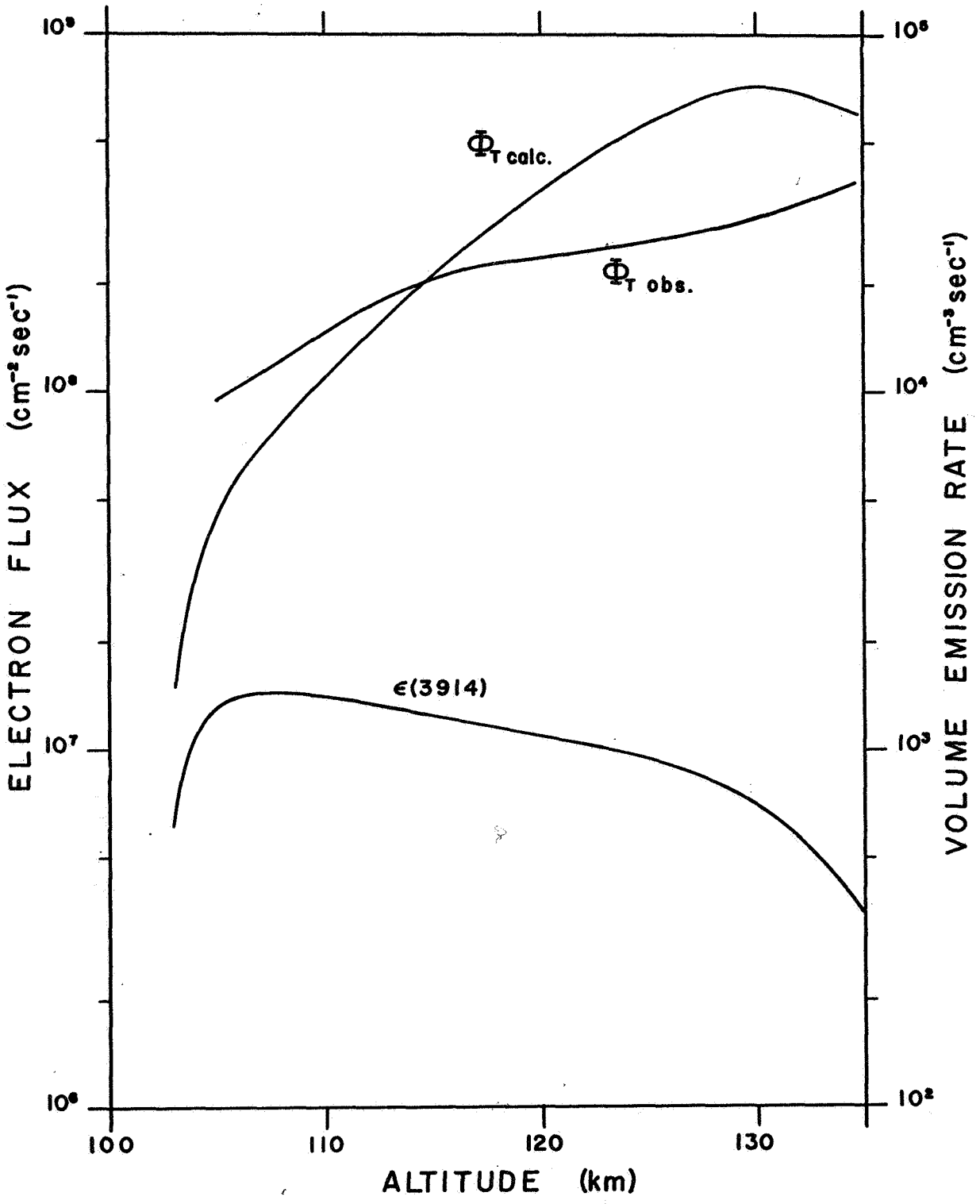

Figure 17. Total electron flux calculated from $\varepsilon(3914)$ compared with the normalized measured total flux. This is for the downleg of the 1967 experiment.

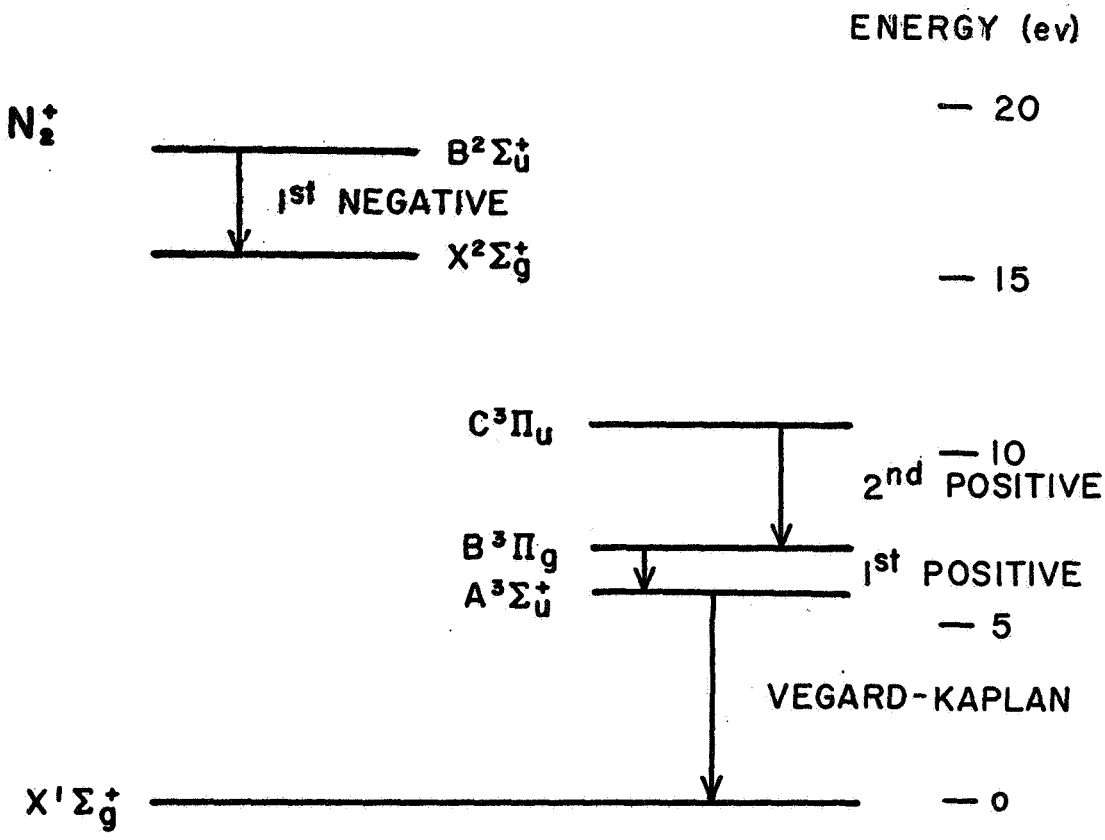

Figure 18. The energy levels of the nitrogen molecule which are of interest.

first positive system by electrons is the sum of the excitation of the $B^3\Pi_g$ state and the $C^3\Pi_u$ state which feeds the $B^3\Pi_g$ state by cascading through the second positive system. Cross sections for excitation of these two states have been estimated by Green and Barth[35] and more recently by Stolarski et al.[36] The cross section they use for excitation of the $C^3\Pi_u$ state is in accord with that measured by Stewart and Gabathuler.[37] Green and Barth's cross sections have been numerically integrated with the corrected flux. The volume emission rate for the λ6685 band, ε(6685), is given by

$$\varepsilon(6685) = 0.03 \times 4\pi\, n(N_2) \left[\int \phi(E)\sigma(B^3\Pi_g|E)dE + \int \phi(E)\sigma(C^3\Pi_u|E)dE\right] \quad (14)$$

where the .03 is the percentage of first positive photons emitted into the (5-2) band at λ6685. This number comes from tables of Franck-Condon factors computed by Benesch et al.[38] The volume emission rate for the λ6685 band can be related directly to the λ3914 band by

$$\varepsilon(6685) = 0.03\ \varepsilon(3914)\ \frac{\left[\int \phi(E)\sigma(B^3\Pi_g|E)dE + \int \phi(E)\sigma(C^3\Pi_u|E)dE\right]}{\int \phi(E)\sigma(3914|E)\ dE} \quad (15)$$

Assuming that the energy spectrum is constant, the λ6685 volume emission rate should follow the λ3914 volume emission rate in the ratio indicated. That this is not the case can be seen in Figures 19 and 20.

The first additional correction that seems reasonable to make is to increase the contribution of the integral $\int \phi\sigma(B^3\Pi_g)dE$ by a factor

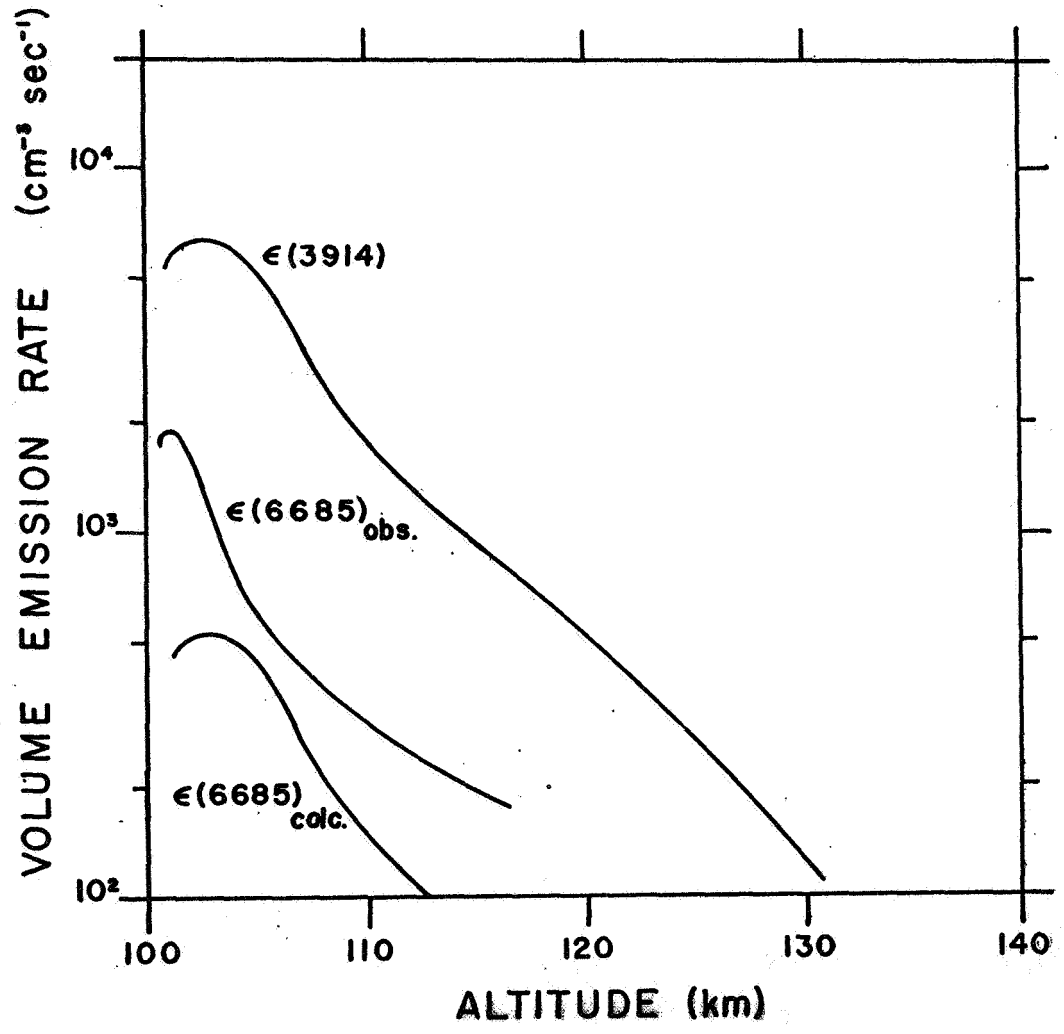

Figure 19. Calculated and observed values of ε(6685) using the cross sections of Green and Barth.[35] This is the upleg of the 1967 experiment.

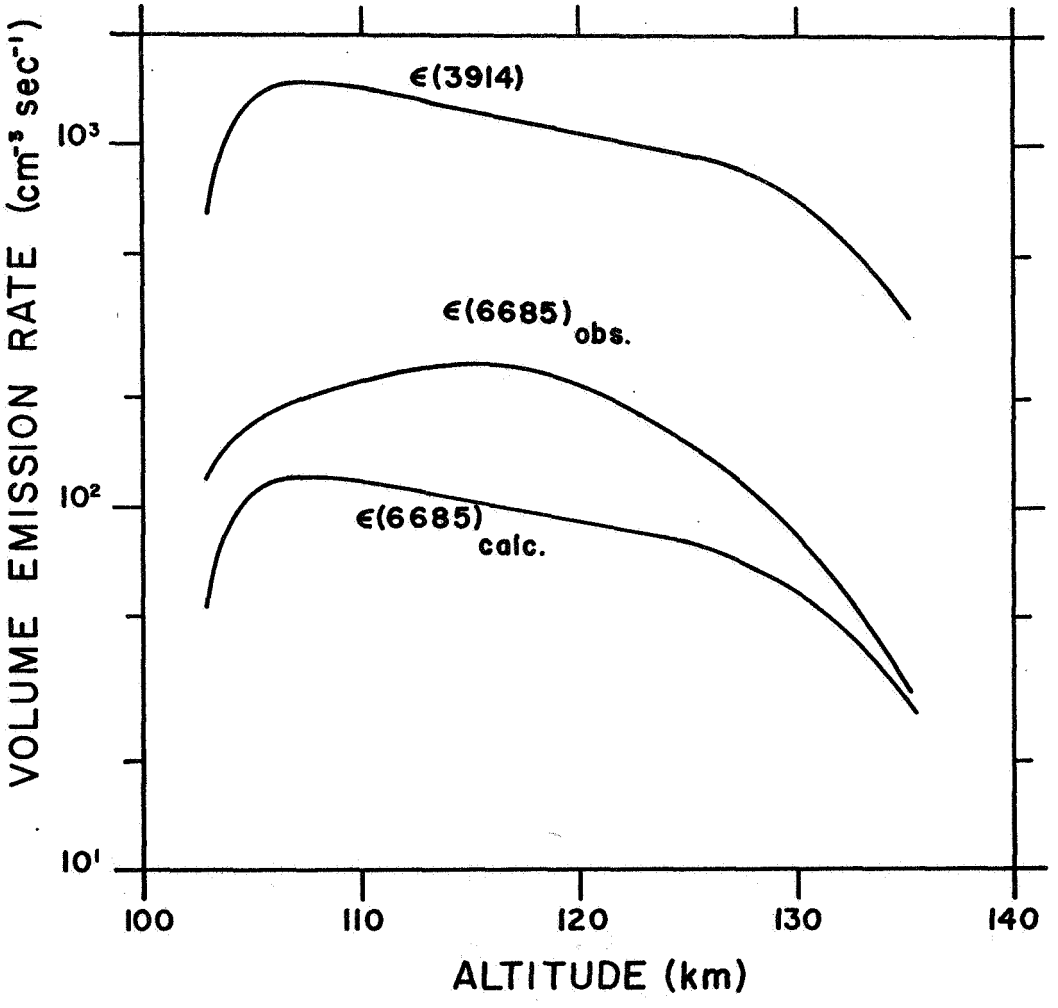

Figure 20. Calculated and observed values of ε(6685) using the cross sections of Green and Barth.[35] This is the downleg of the 1967 experiment.

of 2.9. Then, 16 percent of the first positive system is coming from cascading through the second positive system. This is in line with observations by Broadfoot and Hunten[39] and is higher than those of Benesch et al.[38] and Shemansky and Vallance Jones.[40] It assumed the cross section used by Green and Barth and measured by Stewart and Gabathuler for the $C^3\Pi_u$ state is about right, and the estimated cross section for excitation to the $B^3\Pi_g$ state is too low.

This change is an improvement as can be seen in Figures 21 and 22, but there is still room for more improvement. For the upleg, it is very clear that the volume emission rate for the λ6685 band does not follow that for the λ3914 band. This is the region in which the electron energy spectra show no change. Some other cause for the variation of the cross section for excitation of the first positive system must be found, and a vibrational temperature dependence does not seem out of place.

Dick and Fastie[17] have found about .6 kR of the second positive emission from the (2-0), (3-1), and (4-2) bands at about 93 km. This has been deduced from the least noisy spectrum returned from their half meter spectrometer also flown in 1967. This spectrum was used to determine which portion of the up-down photometer signal was from second positive system, the λ2972 OI(^1S-^3P), and the N_2 Vegard-Kaplan system. They believe the vibrational temperature to be around 2000°K from intensity ratios of various second positive bands.

At 2000°K vibration temperature, about 5 percent of the second positive system emits into the (2-0), (3-1), and (4-2) bands.[41] The measured signal implies about 12 kR of second positive emission. This

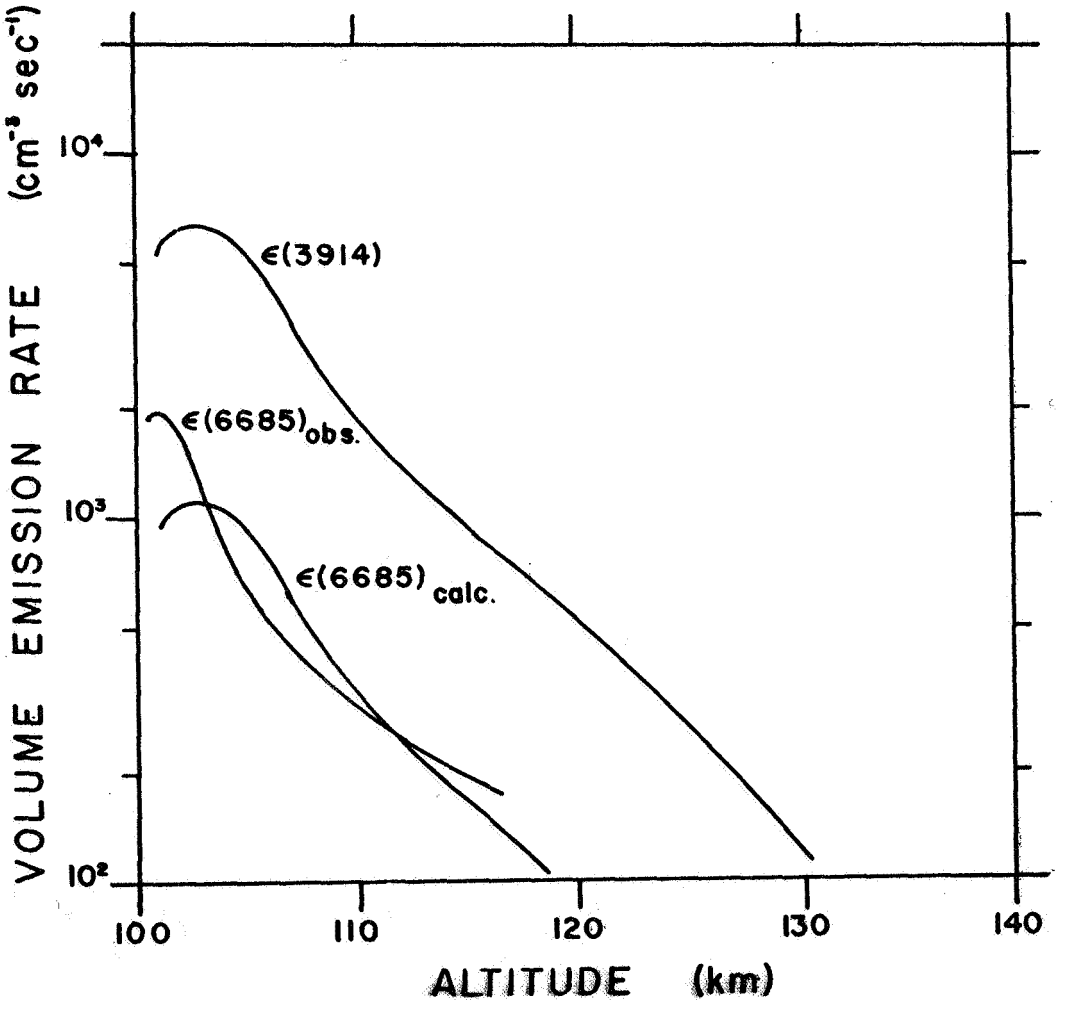

Figure 21. Calculated and observed values of $\epsilon(6685)$ when $\sigma(B^3\Pi)$ is increased to give a 16 percent contribution due to cascading from the $C^3\Pi_u$ state. This is the upleg of the 1967 experiment.

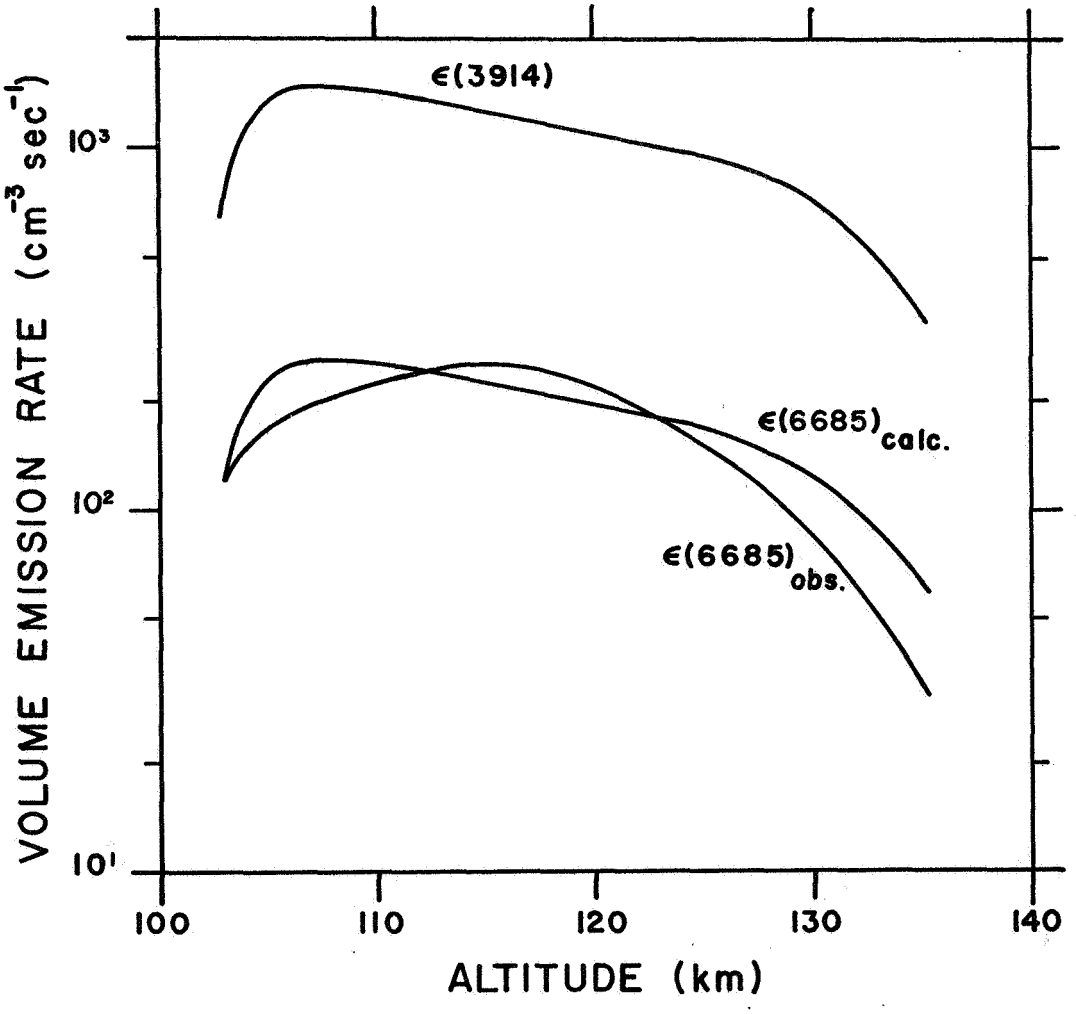

Figure 22. Calculated and observed values of ε(6685) when $\sigma(B^3\Pi_g)$ is increased to give a 16 percent contribution due to cascading from the $C^3\Pi_u$) state. This is the downleg of the 1967 experiment.

in turn implies about 70 kR of first positive emission, using the 16 percent cascading assumed earlier. Of the 70 kR, 3 percent is emitted into the λ6685 band implying about 2 kR for that band. This is about 30 percent more than the value observed. There is plenty of room for speculation for this small disagreement. The most obvious places are the percentage contribution to the first positive system from cascading and the vibrational temperature dependences. Further measurements in the aurora are required.

The preceding discussion of some visible features of molecular nitrogen indicated that the source of excitation is reasonably well understood. The gross features are certainly dependent on the secondary electron flux with finer details perhaps dependent on vibrational temperature of the N_2 molecules and departures from the simple power law expression measured for the secondary electron spectrum.

3.3 The Oxygen Analysis

All three rockets carried photometers which measured the overhead integrated intensity of the OI(^{1}S-^{1}D) green line at 5577Å. In 1966, the OI(^{1}D-^{3}P) red line at 6300Å, the OI(3^5P-3^5S) triplet at 7774Å, and the OI(3^3P-^{3}S) triplet at 8446Å were also measured. In 1967, the (2-0) and (1-0) bands of the first negative system of O_2^+ (at 5279Å and 5618Å respectively) were also measured.

From analysis of the 1966 data, and only the λ5577 green line, λ3914 blue band, and total uncorrected electron flux from the 1967 data

Donahue et al.[28] concluded that only dissociative recombination could excite the $O(^1S)$ in sufficient quantities to cause the observed green line emission. Direct electron excitation,

$$O + e \rightarrow O^* + e \quad , \qquad (16)$$

was rejected because of the insufficient flux capable of exciting the $O(^1S)$ state. Dissociative excitation,

$$O_2 + e \rightarrow O + O^* + e \quad , \qquad (17)$$

was rejected because of an apparent change of cross section with altitude. Particularly interesting is the dissociative recombination process,

$$O_2^+ + e \rightarrow O + O^* \quad , \qquad (18)$$

where the excited atom O^* may be in either the ^1S or ^1D state. Comparsion of the volume emission rates for λ3914 and λ5577 for all flights shows that they possess remarkably similar altitude profiles (Figures 13, 14, 23, 24, and 29). A mechanism which relates the excitation of $O(^1S)$ to the initial ionization process, as indicated by the λ3914 signal, certainly looks promising. A more detailed study of all three processes follows.

Again, data returned from the 1967 rocket will be of most use for this analysis because of its completeness. The secondary electron energy spectrum as shown in the previous discussion (Figure 15) has been integrated with the inelastic electron scattering cross sections of Henry, Burke, and Sinfailam.[42] Those cross sections are a corrected

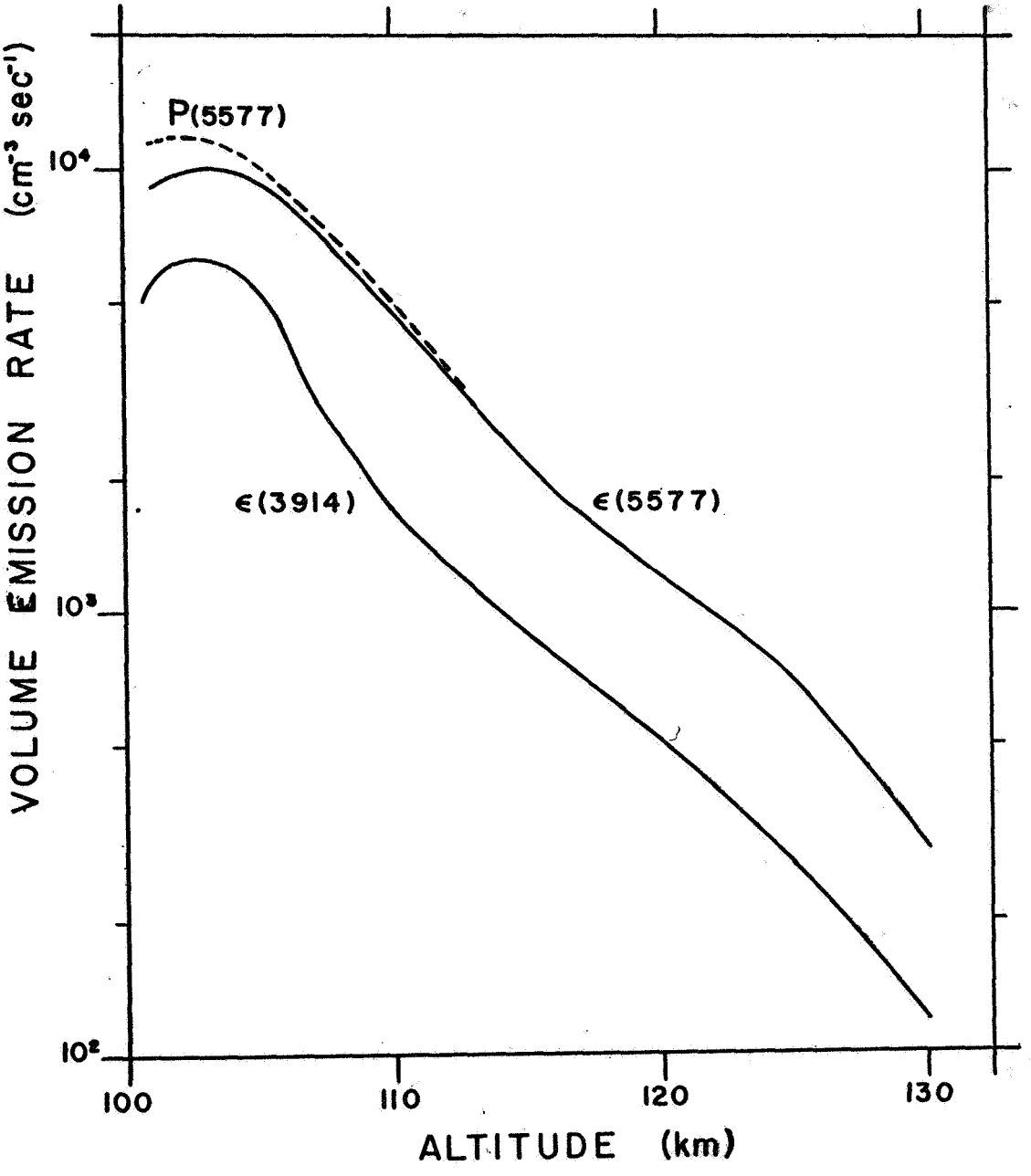

Figure 23. Observed values of ε(3914) and ε(5577) and the appropriate production rate for the ^1S state as measured on the upleg of the 1967 experiment.

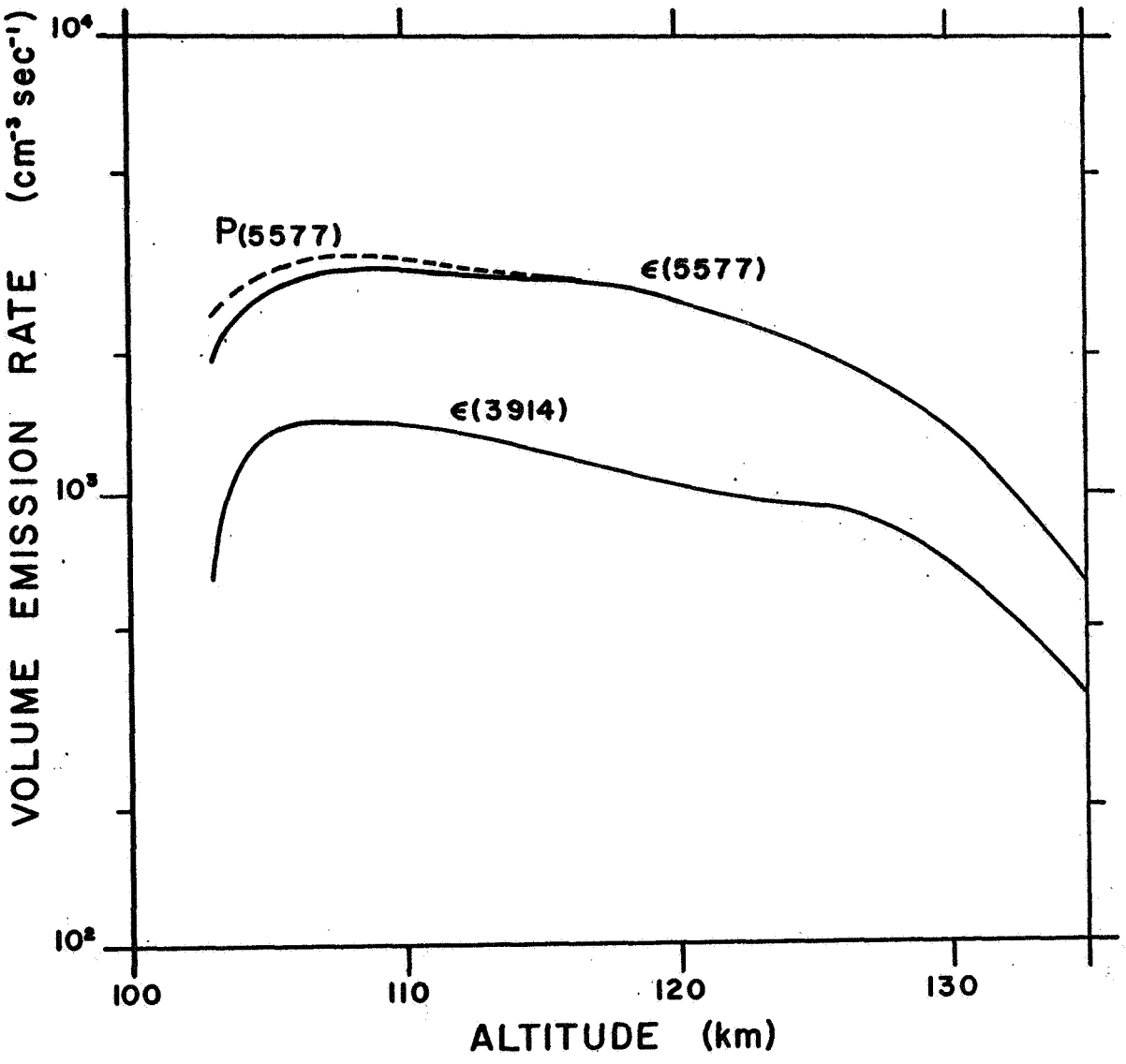

Figure 24. Observed values of ε(3914) and ε(5577) and the appropriate production rate for the ^1S state as measured on the downleg of the 1967 experiment.

version of those earlier given by Smith, Henry, and Burke[43] which in turn were a considerable refinement over Seaton's[9] early efforts.

The volume emission rate for λ5577, ε(5577), is given by

$$\varepsilon(5577) = 4\pi\, Q\, n(0) \int_{4.17ev}^{54ev} \phi(E)\sigma(5577|E)\, dE \quad , \tag{19}$$

where $\sigma(5577|E)$ is the excitation cross section and Q is the quenching factor.

The $O(^1S)$ state is quenched by molecular oxygen. The quenching rate coefficient $d(O_2)$ gives the quenching factor by

$$Q = \frac{1}{1 + d(O_2)n(O_2)/A_{1S}} \quad , \tag{20}$$

where A_{1S} is the total radiative transition probability for the ^1S state. $d(O_2)$ is found by Zipf[44] to be $2.1 \times 10^{-13} cm^3/sec$, and Garstang's[45] values are used for A_{1S}. Figure 25 shows the altitude dependence of Q.

Integration of Equation 19 has been carried out to 54 ev where the given cross sections end. This is a reasonable limit since both the magnitude of the cross section and expecially that of the differential flux have decreased to such an extent that there is a negligibly small contribution from above 54 ev. The flux φ(E) used is related to that calculated for excitation of the λ3914 band (Equation 10). The differential electron flux is given by

$$\phi(E) = B\, E^{-1.36} \tag{21}$$

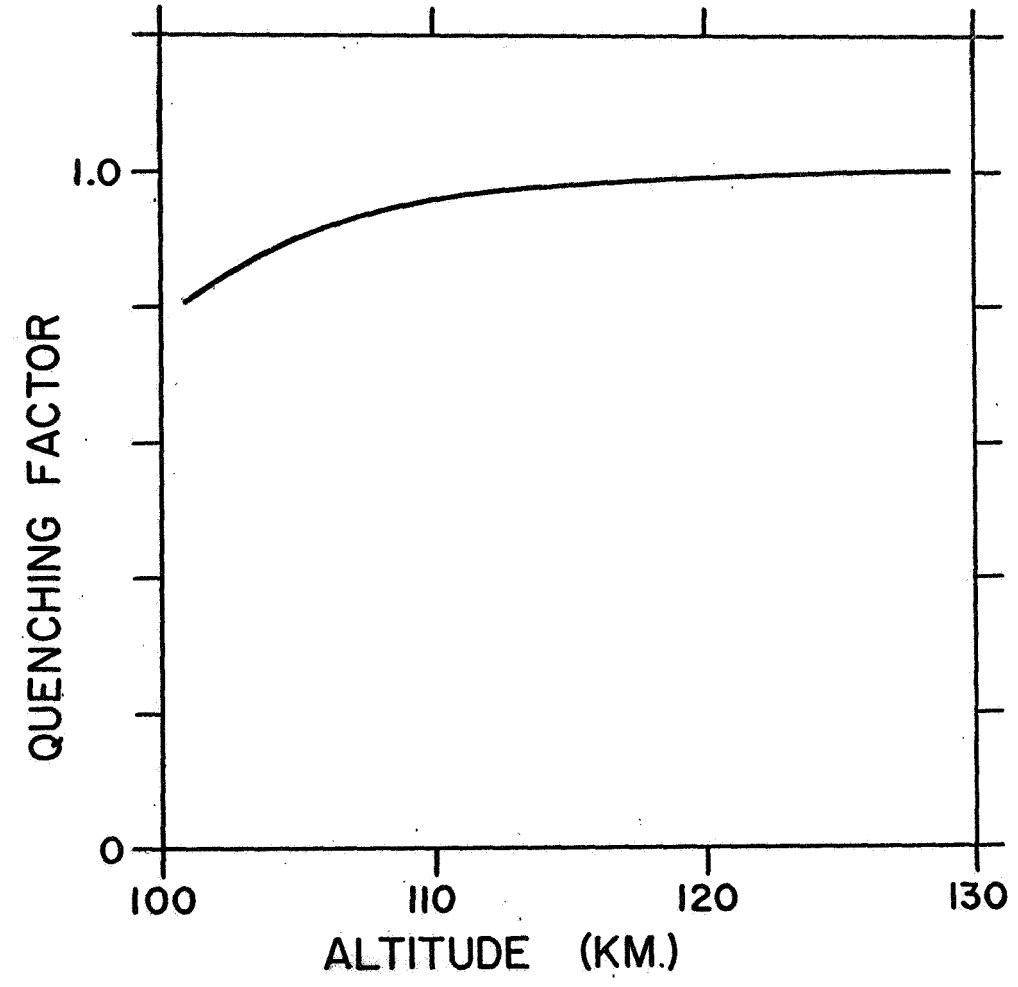

Figure 25. The altitude dependent quenching factor for the $O(^1S)$ state.

In calculating the volume emission rate for λ5577, normalization to the λ3914 band can be made through

$$\varepsilon(5577) = Q\ \varepsilon(3914)\ \frac{n(O)}{n(N_2)} \frac{\int_{4.17ev}^{54ev} E^{-1.36}\sigma(5577|E)\ dE}{\int_{20ev}^{2ev} E^{-1.36}\sigma(3914|E)\ dE} \quad . \qquad (22)$$

The differential flux is assumed constant with altitude as was discussed earlier. Figure 26 plots ε(3914) as observed, and ε(5577) as observed and as calculated by Equation 22. With the model assumed, one to two orders of magnitude deficiency are found. There simply is not a big enough electron flux to directly excite the $O(^1S)$ state as has been assumed for many years.[7,8,46]

The dissociative recombination mechanism is fine in many respects. The ionization cross section is high, and the recombination mechanism channels much energy into the ^1S state. Twenty percent of all recombinations result in an $O(^1S)$ atom.[44] The problem is the large O_2^+ ion densities necessary at the emitting layers. Our own ion mass spectrometer measurements in 1968 and those of others[47,48] show NO^+ to be the dominant ion in the regions of interest. O_2^+ is there above 120 km (Figure 33), but it does not contribute much below that altitude (Figure 29).

The lack of the necessary O_2^+ ions caused reconsideration of the dissociative excitation mechanism (Equation 18). The measured volume emission rate has been used to calculate the dissociative excitation cross section by

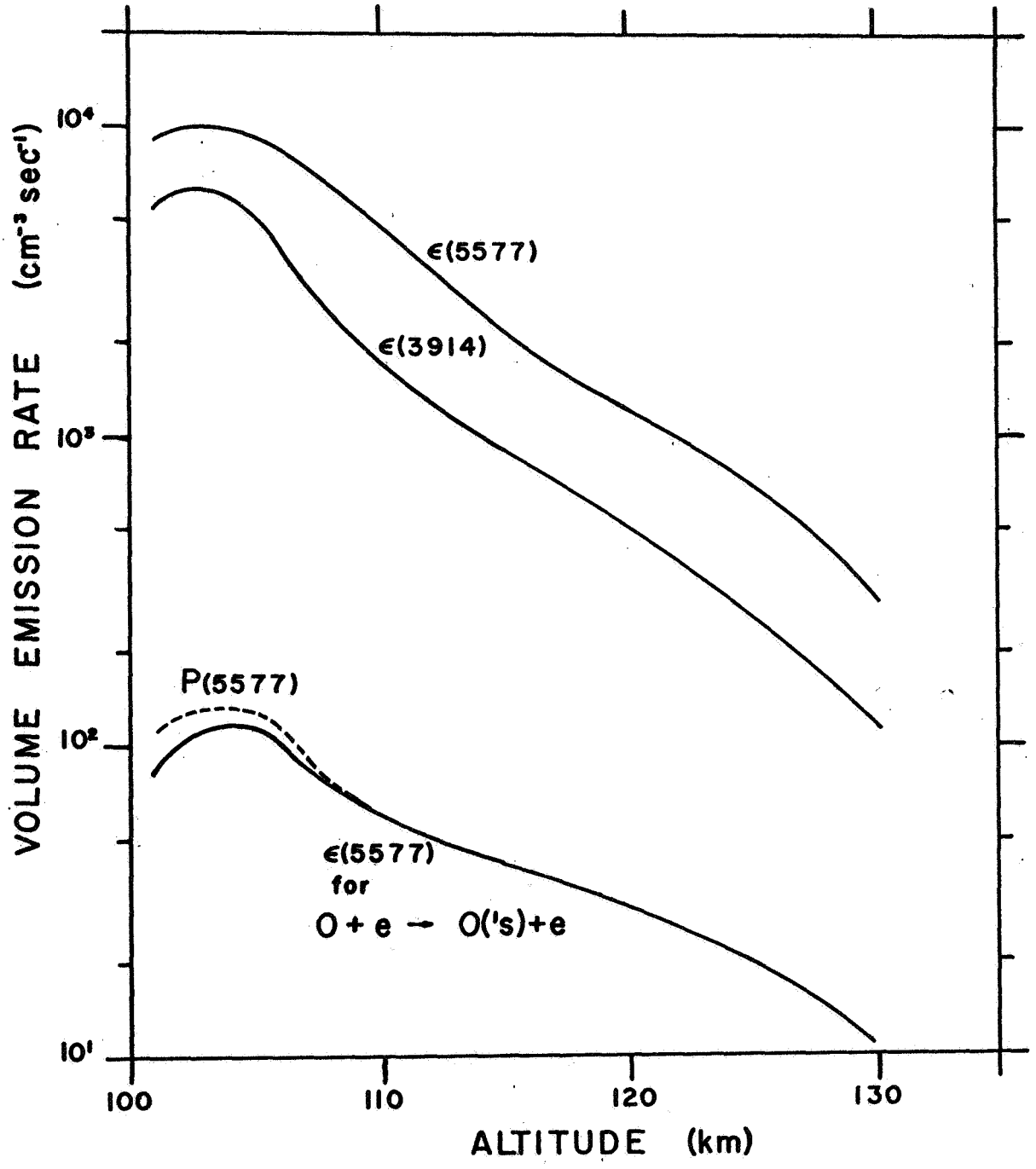

Figure 26. The volume emission rate for direct electron impact excitation of λ5577 compared to the value measured on the upleg of the 1967 experiment.

$$\bar{\sigma}(5577) = \frac{\varepsilon(5577)}{Q\ \Phi_T\ n(O_2)} \qquad (23)$$

The Φ_T used is that calculated from the λ3914 band as discussed earlier (Equation 13) which was in good agreement with the corrected total flux measured for the upleg of the 1967 experiment and showed greater variation than was indicated by the total flux for the downleg. Figures 27 and 28 show the cross sections calculated. Admittedly, there is some apparent altitude dependence; but with the fluxes derived from the λ3914 signal, it is not as bad as indicated by Donahue et al.[28]

This slight variation with altitude can be clearly resolved by looking at the λ5618 and λ5279 O_2^+ first negative signals. Calculations similar to those done to get the dissociative excitation cross section have been done to find the average excitation cross sections for the λ5618 and λ5279 bands,

$$\bar{\sigma}(5618) = \frac{\varepsilon(5618)}{n(O_2)\ \Phi_T} \qquad (24)$$

and

$$\bar{\sigma}(5279) = \frac{\varepsilon(5279)}{n(O_2)\ \Phi_T} \qquad (25)$$

Since λ3914, λ5618, and λ5279 all derive from ionization of the appropriate neutral molecule, and the ionization thresholds for the parent states for both systems are less than 0.5 ev apart,[49] the same total flux which has been calculated from the λ3914 signal can be assumed

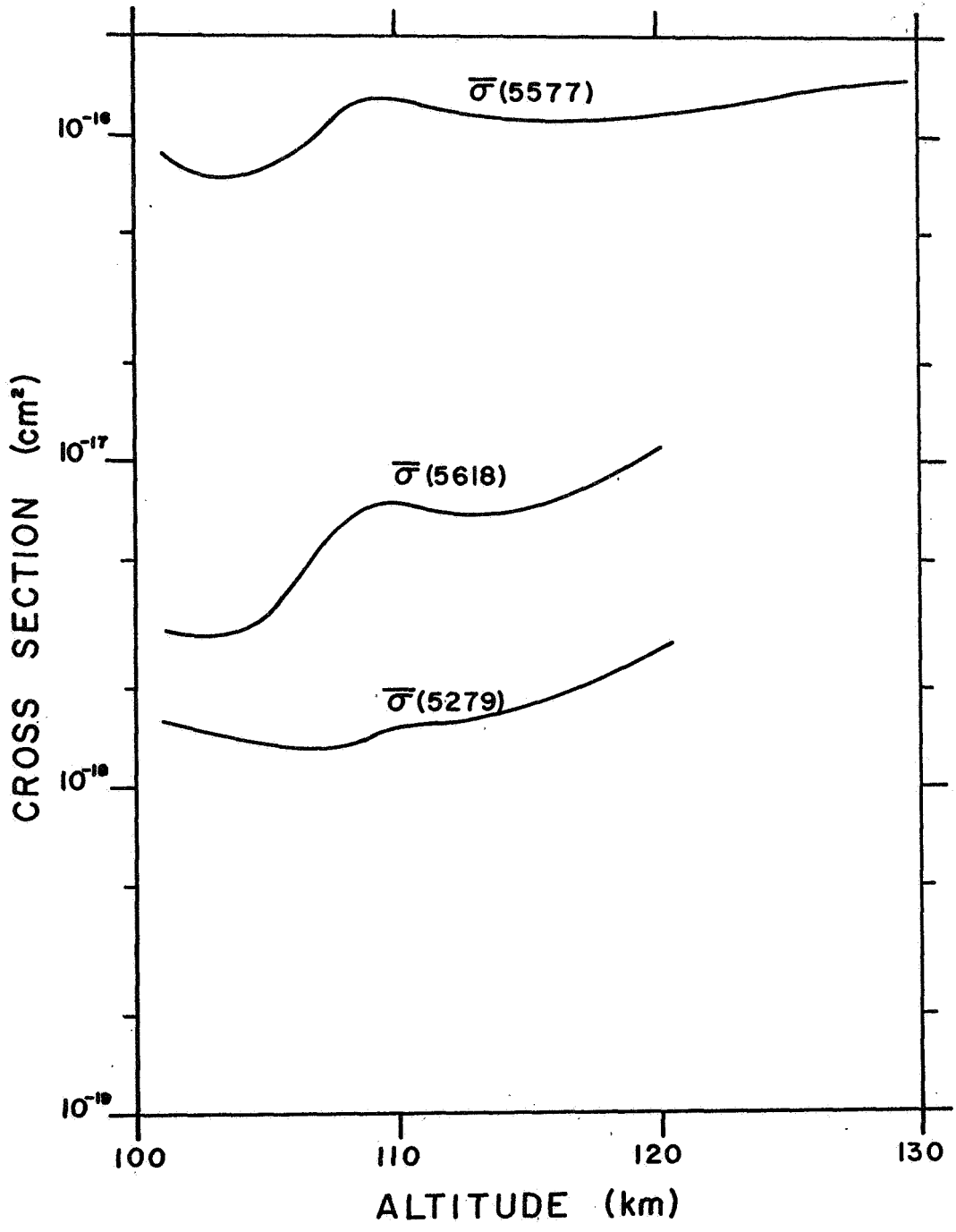

Figure 27. The calculated dissociative excitation cross section for the λ5577 green line. Also shown are cross sections for the (1-0) and (2-0) first negative bands of O_2^+ at 5618Å and 5279Å. This is the upleg of the 1967 experiment.

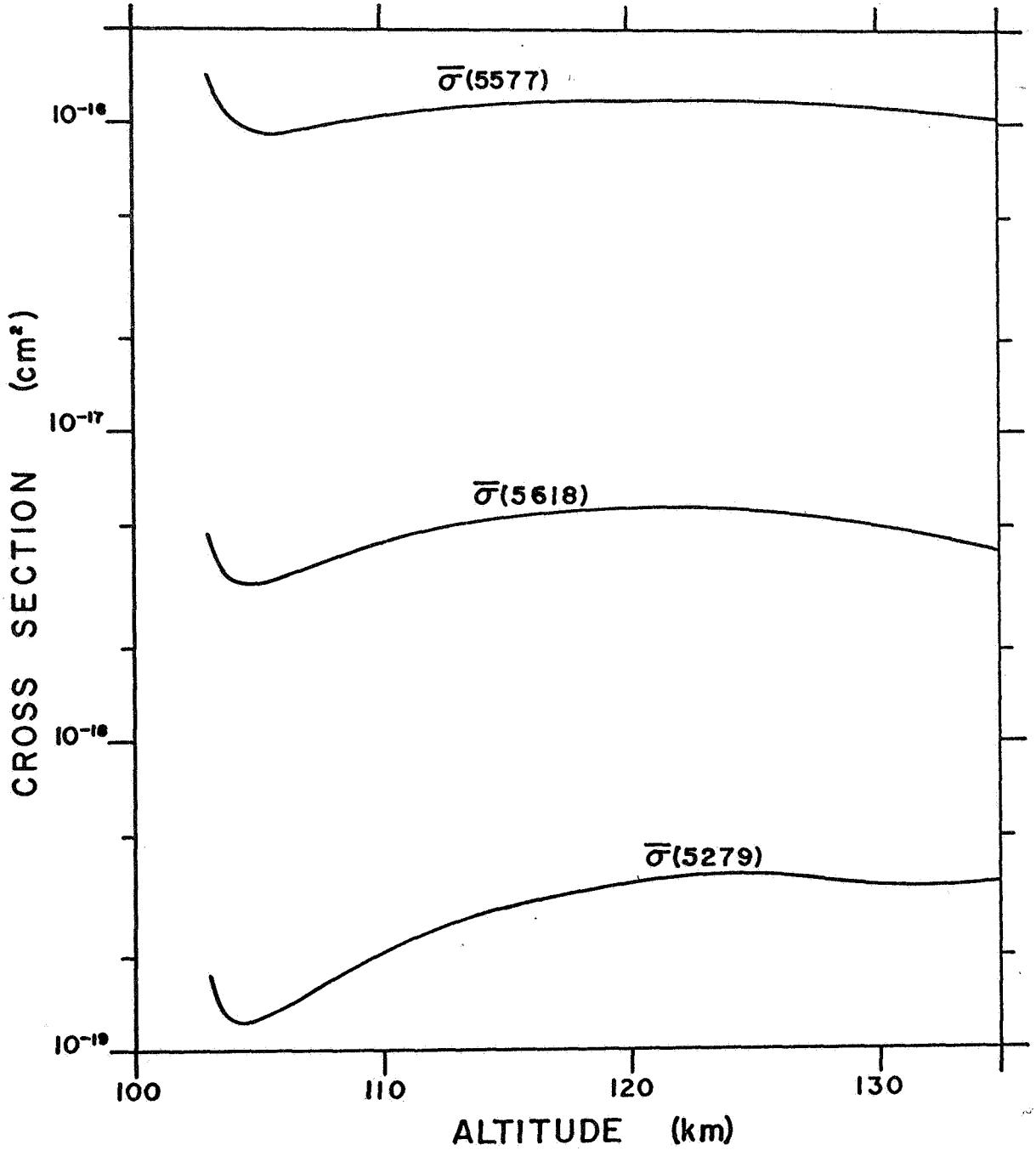

Figure 28. The calculated dissociative excitation cross section for the λ5577 green line. Also shown are cross sections for the (1-0) and (2-0) first negative bands of O_2^+ at 5618Å and 5279Å. This is the downleg of the 1967 experiment.

to also excite the λ5618 and λ5279 band.

Figures 27 and 28 also show $\bar{\sigma}(5618)$ and $\bar{\sigma}(5279)$. Well within the errors associated with its measurement, $\bar{\sigma}(5618)$ shows on both the upleg and downleg of the experiment about the same altitude dependence as does $\bar{\sigma}(5577)$. The absolute magnitude is about $5 \times 10^{-18} cm^2$. There have been no measurements for this cross section, but Stewart and Gabathuler[37] have published a relative cross section for the (2-1) band. Watson et al.[50] have published a phenomenological type calculated cross section for the parent $B^4\Sigma_g$ state. The average of that cross section when integrated with $\phi(E)$ is about six times the above value of $\bar{\sigma}(5618)$, implying that perhaps 16 percent of the first negative emission is in the (1-0) band. This is in very close agreement with the 17 percent shown in a table of relative intensities of the O_2^+ first negative system recently published by Shemansky and Vallance Jones.[40]

$\bar{\sigma}(5279)$ shows roughly the same altitude dependence as $\bar{\sigma}(5577)$, but the change in magnitude of this cross section from the upleg to downleg of the experiment is puzzling. It probably indicates a much stronger vibrational temperature dependence of the transition probability for the (2-0) band than for the transition probability for the (1-0) band at λ5618. On the upleg, $\bar{\sigma}(5279)$ is about 5 percent of Watson et al.'s value for excitation of the whole $B^4\Sigma_g$ state; and on the downleg, it is about 1 percent. The higher value is close to the 4.2 percent given by Shemansky and Vallance Jones.

Figure 29 shows the volume emission rate for λ3914 and λ5577 measured on the upleg of the 1968 experiment. A temporal variation

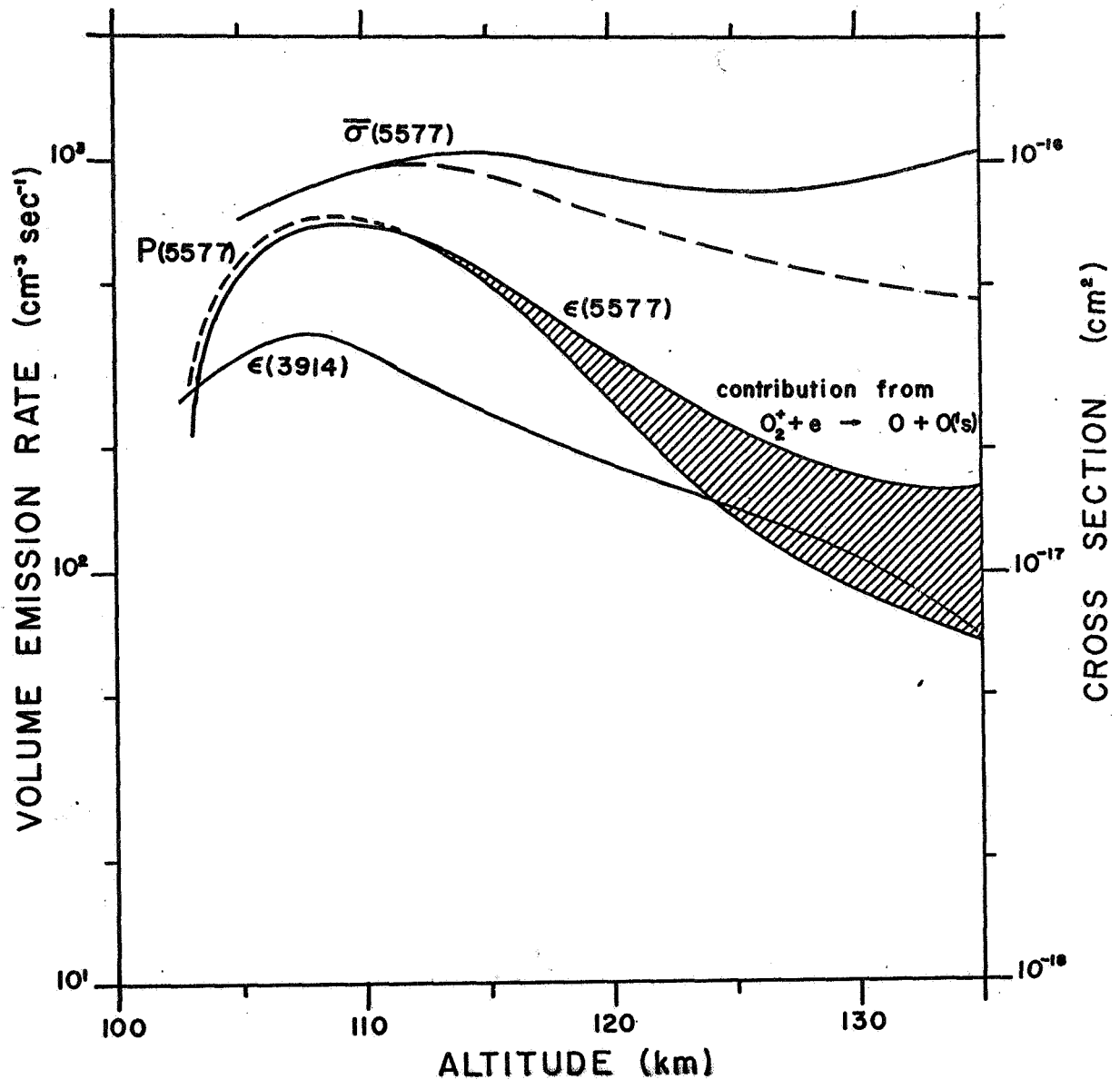

Figure 29. Volume emission rates for λ3914 and λ5577 for the upleg of the 1968 experiment. Also shown is the contribution from dissociative recombination. The dissociative excitation cross section is also shown before and after correction for dissociative recombination.

starting at 127 km (to be discussed later) has been removed from the integrated intensities to obtain the values given. The cross section for dissociative excitation derived from Equation 23 is also shown. There are no unreasonable variations below 130 km. At this point, the ion mass spectrometer data taken at the same time show significant contribution from dissociative recombination.

Assume for the moment that the dissociative excitation cross section is about $10^{-16}cm^2$ as indicated in Figures 27, 28, and 29 (at the emitting altitudes below 130 km). At 140 km, the volume emission rate for λ5577 from dissociative excitation calculated from Equation 23 is about $45/cm^3sec$. The measured value is about $90/cm^3sec$. The remainder must come from dissociative recombination. At this time, the electron density n_e was measured to be $1.7x10^5cm^3$, and the O_2^+ density $n(O_2^+)$ was $3.8x10^4$. This implies, by

$$\varepsilon(5577) = \alpha\, n_e\, n(O_2^+) \qquad (26)$$

that α is $8.4 \times 10^{-9}cm^3/sec$. The measured value at 300°K electron temperature is $4 \times 10^{-8}cm^3/sec$.[44] α is inversely proportional to the electron temperature.[51,52] This relationship implies that at 140 km the electron temperature is 1400°K assuming the branching ratio to the ^1S state is temperature independent. This is a very reasonable value for such a weak aurora.

At 126 km, the contribution from dissociative recombination, assuming 900°K electron temperature, is found to be $80/cm^3sec$, about 38 percent of the total. At 116 km, with a 600°K electron temperature,

there is a 15 percent contribution. The temporal pulse seen between 127 and 135 km hopelessly complicates analysis of the region where transition from the dissociative excitation mechanism to the dissociative recombination mechanism occurs. It is clear, however, that below about 120 km, dissociative excitation is the primary source of the auroral green line; and above about 150 km, dissociative recombination is the source.

Further confirmation of the appropriateness of the dissociative recombination mechanism at the altitudes above 140 km can be seen from the λ6300 red line. The overhead integrated intensity of this feature was measured in the 1966 experiment. Some clearly temporal variations in the brightness of the aurora just before apogee complicate the analysis of the upleg data; and for the present, only the downleg data will be considered. Also, there is a periodic variation of instrumental origin in the red line signal which is common to all signals measured by the filter wheel photometer, and is not seen in the λ5577 green line or N_2^+ ING(0-0) band signals which were measured by independent photometers (Section 2.4).

Figure 30 shows the intensities of the green and red lines for the downleg. Figure 31 shows the red line and green line signals in the 155 to 170 km region. In Figure 31, correction has been applied to the red line intensity for the above mentioned periodic fluctuations.

The data in Figures 30 and 31 clearly show that no measurable emission of the red line occurs below 160 km. Quenching of the $O(^1D)$ state below that altitude is essentially complete. At 165 km, a reason-

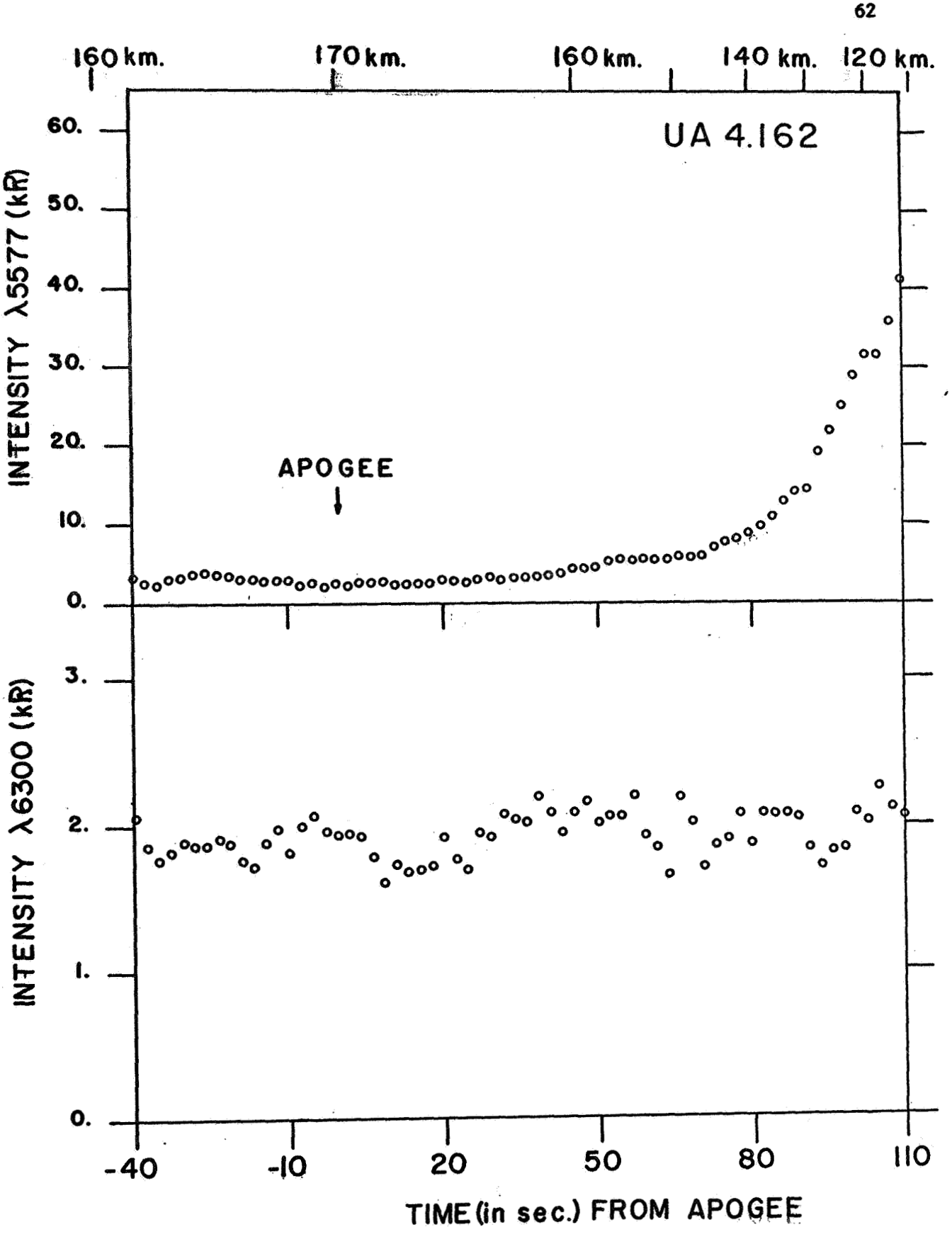

Figure 30. The red and green intensities measured on the downleg of the 1968 experiment.

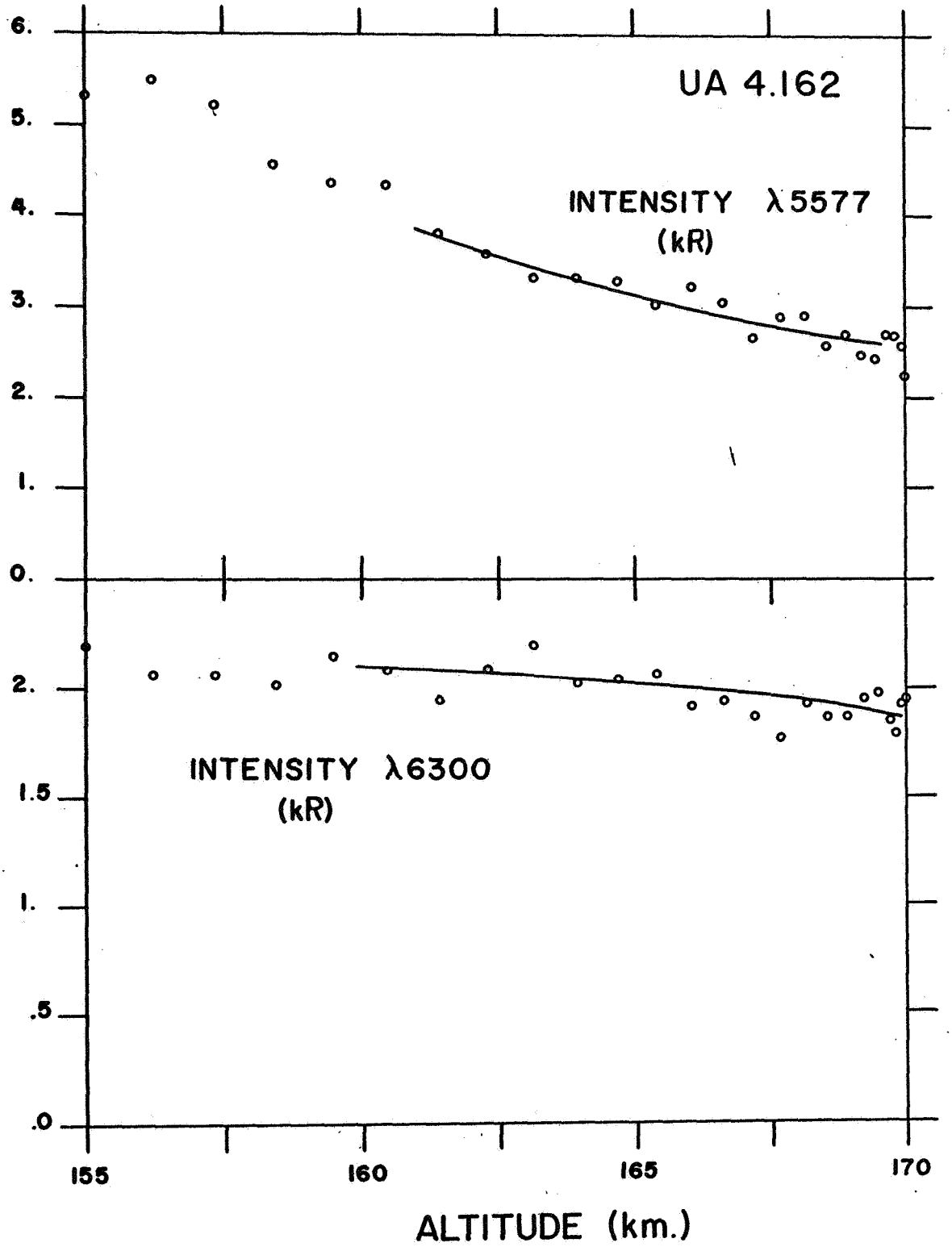

Figure 31. The red and green intensities in the 155 and 170 km region of the downleg of the 1966 experiment.

able value for the volume emission rate of the red line, $\varepsilon(6300)$, is $130/cm^3sec$. The volume emission rate of the green line, $\varepsilon(5577)$, is $1500/cm^3sec$ at that same altitude.

Following the analysis of Hunten and McElroy,[11] the quenching factor Q is defined as the ratio of the observed volume emission rate to that which would be observed in the absence of quenching. For the value which would be observed in the absence of quenching, the volume emission rate of the green line multiplied by a constant r dependent upon the source of excitation is used. Thus,

$$Q = \frac{\varepsilon(6300)}{r \ \varepsilon(5577)} \tag{27}$$

The quenching factor is related to d(X), the quenching rate coefficient for species X, by the following

$$Q = \frac{1}{1 + \sum_X d(X)\ n(X)\ /A_{1D}} \tag{28}$$

where n(X) is the number density of species X and A_{1D} is the total radiative transition probability from the $O(^1D)$ state.[45] Therefore,

$$r = \frac{\varepsilon(6300)}{\varepsilon(5577)} \quad [\ 1 + \sum_X d(X)\ n(X)\ /A_{1D}] \tag{29}$$

Table VII gives the value of r determined using the quenching rate coefficients measured in the laboratory by Noxon[53] and Young[54]. These values of the ratio r are to be compared with laboratory measurements by Zipf[44] and airglow analysis reviewed by Hays and Walker[55] which indicate that for dissociative recombination (Equation 18), between four

TABLE VII

Experimentally determined excitation ratio r.

	Noxon[53]	Young[54]
$d(O_2)$	$6.0 \times 10^{-11} cm^3/sec$	$4 \times 10^{-11} cm^3/sec$
$d(N_2)$	$10 \times 10^{-11} cm^3/sec$	$5 \times 10^{-11} cm^3/sec$
r	6.1	3.1
r_{ave}	4.6	

and five $O(^1D)$ atoms are produced (including cascading) for each $O(^1S)$ atom produced. This is in good agreement with this analysis.

The ratio r can be calculated for the direct electron excitation mechanism,

$$O(^3P) + e \rightarrow O(^1D) + e \qquad (30)$$

and

$$O(^3P) + e \rightarrow O(^1S) + e \quad , \qquad (31)$$

using the calculated excitation cross sections[42] and measured electron fluxes. The secondary electron spectrometer on this experiment did not measure the electron flux at energies as low as the 2 ev excitation threshold of the $O(^1D)$ state.[16] A similar instrument, flown in 1967 and already discussed (Section 3.2), scanned to one electron volt. The spectral shape which that unit measured at 105 km has again been assumed to hold at 165 km (Figure 15).

The ratio r is dependent only upon the energy dependence of the flux and cross section functions, and is given by

$$r = \frac{\int_{1.96ev}^{54\ ev} \phi(E)\ \ \sigma(^1D|E)\ \ dE}{\int_{4.17\ ev}^{54\ ev} \phi(E)\ \ \sigma(^1S|E)\ \ dE} + .95 \quad , \qquad (32)$$

where $\phi(E)$ is that given in Equation 10. The .95 is the contribution due to cascading from the ^1S to ^1D states. Numerical integration was performed on a computer as mentioned earlier. The 54 ev upper limit is sufficient because of the pronounced decrease in both cross section and

flux above 9 ev. The value obtained for r is 18. This is several times the value observed.

It should be noted here that any theory which requires an extremely "soft" flux, necessary because of the low value of the excitation cross section of the $O(^1S)$ state, will produce values of r much greater than 18. The value 38 appeared in a recent paper by Rees et al,[56] Their high value of r, and the resultant high value of the volume emission rate at altitudes below 150 km [$\varepsilon(6300)=1500/cm^3sec$ at 150 km for 70 kR of the green line] is not supported by the rocket borne measurements.

The quenching of $O(^1D)$ provides a check on the rejection of direct electron impact excitation as the primary source of the auroral green line. This is independent of the order of magnitude deficiency of the electron flux shown earlier in this section. The quenching of $O(^1D)$ supports dissociative recombination as the source of the green line at high altitudes in so far as the measured excitation ratio is in agreement with that known for dissociative recombination. The data presented here also confirms Hunten and McElroy's[11] assertion that the analysis of the red-green intensity ratio such as done be Seaton[10] is invalid because the emissions originate from such dramatically different altitudes.

While quenching of the red line is a confirmation of the high altitude dissociative recombination source of the green line, there is other evidence to show that the major portion of the green line intensity, which is emitted in the 100 to 120 km region (Figure 29), comes from a process directly involving the ionizing flux. Observations of

auroral pulsations by Omholt and Harang[57] and Evans and Vallance Jones,[58] which concern phase and amplitude differences between the green line and the first negative system of N_2^+, have about the expected dependence for the direct electron excitation reaction

$$O + e \rightarrow O(^1S) + e \tag{33}$$

To which the green emission had long been attributed. It is noted here that the reaction

$$O_2 + e \rightarrow O + O(^1S) + e \tag{34}$$

would also show about the same phase and amplitude relationship as Reaction 33. Differences observed would be from the minor contribution to the total intensity due to dissociative recombination at high altitudes and the decreasing density of O_2 with respect to N_2 once diffusion establishes itself as controlling the atmospheric densities.

To obtain first hand data, a two channel photometer was constructed so that each channel looked at the same portion of the sky. It continuously recorded the λ5577 green line and λ3914 (0-0) first negative band of N_2^+. The instrument was placed aboard the NASA Convair 990 for the NASA Airborne Auroral Expedition. The expedition spent six weeks in the field and about 80 hours flying in the Arctic observing auroras and polar nightglow.

The λ3914 signal is used to provide information about the incoming electron flux. Using Equation 13, the total electron flux as a function of time t is found by

$$\Phi_T(t) = \frac{\varepsilon(3914|t)}{\bar{\sigma}(3914)\ n(N_2)} \quad , \qquad (35)$$

where $\varepsilon(3914|t)$ is the time dependent volume emission rate of λ3914.

For the dissociative excitation process (reaction 34), the time dependent continuity equation is

$$\tau \frac{d\ \varepsilon(5577|t)}{dt} = \bar{\sigma}(5577)\ \Phi_T(t)\ n(O_2) - \varepsilon(5577|t) \quad , \qquad (36)$$

where $\varepsilon(5577|t)$ is the time dependent volume emission rate for λ5577 and τ is the lifetime of the $O(^1S)$ state. (A similar equation can be written for direct electron excitation, but in view of the insufficient electron flux and improper excitation ratio mentioned earlier, further development is abandoned.) The solution to Equation 36 is

$$\varepsilon(5577|t) = \varepsilon(5577|to)\ e^{-(t-to)/\tau} + \frac{e^{-t/\tau}}{\tau} \int_{to}^{t} \frac{\bar{\sigma}(5577)\ n(O_2)}{\bar{\sigma}(3914)\ n(N_2)} \varepsilon(3914|t')e^{t'/\tau}dt' \qquad (37)$$

where $\Phi_\tau(t)$ has been replaced by Equation 35.

The photometer, however, does not measure the volume emission rate. It measures the integrated intensity I, where

$$I = \frac{1}{4\pi} \int_0^\infty \varepsilon(Z)\ dZ \quad . \qquad (38)$$

The simplifying assumptions made to conveniently perform the Z integration will be discussed.

The lifetime of the $O(^1S)$ state is dependent on altitude because of quenching by O_2. This is significant below 110 km. τ is related to the quenching factor by

$$\tau(Z) = Q(Z) / A_{1S} \quad . \tag{39}$$

(Equation 21 and Figure 25.) While the altitude dependence is not insignificant, quenching is ignored for these calculations remembering that its effect will be to shorten the effective lifetime to some average $\bar{\tau}$. The other assumption made is that during temporal pulsations the energy distribution of the exciting flux remains the same and hence the altitude distributions of the two emissions remain the same. This assumption is idealistic, but the rocket data for more stable aurora indicates that this is at least reasonable for a first step. The effect of these simplifications is to allow the integrated intensity to be considered proportional to the local emission rate. Equation 37 becomes

$$I(5577|t) = I(5577|to)\, e^{-(t-to)/\bar{\tau}} + \frac{e^{-t/\bar{\tau}}}{\bar{\tau}} \int_{to}^{t} \frac{\bar{\sigma}(5577)\, n(O_2)}{\bar{\sigma}(3914)\, n(N_2)}\, I(3914|t')\, e^{t'/\bar{\tau}}\, dt' \quad . \tag{40}$$

By Equation 35 and the time independent version of Equation 36

$$\frac{\bar{\sigma}(5577)\, n(O_2)}{\bar{\sigma}(3914)\, n(N_2)} = \frac{I(5577|t_Q)}{I(3914|t_Q)} \quad , \tag{41}$$

where t_Q is a quiescent period of observation where equilibrium has been established in the column observed. Because of variations of the ratio of intensities of green to blue, it is convenient to let t_Q be the same as t_o, the initial time chosen; and hence, t_o is chosen as the last reasonable quiescent period before the pulsations investigated begin.

A computer program has been written which solves the following equation,

$$I(5577|t) = I(5577|t_o) \left[e^{-(t-t_o)/\bar{\tau}} + \frac{e^{-t/\bar{\tau}}}{\tau I(3914|t_o)} \int_{t_o}^{t} I(3914|t')\, e^{t'/\bar{\tau}}\, dt'\right] \qquad (42)$$

when given $I(3914|t')$ at sufficiently small time intervals that $I(3914|t')$ can be considered linear in time over that interval.

During the Auroral Expedition, several periods of pulsations were observed. For none of these was the λ5577 intensity greater than 3 kR. So far analysis has been done on one period at 09:24 UT on 3 March 1968. Other photometers and the all sky camera aboard confirmed that pulsations were being seen and not fine auroral structure.[59,60] A reasonable value for t_o was found, and about 50 seconds of pulsations were calculated on the basis of the λ3914 integrated intensity. Figure 32 shows the λ3914 source signal, the λ5577 calculated signal, and the λ5577 observed signal. There is no strong departure of the observed signal from the calculated signal. The most noteworthy difference is the consistent 3 to 10 percent decrease of the observed λ5577 intensity at pulsation peaks compared to the calculated intensity. This could

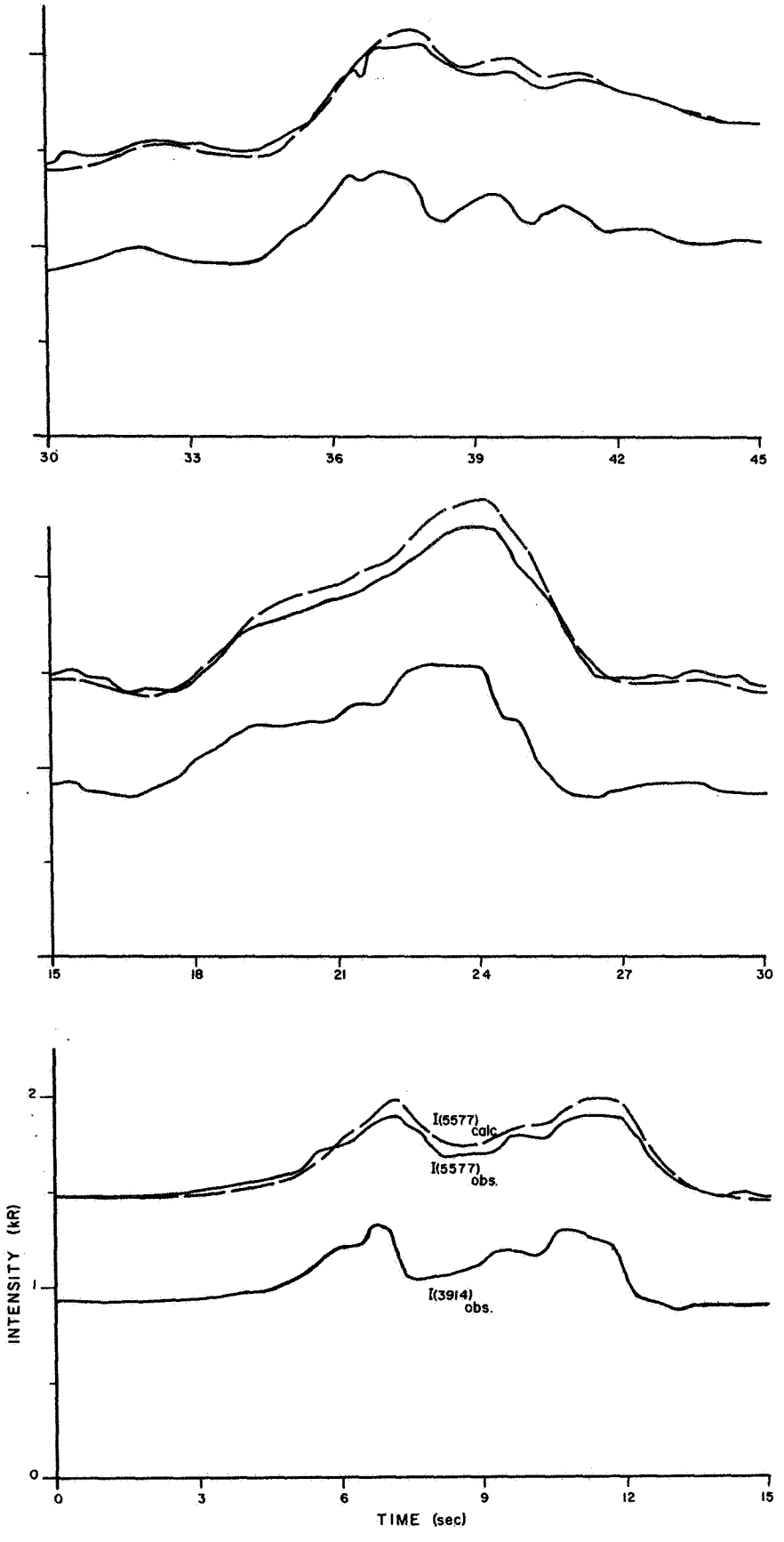

Figure 32. A series of pulses observed at 09:24 UT on 3 March 1968. At the peaks, the calculated intensity (dashed line) is greater by 3 to 10 percent than the observed intensity

be caused by slower nonlinear effects due to the minor contribution to the total λ5577 signal from the high altitude dissociative recombination mechanism. It could also be caused by electron energy changes and the accompanying changes in altitude distribution which are unknown.

This experiment did not find the dramatic phase and amplitude changes expected for the dissociative recombination mechanism.[28,61] Furthermore, since NO^+ is the dominant ion, the analysis which indicated these dramatic effects is invalid. A more complex replacement analysis consistent with the ion mass spectrometer results has yet to be developed. An analysis considering only the dissociative recombination mechanism will be appropriate only for very high pulsating auroras. Further studies of pulsation with respect to the green line are not expected to yield vastly different results.

Romick and Belon[62] have found the I(5577) /I(3914) ratio is higher toward the center of stable arcs. This has been confirmed by Brekke and Omholt.[63] The high altitude dissociative recombination mechanism is nonlinear and can explain the observed phenomena. Further discussion is dependent upon better theoretical knowledge of the ion composition and details of the analysis of the ground based data. Some of the assumptions necessary for reduction of ground based data obviously need re-evaluation in view of the rocket borne data.

All observations are consistant with the dual dissociative source proposed in this section. Variations of the contribution of each mechanism are to be expected, and further sophisticated rocket investigation of brighter auroras is very important. It is also expected that when the

dissociative excitation cross section is measured in the laboratory, it will be found between 6 and 10 x $10^{-17}cm^2$.

3.4 Ion Composition

Figure 33 shows the smoothed ion densities (except 4^+) measured on the upleg of the 1968 experiment. The values given are corrected as discussed earlier (Section 2.3). Figure 34 shows data for the upleg and downleg for 4^+. The downleg of the flight shows considerably more 4^+ than the upleg as would be expected when the ion mass spectrometer fell back through a vehicle generated cloud. Helium was used to pressurize the rocket sustainer and is believed to be the source of much of the 4^+ ions detected, expecially the excess observed on the downleg.

There are several striking features in the ion data. The data shown in Figure 33 is very similar to that of Johnson et al.[47] and Swider et al.[48]. It shows far more NO^+ than expected.[28] The photometers carried with this experiment guarantee that the rocket was in an aurora when the data was taken.

In the 115 km to 126 km region, where constant excitation conditions prevailed, the ratio of 30^+ to 32^+ varies from about 20 to 8. The latter number is in reasonable agreement with that of Swider et al. To explain this high ratio, higher density of neutral NO has been suggested. Another means of increasing this ratio would be the following,

$$O_2^+ + N_2^* \rightarrow NO^+ + NO \quad , \qquad (43)$$

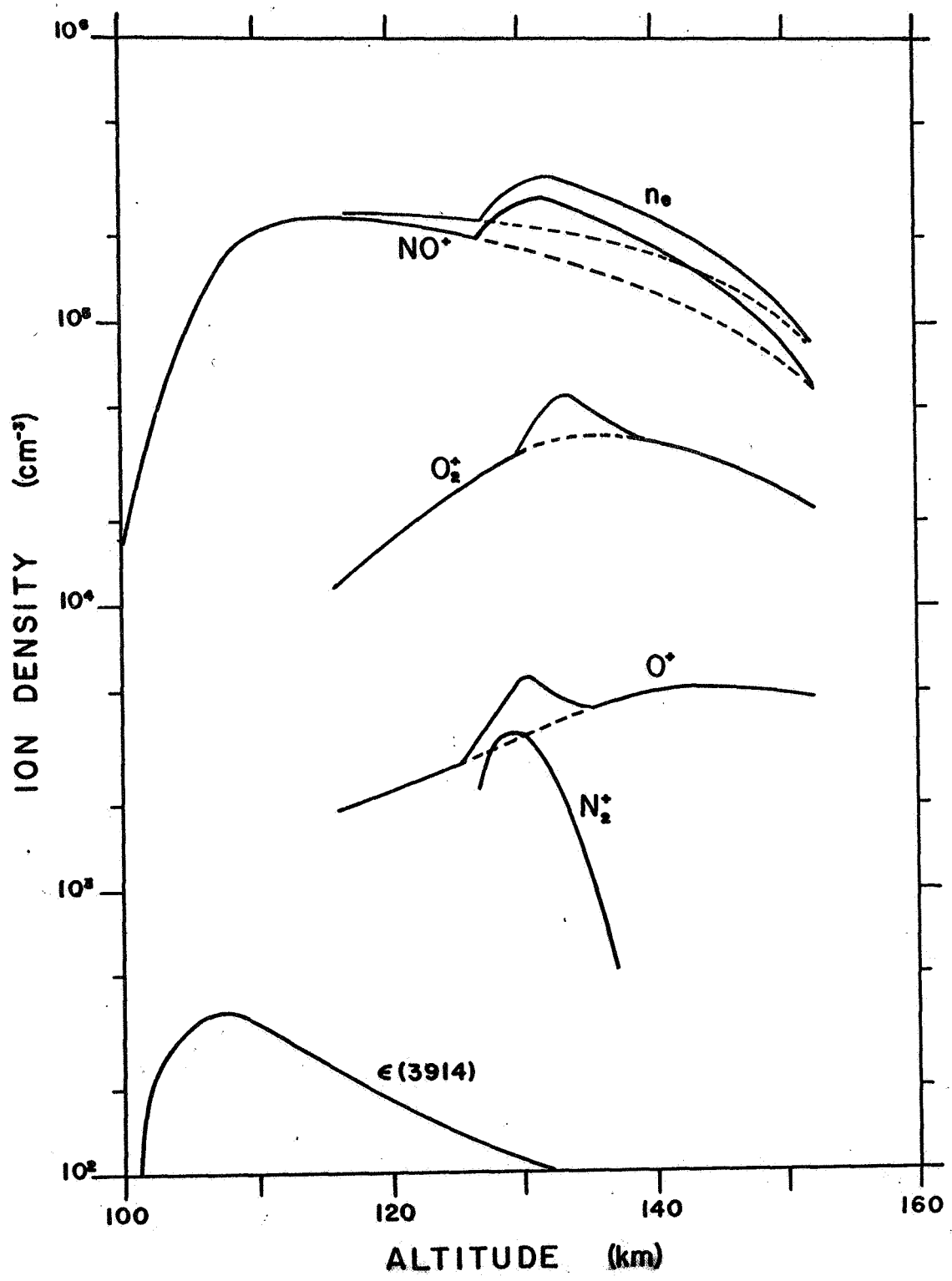

Figure 33. The ion densities measured by the ion mass spectrometer. Dashed lines indicate values expected had there been no fluctuation at 127 km.

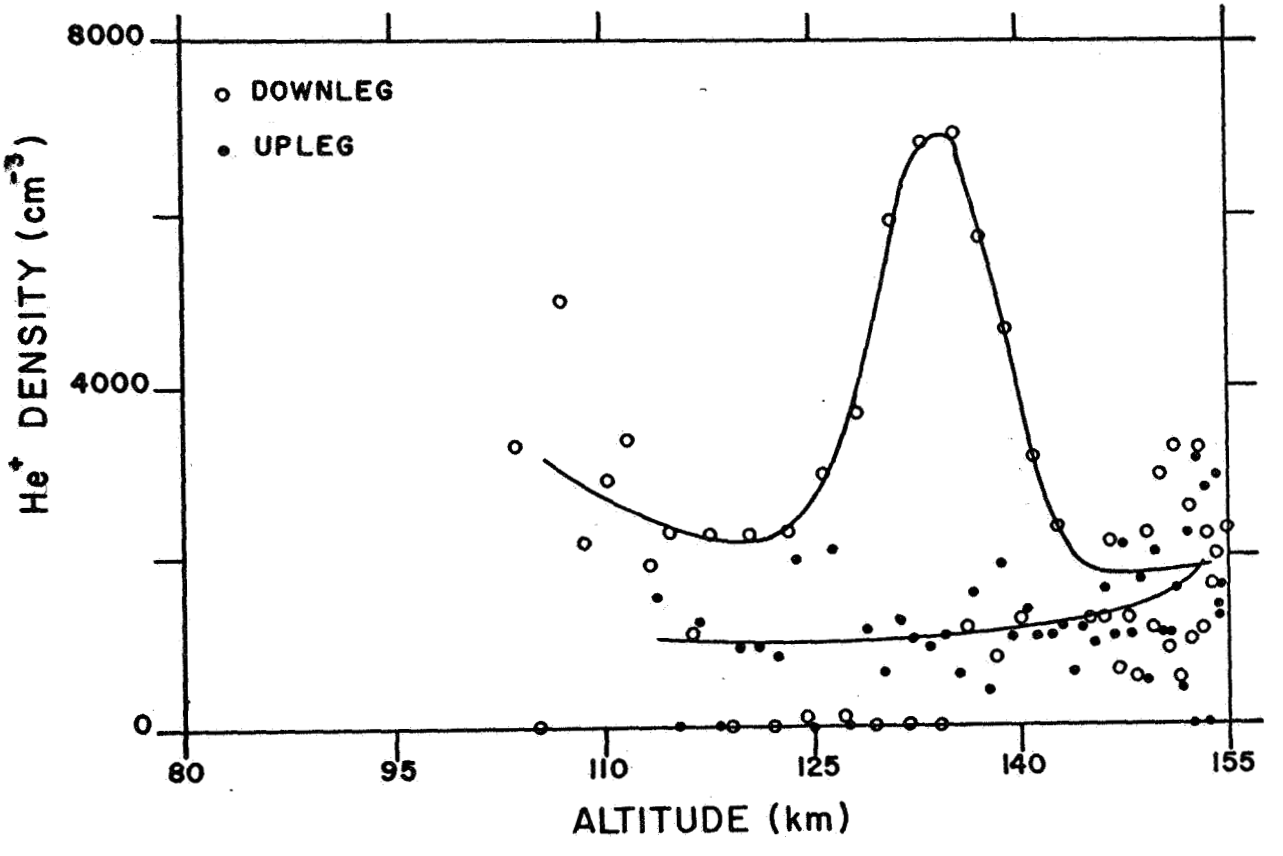

Figure 34. He^+ densities observed in the 1968 experiment.

where N_2^* is a vibrationally excited nitrogen molecule. Both mechanisms increase the NO^+ density at the expense of the O_2^+ density. Possible dependence of the rate coefficient for Reaction 43 on the vibrational temperature of the neutral N_2, as is known for the reaction

$$O^+ + N_2^* \rightarrow NO^+ + N \quad , \qquad (44)$$

could produce the two orders of magnitude increase which would cause the NO^+ to O_2^+ ratio observed.

The above proposal does not appear consistant with the high O^+ density observed in the 1968 experiment. The continuity equation for the density of O^+, $n(O^+)$, for steady state conditions is

$$P(O^+) = n(O^+)[k_{12}(T_v)n(N_2) + k_{13}\, n(O_2)] \quad , \qquad (45)$$

where $P(O^+)$ is the production rate of O^+, $k_{12}(T_v)$ is the vibrational temperature dependent reaction rate coefficient for Reaction 44, and k_{13} is the reaction rate coefficient for the charge exchange reaction

$$O^+ + O_2 \rightarrow O_2^+ + O \quad . \qquad (46)$$

The production of O^+ is related to the ionizing flux as determined from the volume emission rate for $\lambda 3914$ by

$$P(O^+) = \frac{n(O)}{n(N_2)}\ 14\ \varepsilon(3914) \qquad (47)$$

as was done by Donahue et al.[28] Using a vibrational temperature equal to the gas temperature of about 310°K, Equation 45 at 125 km gives only

about 30 percent of the density observed. This difference is somewhat greater than the tolerances on the absolute calibrations involved. An increase in vibrational temperature only makes the situation worse.

Figure 35 shows the important source and loss terms for each constituent ion. Assuming steady state excitation conditions, the continuity equations of the model shown in Figure 35 are

$$n(O)/n(N_2)\ 14\ \varepsilon(3914) = n(O^+)[n(N_2)\ k_{12} + n(O_2)\ k_{13}] \tag{48}$$

$$14\ \varepsilon(3914) = n(N_2^+)[n(O)\ k_{21} + n(O_2)\{k_{23} + \acute{k}_{23}\} + \alpha_2\ n_e] \tag{49}$$

$$\begin{aligned} n(O_2)/n(N_2)\ 14\ \varepsilon(3914) = {} & -n(O^+)n(O_2)\ k_{13} - n(N_2^+)n(O_2)\ k_{23} \\ & + n(O_2^+)[n(N_2)\ k_{32} + n(NO)\ k_{34} + \alpha_3\ n_e] \end{aligned} \tag{50}$$

$$\begin{aligned} 0 = {} & -n(O^+)n(N_2)\ k_{12} - n(N_2^+)[n(O)\ k_{21} + n(O_2)\ \acute{k}_{23}] \\ & - n(O_2^+)[n(N_2)\ k_{32} + n(NO)\ k_{34}] + \alpha_4\ n(NO^+)n_e \end{aligned} \tag{51}$$

$$n_e = n(O^+) + n(N_2^+) + n(O_2^+) + n(NO^+) \quad . \tag{52}$$

A versatile computer program has been written which easily solves this set of nonlinear equations by a series of approximations for the total electron density. Lists of values for n_e are successively searched until the value chosen agrees to any desired precision with the sum of the ion densities. Figure 36 shows the ion composition

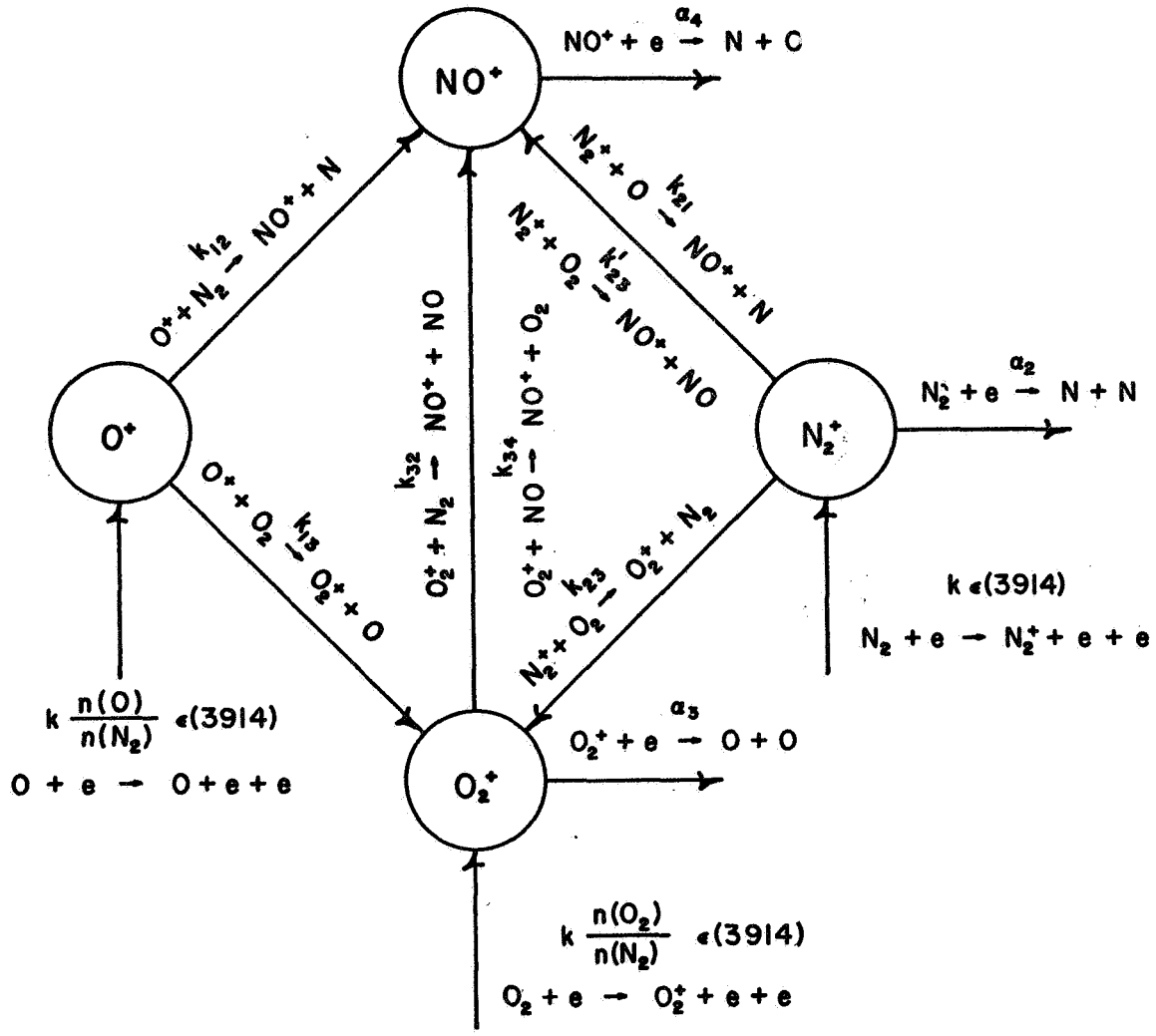

Figure 35. Ion Chemistry Model used in discussion of the ion composition.

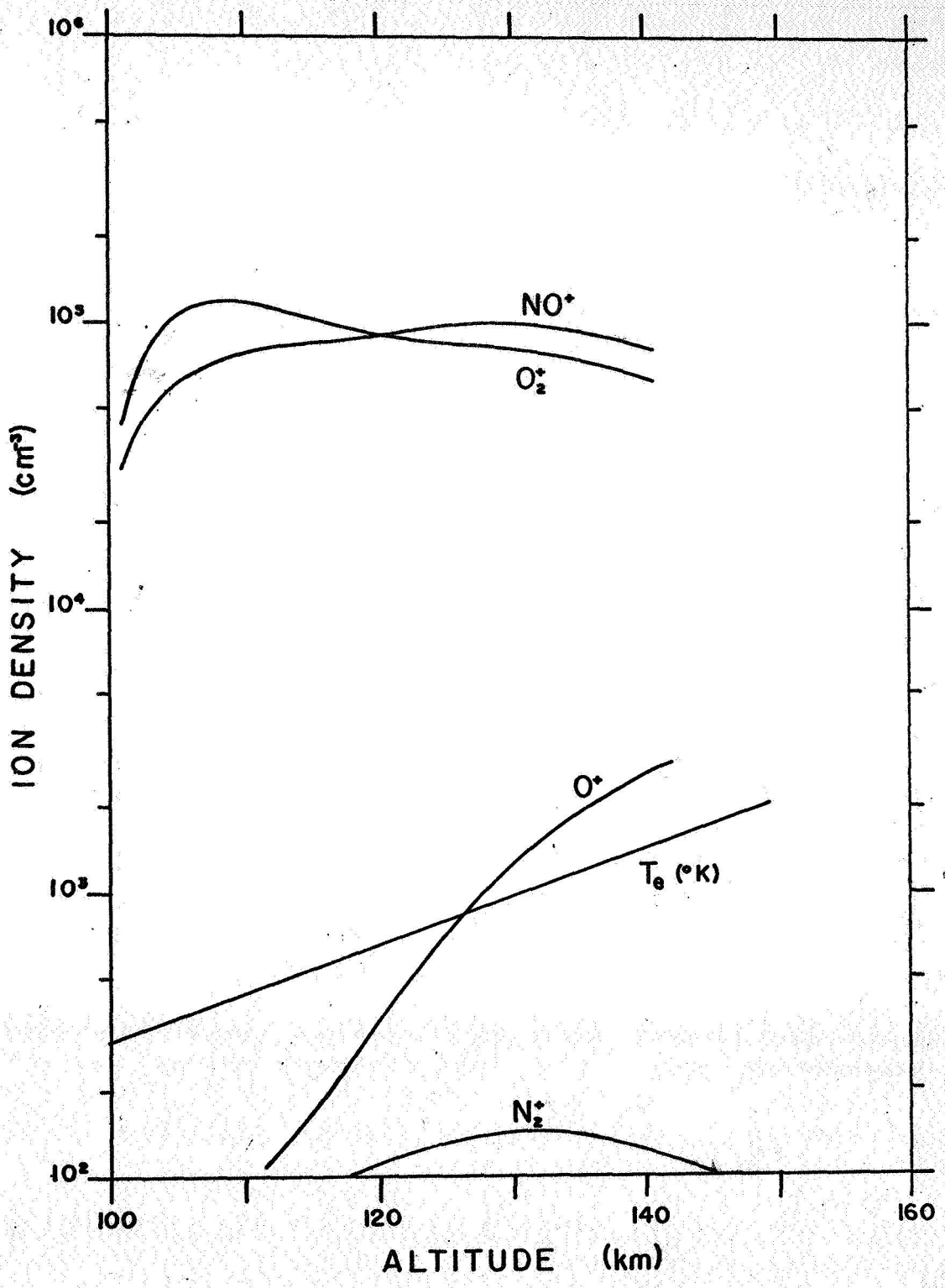

Figure 36. Ion composition expected using conventional ion chemistry and recent values for reaction rate coefficients.

calculated using the accepted rate coefficients[51,64,65,66] and the other parameters indicated less any contribution from the charge exchange reaction

$$O_2^+ + NO \rightarrow NO^+ + O_2 \quad . \tag{53}$$

Ionization is derived from the measured λ3914 signal.[28]

Increasing the rate for k_{32} to a value of 4×10^{-13} (assuming a substantial increase in k_{32} for vibrational temperatures not exceeding 1200°K) instead of 10^{-15} gives the distributions as shown in Figure 37, which is much closer to that observed. A similar ion distribution can be obtained if the possibility of NO densities upwards of $10^8/cm^3$ at 120 km is accepted. Furthermore, if the calibration of the ion mass spectrometer is assumed high by the factor of about two to which the absolute calibration is believed, then the calculated distribution with k_{32} about 4×10^{-13} agrees quite well overall although not as well in detail (Figure 38). It should be noted that this decrease would also decrease the electron temperature at 140 km to about 400°K, and would decrease the contribution of dissociative recombination to the λ5577 signal in the region below 130 km (Figure 29). This discussion does not consider small quantities of atomic nitrogen which may be present. Should this be detected, it could alter the ion chemistry significantly.

3.5 A Fluctuation

On the upleg of the 1968 experiment, a sharp temporal and/or spatial variation was seen starting at 127 km. Figure 39 shows the

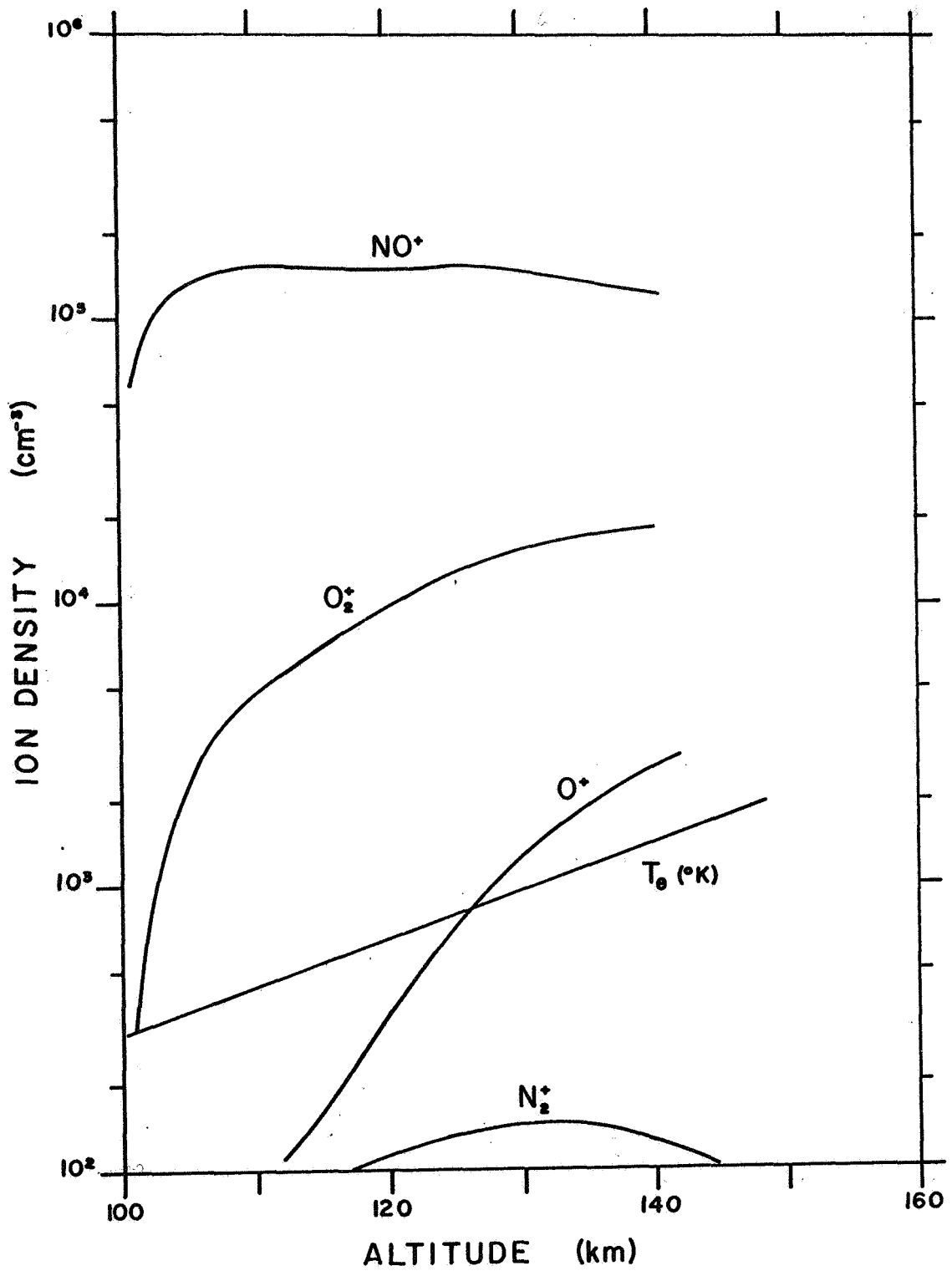

Figure 37. Ion composition expected with k_{32} increased from 10^{-15} $4 \times 10^{-13} cm^3/sec$.

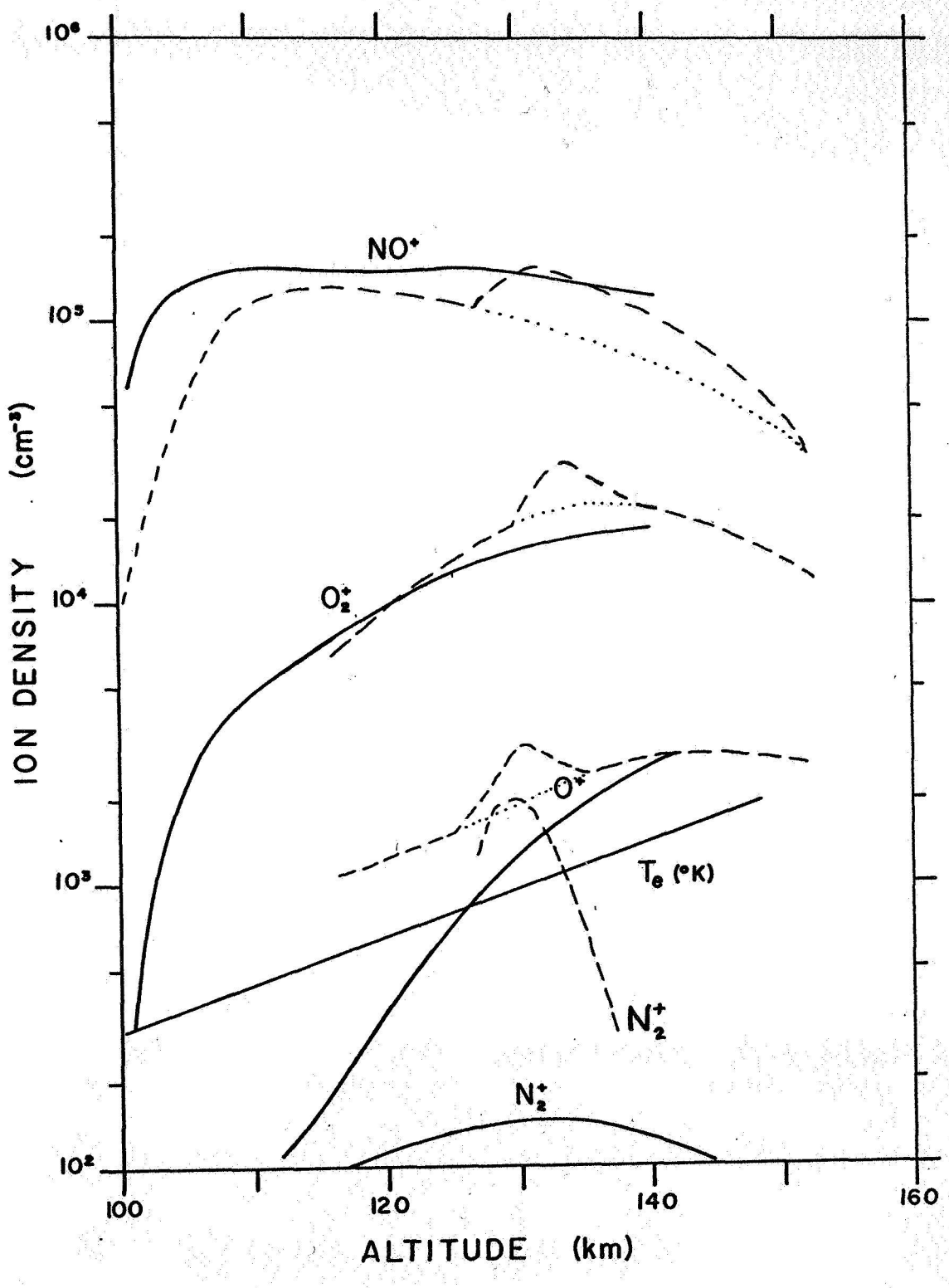

Figure 38. Ion densities from Figure 37 compared with the observed densities which have been decreased by a factor of 1.8.

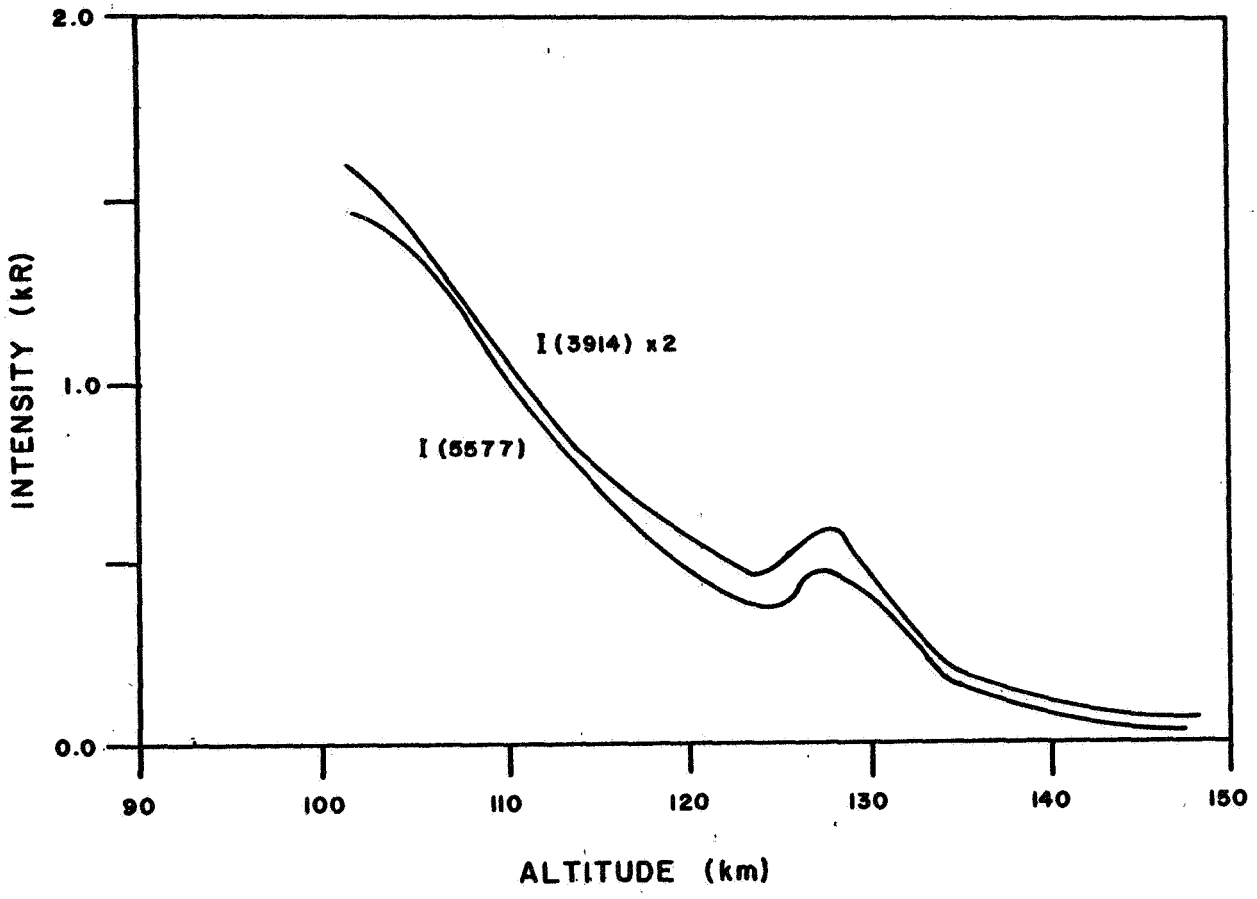

Figure 39. λ3914 and λ5577 intensities recorded on the upleg of the 1968 experiment. The fluctuation is clearly present.

integrated overhead intensities of the λ5577 and λ3914 emissions. The intensity enhancement is striking. When this data is considered with the mass spectrometer data, electron spectrometer data, and the up-down photometer data, a reasonably clear picture of what happened is obtained.

Figure 40 shows the up looking and down looking intensities recorded by the up-down photometer. Also shown is the O^+ ion data for reference to the ion data presented in Figure 33.

At the time the rocket was at about 122 km, the incoming flux increased about 100 percent; and this pulse of electrons slowly moved down the magnetic field lines reaching the rocket when the rocket was at about 127 km. At this point, a sharp increase in all ion densities in the vicinity of the rocket was observed; and for the first time, N_2^+ was seen (Figure 33). Also, the primary and secondary electron spectrometers showed a doubling of the total fluxes at this exact time.[29] No reduction has yet been done by Doering to see if the secondary spectra changed during this pulse. Finally, the pulse passed below the rocket where it was observed by the down looking observations of the up-down photometer. Figure 41 shows what occurred diagrammatically, with time increasing to the right. The arrows on the trajectory show orientation of the fields of view of the up-down photometer. The density of lines in the region shown for the pulse indicates total emission for the pulse only. The column on the right indicates the steady portion due to the initial constant flux.

The above qualitative discussion can be made quantitative with

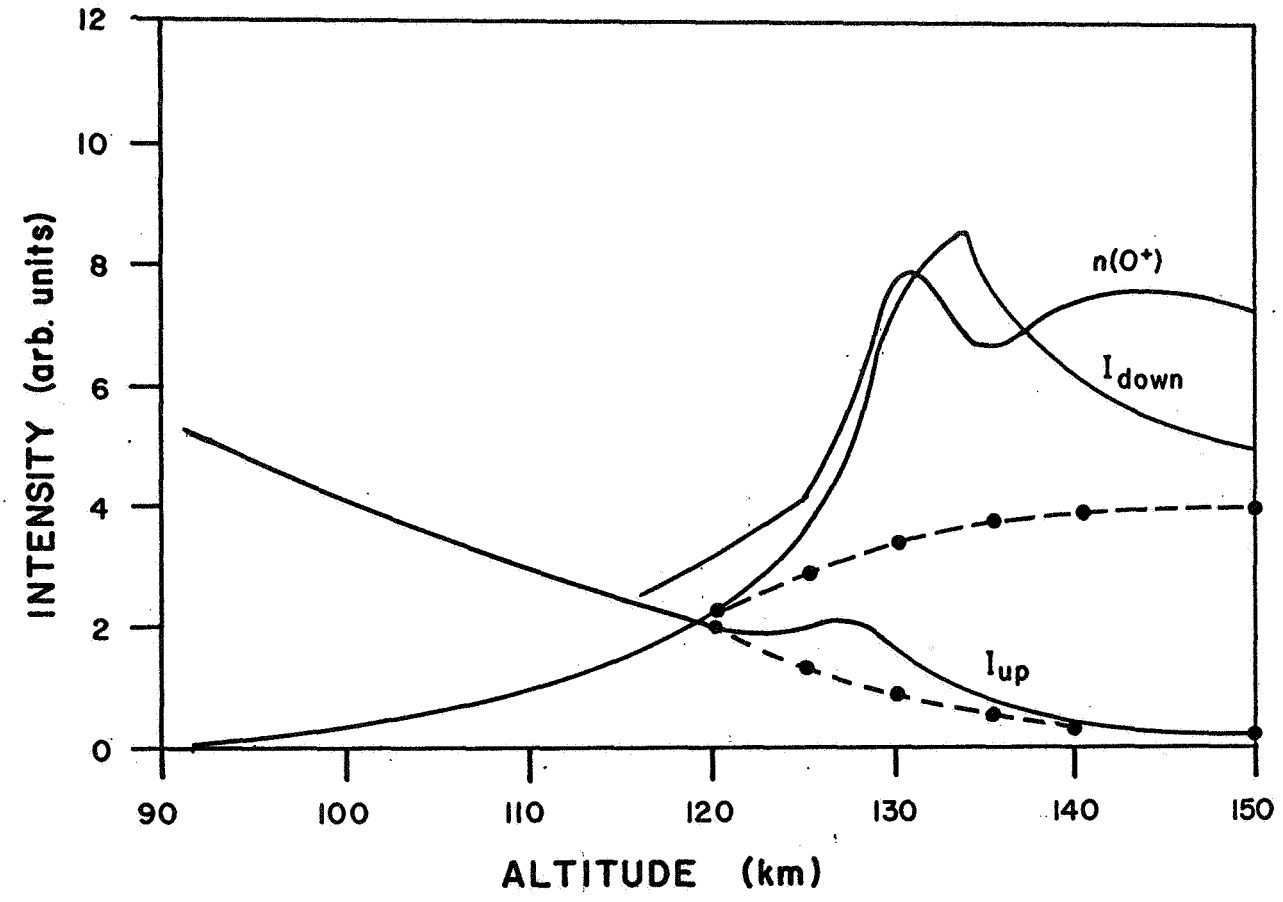

Figure 40. Up-down photometer signals and O^+ density. The enhancement below the rocket was clearly much later than that above. Dashed lines give calculated intensities expected had there been no fluctuation.

some assumptions. Column densities have been calculated from atmosphere Model VII. At 120 km, well before the pulse was seen, an average excitation cross section $\bar{\sigma}_{U-D}$ for the emissions observed by the up-down photometer (in arbitrary units) has been found from

$$I_{UP} = \int [.7\ n(N_2|Z)\Phi_{N_2} + .3\ n(O_2|Z)\Phi_{O_2}]\bar{\sigma}_{U-D}\ dZ \qquad (54)$$

where about 70 percent of the intensity I_{UP} is assumed to come from the N_2 second positive and Vegard-Kaplan systems,[30] and 30 percent is from λ2972 OI(^{1}S-^{3}P) which, at this altitude, is partially related to $n(O_2)$ by ionization and subsequent recombination, and partially by dissociative excitation (Section 3.3). Because of the different energy dependences of the excitation cross sections for the two species considered, separate total fluxes Φ_{N_2} and Φ_{O_2} were considered. Φ_{O_2} is the flux used in the earlier discussion which was derived from the λ3914 volume emission rate by Equation 13. Φ_{N_2} is the total flux in the energy interval from 11 ev to 100 ev which is the significant region for excitation of the second positive system which contributes most of the signal from N_2. After calculation, Φ_{N_2} was found to be about the same as Φ_{O_2}, and they have been considered equal to Φ_T.

With $\bar{\sigma}_{U-D}$, the up intensity for any altitude could be calculated from

$$I_{UP}(Z) = [.7\ \bar{n}(N_2) + .3\ \bar{n}(O_2)]\bar{\sigma}_{U-D}\ \Phi_T \qquad (55)$$

where $\bar{n}(N_2)$ and $\bar{n}(O_2)$ are the column densities at altitude Z. Figure 40 shows the values obtained in the region of the pulse. These are in excellent agreement with expectations had no pulse been observed, especially after complete transit of the pulse (above 140 km).

Once $\bar{\sigma}_{U-D}$ was found from the upward intensity at 120 km, the effective downward column density $\bar{n}_D$ at the same altitude was found from

$$I_{down} = \bar{\sigma}_{U-D} \Phi_T \bar{n}_D \tag{56}$$

The down intensity could then be calculated from

$$I_{down}(Z) = \Phi_T \bar{\sigma}_{U-D} [\bar{n}_D + .7 \Delta\bar{n}(N_2) + .3 \Delta\bar{n}(O_2)] \tag{57}$$

where $\Delta\bar{n}(X)$ is the column density of species X at 120 km less the column density at altitude Z. Figure 40 also shows the calculated downward intensity. At 150 km, it appears there are still some effects from the pulse.

Referring back to Figures 39 and 40, it appears that between 122 and 124 km, the pulse shows about 20 percent of the total increase it caused at 127 km. Thus, when the rocket is at about 123 km, the bottom edge of the pulse is at an altitude where the column density is 20 percent that found at 127 km. From the model, this is about 150 km.

At about 134 km, the down looking photometer shows that the leading edge of the pulse is being extinguished. This allowed positioning of the leading edge of the pulse in Figure 41.

The shape of the pulse is pretty clearly indicated by the N_2^+ signal. Figure 42 shows the relative primary flux measured during

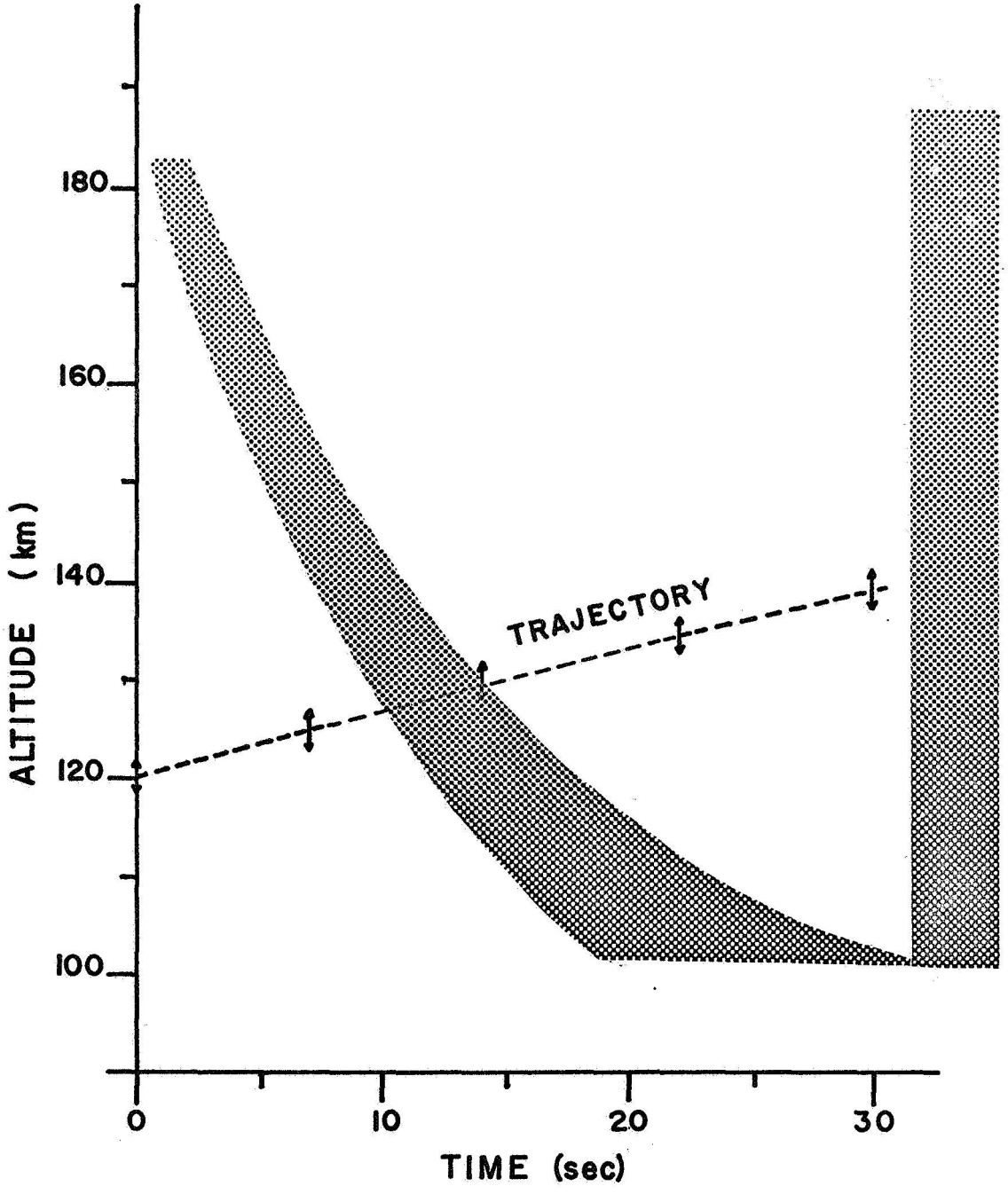

Figure 41. The pulse is shown to descend slowly into the atmosphere as the rocket continues toward apogee.

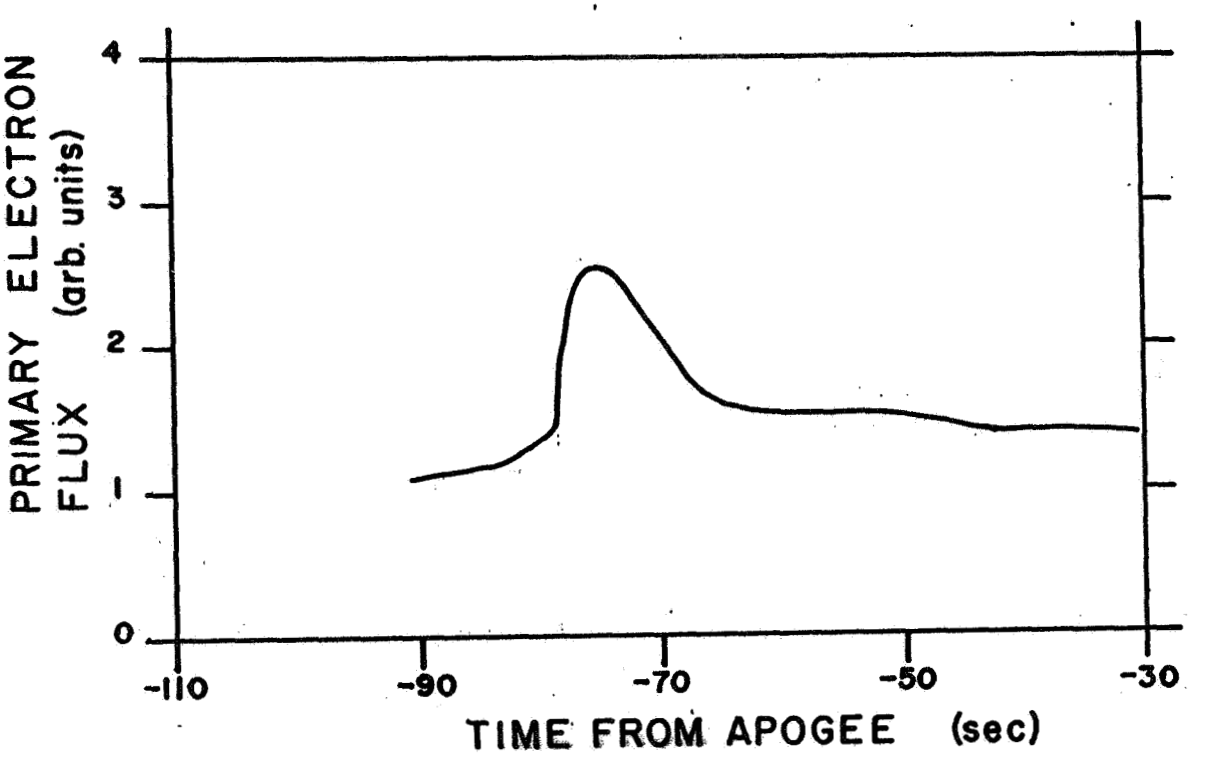

Figure 42. The bump shown is the primary electron flux measured when the pulse passed the rocket.

flight by Doering's primary electron spectrometer. The trailing edge is difficult to place in Figure 41 because of the slower cutoff of the pulse. Also, it is not yet clear that the pulse was of uniform extent throughout its descent into the atmosphere. The calculation of the down intensity indicates that a vertical spatial spreading of the pulse could cause the discrepancy noted at 150 km. There could also be a slight spatial variation on top of this obvious temporal pulse.

A most interesting feature of this pulse is the slow velocity with which it entered the emitting atmosphere. If the leading edge of the pulse as drawn in Figure 41 is assumed reasonable, then at 140 km the pulse was moving down at about 5 km/sec. The velocity appears to decrease as it penetrates to about 100 km.

The data shows the pulse to be primarily of temporal origin. Purely spatial variations seem unlikely since the rocket trajectory was well aligned with the magnetic field lines during this portion of the flight. A ground based photometer saw an increase of 30 percent in the λ3914 signal at the appropriate time. That this signal did not double can be attributed to several possible factors. The ground photometer was not necessarily pointed in line with the rocket. It was aimed at the predicted point for an altitude of 100 km. More important, the field of view of the photometer covered a much larger area of the emitting layer than did the rocket borne photometers. This may indicate a patchiness in the aurora and hence that more of the fluctuation should be attributed to a local spatial variation than has been.

4.0 CONCLUSION

The data discussed in Chapter 3, gives a rather complete picture of the excitation mechanisms of the prominent emission features of the aurora. Electron impact ionization of N_2 resulting in the first negative emissions of N_2^+, as proposed by Bates,[6] is shown to be completely compatible with laboratory measurements of the excitation cross section and measured electron spectra of energy less than 2 kev. The apparent error in calibration of the flight electron spectrometer was such that more first negative emission was expected than was observed. The correction to the absolute calibration that was made is reasonable. The use of the volume emission rate of the λ3914 (0-0) band as the source of a total incoming flux has been shown to be most useful.

The first and second positive emissions of N_2 are also excited by electron impact. The calculated cross section for excitation of $N_2(C^3\Pi_u)$ state is realistic.[35,36] The cross section which is calculated for the $N_2(B^3\Pi_g)$ state[35,36] needs to be enlarged by a factor of three to be in agreement with Broadfoot and Hunten's[39] ratio of second positive emission to first positive emission. The increase will be even larger to agree with others.[38,40] Further investigation of the second positive-first positive emission ratio seems warranted, especially if measurements of the vibrational temperature indicated by each system can be included.

The source of the most prominent feature of the aurora, the λ5577 green line, has been shown to involve O_2 rather than O. Direct electron impact excitation of the $O(^1S)$ state as suggested by Seaton[8] is

shown insufficient when measured fluxes are considered. Independently, the excitation ratio of $O(^1D)$ to $O(^1S)$ at 165 km is also shown to be incompatible with direct electron excitation and in good agreement with dissociative recombination. Dissociative excitation, rejected by Donahue et al.,[28] has been re-examined and the objections have been removed by examination of the O_2^+ first negative emissions and by considering dissociative recombination to be important starting about 125 km and becoming more dominant as the altitude increases. Pulsating auroras also indicate the low altitude dominance of dissociative excitation. Laboratory measurement of the cross section for dissociative excitation of the $O(^1S)$ state is most urgent. There is definite need of confirmation of the large value of $6 - 10 \times 10^{-17} cm^2$ observed in the aurora.

Compared to nitrogen, the first negative system of O_2 has been neglected in the laboratory studies. The agreement of the little that is discussed here is heartening. The biggest puzzle is the apparent decrease of the excitation cross section of the (2-0) band with respect to the (1-0) band seen in 1967.

The ion composition of the emitting regions of the aurora is unexplained in terms of the conventional ion chemistry. A process which decreases O_2^+ and increases NO^+ is necessary. Charge exchange with neutral NO is reasonable only for high densities of NO. It is suggested that an increase of the reaction rate for O_2^+ on vibrationally excited N_2 producing NO^+ could be the needed process if vibrational temperatures in excess of 1200°K are not required. Further investigation of the neutral atmosphere, including NO and N measurements, is necessary. Should

large quantities of NO be found, a source will also have to be found.

The use of the up-down photometer in analysis of fluctuations has been demonstrated. It is clearly an essential instrument on any rocket probe of the aurora. Discussion of the bilayering observed in the 1966 experiment would have been more complete, and perhaps solved, had an up-down photometer been present on that experiment. The joint Johns Hopkins University-University of Pittsburgh payload as flown in 1968 is a complete auroral experiment. Its ability to measure most of the important parameters for the quantitative study of the aurora has been demonstrated by the rather complete picture of the atomic and molecular physics of the aurora which is discussed in this dissertation. Further experiments will permit it to add the ion chemistry of the aurora to its list of accomplishments.

APPENDIX A: THEORETICAL CONSIDERATIONS APPLICABLE TO INTERFERENCE FILTER PHOTOMETERS

A simple photometer consists of an aperture system to define that portion of the emitting surface from which it accepts light, a filter to isolate the desired spectral feature, and a suitable detector to convert the light signal into a usable electric signal. The interference filter is commonly used for narrow band applications in the visible, near ultraviolet, and near infrared.

The basic principle applied in interference filters is multiple beam interference. In modern narrow band pass filters, alternate layers of high and low refractive index dielectrics are evaporated onto a glass substrate. The thickness of the coatings determines the ultimate peak wavelength (wavelength for which the transmission is a maximum), band-pass (width in Å at one half the maximum transmission), and maximum transmission. Figure 43 shows a typical curve for a nominal 10 Å band pass filter for normal incidence light. Often the substrate and cover glass are themselves wide band pass or cut off type glass filters. Their use is necessary to prevent transmission of nearby orders.[67,68]

Interference filters are temperature sensitive due to the thermal expansion properties of the dielectric layers. $\Delta\lambda/\Delta T$ is positive, with variable values in the neighborhood of an Ångström unit per several degrees Kelvin. Exact values are, of course, dependent upon the particular filter. The filters can also show aging, especially the very narrow band pass ones. The peak wavelength will decrease with age. The peak wavelength of a nominal 3 Å band pass filter can shift 3 Å in only a few months.[69]

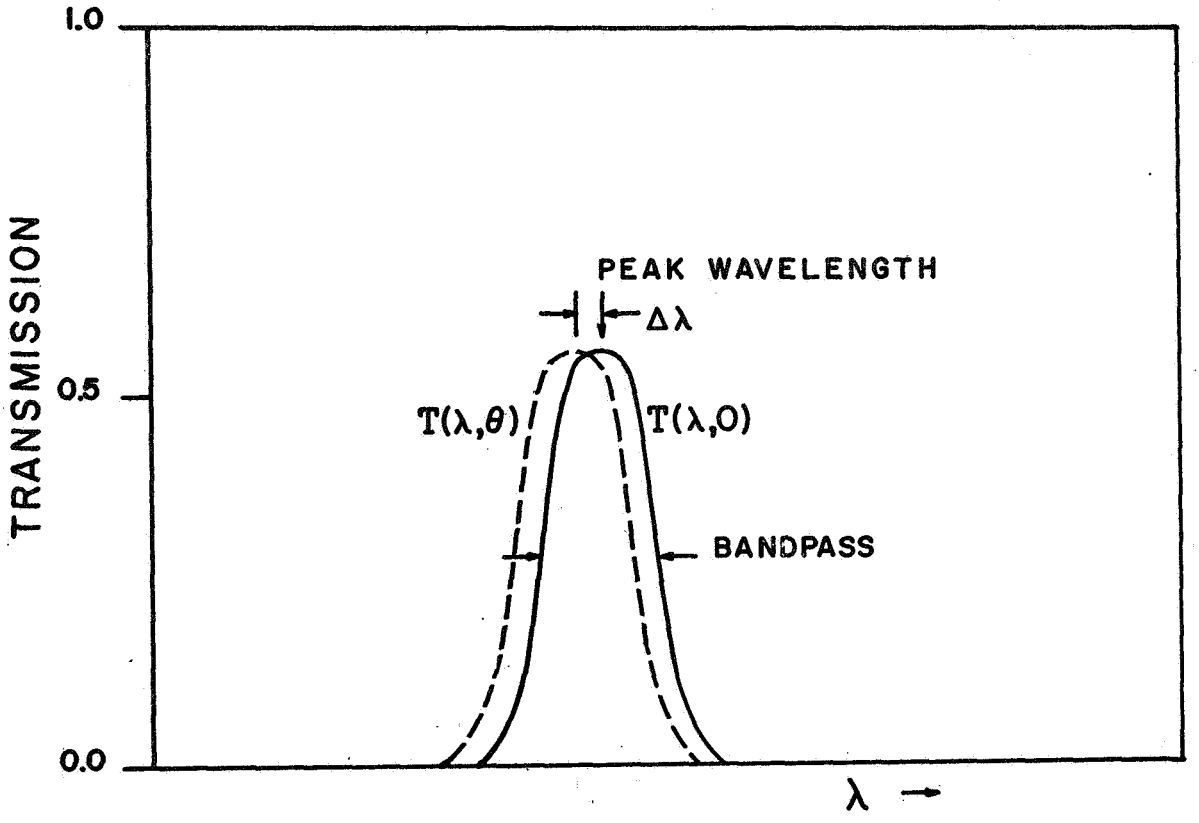

Figure 43. A typical transmission curve for a narrow bandpass filter. Also shown is the shift for non-normal incidence.

For multiple beam interference, the wavelength passed is dependent upon the angle of refraction θ' in the interfering media as given by the multiple beam interference formula

$$\lambda = 2\, n't \cos\theta' = \lambda_o \cos\theta' \qquad (58)$$

It is at once apparent that oblique incidence will cause a shift toward shorter wavelengths. This important result warrants further discussion.

Applying the small angle approximation

$$\Delta\lambda = \lambda - \lambda_o = -\lambda_o \frac{\theta'^2}{2} \qquad (59)$$

From Snell's law, the angle of incidence θ of light on the filter is related to θ' by

$$\theta' = \theta/n' \qquad (60)$$

considering n = 1 for air. Thus

$$\Delta\lambda = -\frac{\lambda_o\, \theta^2}{2\, n'^2} \qquad (61)$$

The commonly used formula for the shift of band pass is

$$\Delta\lambda = -\frac{\lambda_o\, \theta^2}{6} \qquad (62)$$

The transmission of the filter $\tau(\lambda,\theta)$ becomes $\tau[\lambda(1+\frac{\theta^2}{6})]$ as illustrated in Figure 43. Table VIII gives some values of $\Delta\lambda$ at commonly used λ_o for several values of θ.

In a photometer, the value of θ varies from 0 to some θ_{max} which is determined by the aperture system. In the simplest use, the aperture

TABLE VII

Bandpass shifts (in Å for interference filters as a function of wavelength and angle of incidence.

θ_{max}	f/4 7.3°	f/5 5.8°	f/6 4.8°	f/8 3.6°	f/10 2.9°	f/12(lens) 2.4°
3370Å	8.8	5.6	3.9	2.2	1.4	.98
3914Å	10.	6.5	4.5	2.6	1.6	1.7
5577Å	14.	9.3	6.4	3.6	2.3	1.6
6300Å	16.	10.	7.3	4.1	2.6	1.8
6685Å	17.	11.	7.7	4.4	2.8	1.9
7774Å	20.	13.	9.0	5.1	3.2	2.2
8446Å	22.	14	9.8	5.5	3.5	2.4

system is merely two circular holes separated by a distance D (Figure 44). For this system

$$\theta_{max} = \tan^{-1} \frac{a+a'}{D} \quad . \tag{63}$$

A great improvement can be had by using two lenses of identical focal length D placed at the apertures (Figure 45). The objective lens focuses a real image of the sky at the field lens. This lens then produces a virtual image on top of its object (the image from the objective lens). The maximum angle any light ray makes on leaving the field lens is

$$\theta_{max} = \tan^{-1} a/D \quad . \tag{64}$$

Figure 45 shows how light rays traverse the system, using simple thin lens geometric optics. It can also be seen from Figure 45 that the virtual image formed by the field lens emits into the solid angle

$$\Omega = \pi \, a^2/D^2 \quad . \tag{65}$$

The lens system allows much larger apertures to be used since its θ_{max} is about one-half that of the no-lens system. For the same θ_{max} the lenses give an increase of photon gathering power by a factor of 16 at the cost of no more than .8 from the transmission of the two lenses. The use of proper antireflectance coatings on the lenses almost completely removes these transmission losses, especially in the visible region of the spectrum.

Consider a detector system such as a photomultiplier tube and appropriate electrometers. The three characteristics of interest in the tube are the quantum efficiency $Q(\lambda)$ which depends on wavelength,

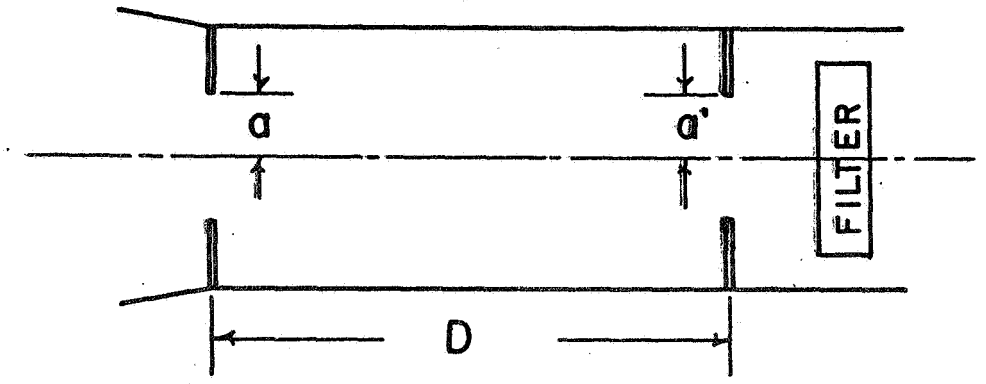

Figure 44. Simple aperture system for a photometer.

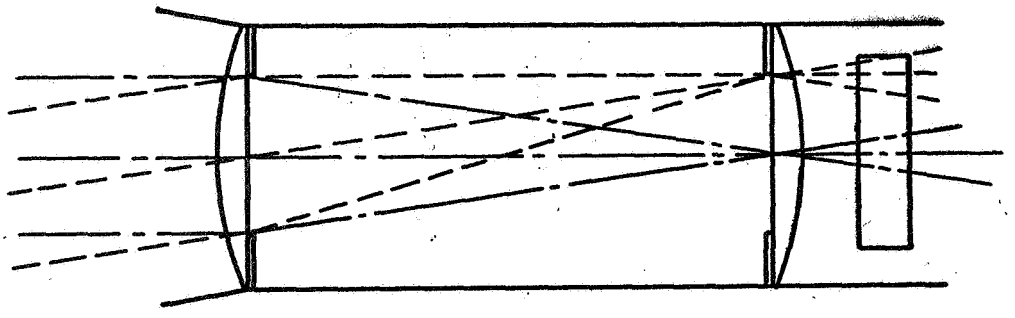

Figure 45. The use of lenses of focal length D gives a factor of 16 increase in light gathering ability for a given θ_{max}. Simple ray tracing is shown for the extreme rays.

the gain g which depends on the high voltage applied to the tube, and the dark current I_D which depends on the gain and the temperature of the photocathode. Figures 46 and 47 show these parameters for a typical EMR 541E-01 photomultiplier tube.[70] Note the approximate straight line dependence of g and I_D when plotted on log-log scales.

The dark current of photomultiplier tubes is sensitive to mechanical shocks and light shocks. Extreme vibrations can cause a tremendous increase in dark current, and has caused complications in analysis of some rocket borne experiments (Section 2.4). Light shocks occur from exposure of the photocathode to large photon fluxes. Time constants for recovery from both types of shocks can be several hours. It should also be noted that cooling of the photocathode will also decrease the dark current. Photomultiplier tubes in laboratory use have shown dark current decreases by factors of nearly 100 after prolonged, continuous cooling to dry ice temperatures.

Putting the system together, we have a unit as shown schematically in Figure 48. An exact solution for the photoelectrons produced will be indicated in full detail. Light from a source of surface brightness $B(\lambda)$ in units of photons per square centimeter per second per steradian per Ångström passes through area elements dA and dA' spaced d apart, through the filter at angle θ, and on to the photocathode of the photomultiplier tube. The number of photoelectrons emitted by the cathode to be seen as signal is

$$N = \int_A \int_{A'} \int_\lambda B(\lambda) \frac{dA\, dA'}{d^2} \tau_{lens}^2(\lambda) \tau[\lambda(1-\frac{\theta^2}{6})] Q(\lambda) d\lambda \quad , \quad (66)$$

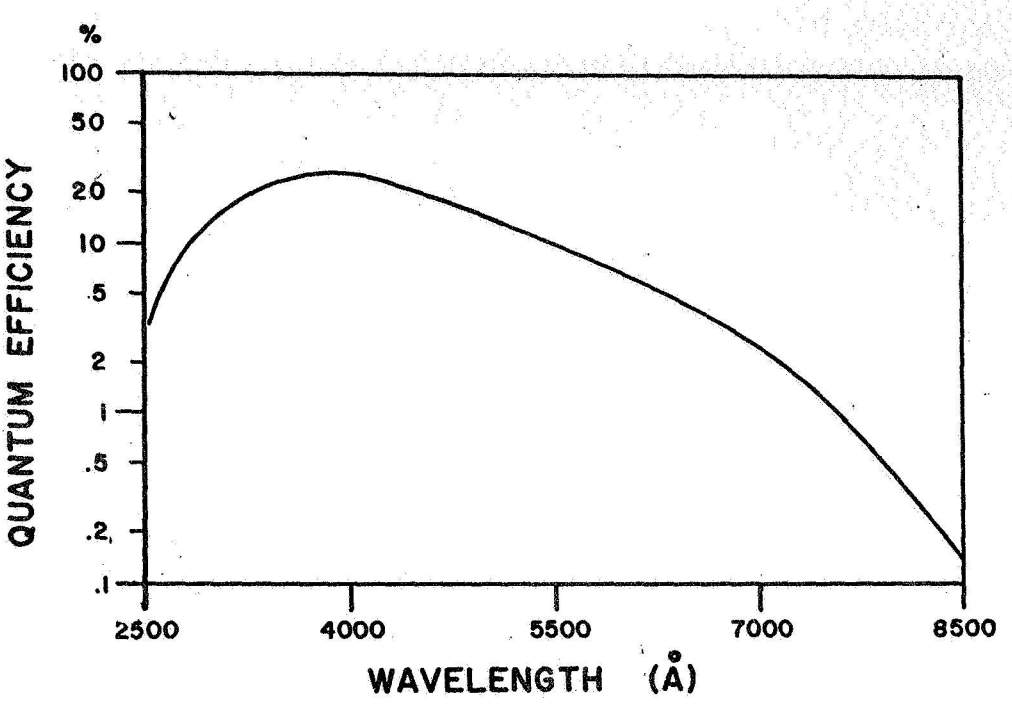

Figure 46. Typical quantum efficiency of an EMR 541E photomultiplier tube.[70]

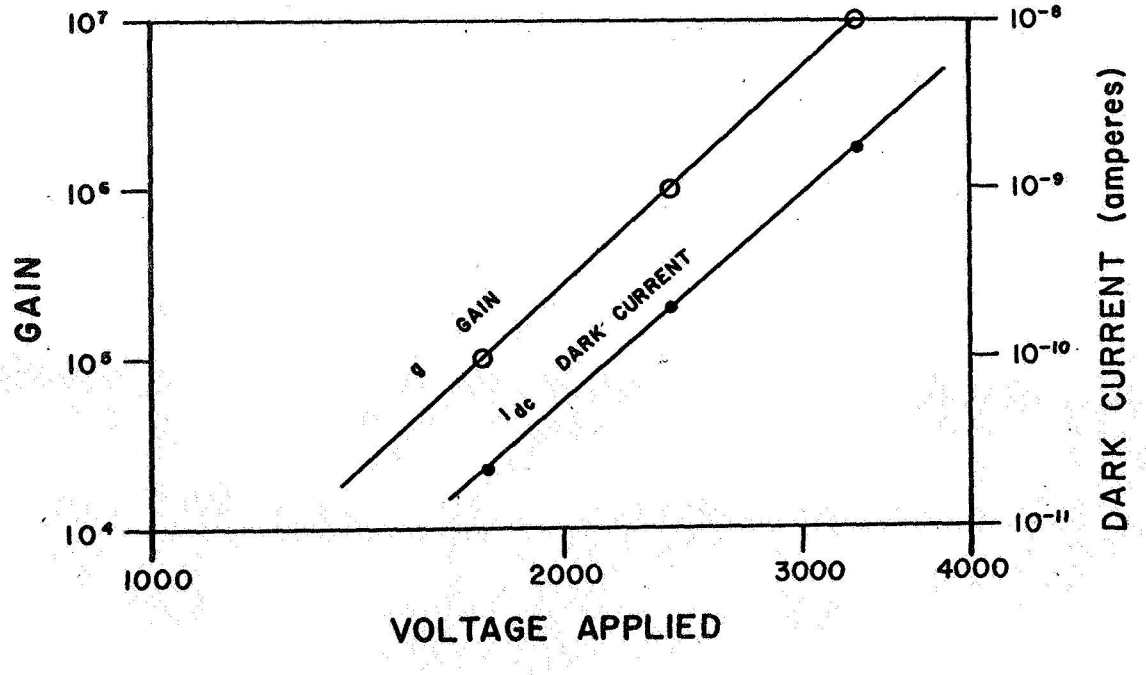

Figure 47. Typical gain and dark currents of an EMR 541E photomultiplier tube.[70]

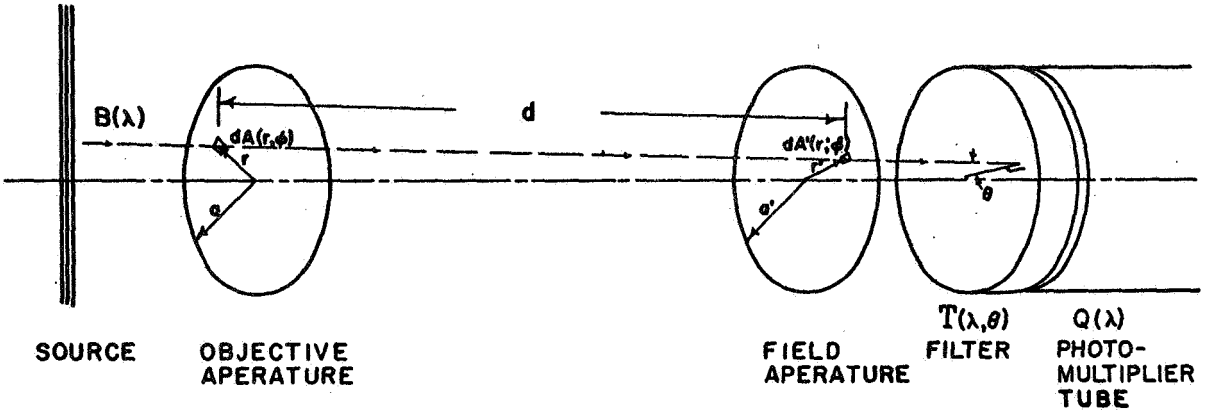

Figure 48. Elements of a complete photometer. A light ray from the source $B(\lambda)$ is traced through the system.

Since lenses are being used

$$\theta = \tan^{-1} r/D \tag{67}$$

and the full expression for N is

$$N = \int_0^{2\pi} d\phi \int_0^a r\,dr \int_0^{2\pi} d\phi' \int_0^{a'} r'\,d\,r' \int_0^{\infty} d\lambda \; \frac{B(\lambda)\, \tau_{lens}^2(\lambda)\, \tau[\lambda(1-\frac{\theta^2}{6})]Q(\lambda)}{D^2 + r^2 + r'^2 - 2\, r\, r' \cos(\phi-\phi')} \,. \tag{68}$$

By examination of Equation 68, the parameters of the photometer are chosen for optimum performance. a, a', 1/D, $\tau_{lens}(\lambda)$, and $Q(\lambda)$ should be as large as possible consistent with the effects of θ_{max} on the λ integration and dark current on the signal to noise ratio. Notice that because of Equation 67 the contribution to N due to the r integration is larger as r increases. Thus, most of the light enters the filter obliquely. It is also desirable to have maximum peak transmission of the filter, considering carefully the background continuum and the necessary isolation of the spectral feature to be observed.

In practice, several approximations are applied to the multiple integral given for N in Equation 68. First, the integration over the apertures gives the geometric factor as $\pi^2 a^2 a'^2/D^2$. When this is done, $\tau[\lambda(1-\frac{\theta^2}{6})]$ becomes $\bar{\tau}(\lambda)$, some average chosen to account for the θ dependence. With these simplifications, N becomes

$$N = \frac{\pi^2 a^2 a'^2}{D^2} \int_0^{\infty} B(\lambda)\, \bar{\tau}(\lambda)\, Q(\lambda)\, \tau_{lens}^2(\lambda)\, d\lambda \,. \tag{69}$$

At this point, two types of $B(\lambda)$ must be considered as extremes. The first is for a continuum source such as the standard lamp used for calibration. In this case λ_o is considered the peak wavelength of the narrow-bandpass filter. The λ integration then becomes

$$B(\lambda_o)\ Q(\lambda_o)\ \tau_{lens}(\lambda_o) \int_o^\infty \bar{\tau}(\lambda)\ d\lambda \quad , \tag{70}$$

and the factors moved outside the integral are considered constant over the relatively narrow bandpass of the filter. The last integral above can also be replaced by

$$\Delta\lambda = \int_o^\infty \bar{\tau}(\lambda)\ d\lambda \quad , \tag{71}$$

which would then be the bandpass of a filter with 100 percent transmission and square cutoffs. This term must be used carefully and is not a replacement for the real bandpass of the filter. Thus, for a continuum source

$$N = \frac{\pi^2 a^2 a'^2}{D^2}\ B(\lambda_o)\ Q(\lambda_o)\ \tau^2_{lens}\ (\lambda_o)\ \Delta\lambda \quad . \tag{72}$$

The second consideration is for a line emission where the brightness is given by a delta function

$$B(\lambda) = B\ \delta(\lambda-\lambda_o) \quad . \tag{73}$$

Here also the quantum efficiency and transmission of the lens are considered constants. The λ integration to be performed is

$$\int_o^\infty B\ \delta(\lambda-\lambda_o)\ \tau(\lambda)\ d\lambda \tag{74}$$

yielding

$$B\ \bar{\tau}(\lambda_o) \quad . \tag{75}$$

In this case, we may make use of Equation 68 and write

$$\bar{\tau}(\lambda_o) = \int_o^a \frac{2r\ dr}{a^2}\ \tau\ \lambda_o\ \ 1 - \frac{(\tan^{-1} r/D)^2}{6} \quad , \tag{76}$$

which explicitly includes the proper correction for angular dependence of the filter transmission. For the line source,

$$N = \frac{\pi a^2 a'^2}{D^2}\ \ B\ Q(\lambda)\ \tau^2_{lens}(\lambda)\ \bar{\tau}(\lambda_o) \quad . \tag{77}$$

With these two extreme, but practical, simplifications, discussion can proceed to the actual signal from the photometer. The current from the photomultiplier tube will consist of two parts; one is the constant dark current and the other is from the signal N just calculated above, Hence,

$$I = Nge + I_D = N_T ge \quad , \tag{78}$$

where g is the gain of the photomultiplier tube and e the charge on an electron. The dark current can be written as the spontaneous emission rate of electrons from the photocathode

$$N_D = I_D/ge \quad . \tag{79}$$

Both the spontaneous emission of electrons from the photocathode and emission of photons from the source $B(\lambda)$ are random processes and will have fluctuations. If N counts are made in a given time, the associated

fluctuations are $\sqrt{N}$.

For the photometer we must find an appropriate time over which N and N_D can be compared to give a meaningful signal to noise ratio. The only natural time in the system is the time constant T of the electrometer. This is a very reasonable time to use for the purpose since it is roughly the time for which the signal is averaged before it is seen on the output. For the noise analysis we now use

$$n = N\,T\ , \tag{80}$$

$$n_D = N_D\,T\ , \tag{81}$$

and

$$n_T = N_T\,T\ . \tag{82}$$

The noise signal is $\sqrt{n_T}$. Thus, the signal to noise ratio S is

$$S = \frac{n}{\sqrt{n_T}} = \frac{N\sqrt{T}}{\sqrt{N+N_D}}\ . \tag{83}$$

Table IX gives some values of S for various values of N, N_D, and T. It is clear that it is desirable to maximize N and minimize N_D. Also, T should be as large as possible without compromising the desired time resolution.

In spite of the detail of the calculations done in this Appendix, it should be noted that when the photometer is put together and calibrated absolutely, there may be variations of perhaps a factor of two between calculated and actual sensitivity. This is due to unavoid-

TABLE IX

Signal to noise ratio.

Time constant of amplifier (sec)	Dark current counting rate (sec^{-1})	Total counting rate (sec^{-1}) 10^2	10^3	10^4	10^5	10^6
.001	20	.29	.99	3.16	10.00	31.62
	59	.26	.98	3.16	10.00	31.62
	100	.22	.95	3.15	10.00	31.62
	200	.18	.91	3.13	9.99	31.62
	500	.13	.82	3.09	9.98	31.62
	1000	.10	.71	3.02	9.95	31.61
	2000	.07	.58	2.89	9.90	31.59
	5000	.04	.41	2.58	9.76	31.54
.002	20	.41	1.40	4.47	14.14	44.72
	50	.36	1.38	4.46	14.14	44.72
	100	.32	1.35	4.45	14.14	44.72
	200	.26	1.29	4.43	14.13	44.72
	500	.18	1.16	4.36	14.11	44.71
	1000	.14	1.00	4.26	14.07	44.70
	2000	.10	.82	4.08	14.00	44.63
	5000	.06	.58	3.65	13.80	44.61
.005	20	.64	2.21	7.06	22.36	70.71
	50	.58	2.18	7.05	22.36	70.71
	100	.50	2.13	7.04	22.35	70.71
	200	.41	2.04	7.00	22.34	70.70
	500	.29	1.83	6.90	22.30	70.69
	1000	.21	1.58	6.74	22.25	70.68
	2000	.15	1.29	6.46	22.14	70.64
	5000	.10	.91	5.77	21.82	70.54
.010	20	.91	3.13	9.99	31.62	100.00
	50	.82	3.09	9.98	31.62	100.00
	100	.71	3.02	9.95	31.61	100.00
	200	.58	2.89	9.90	31.59	99.99
	500	.41	2.58	9.76	31.54	99.98
	1000	.30	2.24	9.54	31.57	99.95
	2000	.22	1.83	9.13	31.31	99.90
	5000	.14	1.29	8.16	30.86	99.75

ably coarse interpolations and errors on parameters supplied by the manufacturer of components and other small uncertainties. Should the calculated results be much further off than this, a thorough check of both the calculations and calibration should be made.

APPENDIX B: OPTICAL CALIBRATION WITH A TUNGSTEN RIBBON FILAMENT LAMP

The following discussion concerns the use of a General Electric Type 30A/T24/13 lamp calibrated for brightness temperature as a function of current. The lamp is fitted with a 1 1/4 inch diameter quartz window and SR8A tungsten ribbon filament. In the region of the spectrum where the emissivity of tungsten is known, calculations are given which allow the lamp to be used as an absolute standard.

The lamp is used in the circuit shown in Figure 49. The calibration data from the National Bureau of Standards gives the brightness temperature viewed through the quartz window at a specified wavelength as a function of the current through the filament.[71] The desired current is supplied by a Kepco KS8-50M D. C. Power Supply with 0.05 percent regulation. This regulation is just sufficient. A Leeds and Northrup Model 4361 0.01 ohm (0.04 percent) 100 ampere resistor provides a voltage drop of 10 millivolts per ampere, which is measured by a Fluke Model 885AB Differential Voltmeter. Measurement to the hundredth of an ampere given by the NBS is necessary.

The brightness temperature is confirmed by a Leeds and Northrup Model 8632-C optical pyrometer. The pyrometer reads to $\pm 8°$ on the H range (1075°C to 1750°C) and on the xH range $\pm 14°$ at 1750°C to $\pm 18°$ at 2540°C. The pyrometer is used so that any gross change in the lamp, or of course the pyrometer, can be detected.

The brightness temperature T_B is defined from the Planck radiation law

$$W(\lambda_S, T_B) = \frac{C_1}{\lambda_S^5} \frac{1}{(e^{C_2/\lambda_S T_B} - 1)} , \qquad (84)$$

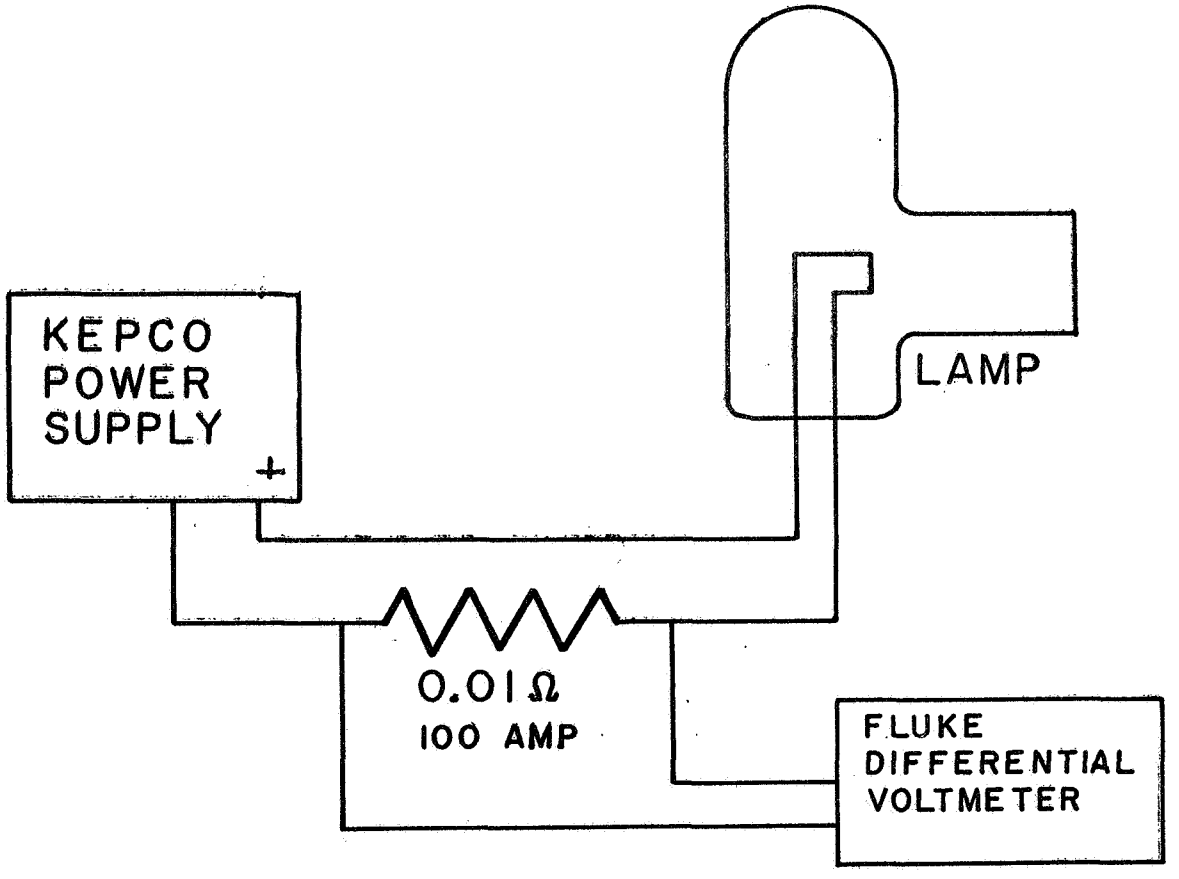

Figure 49. Circuit configuration used with the standard lamp.

where W is the emissive power in ergs per square centimeter per second per Ångström, C_1 and C_2 constants, and λ_S the wavelength at which W is measured. Thus the brightness temperature T_B would be the true temperature of a black body which radiates the same energy per square centimeter per second per Å at the wavelength λ_S.

The emissivity of a radiating surface at wavelength λ is defined by the ratio of the actual emissive power W' to the emissive power W of a black body at the same true temperature as the emitting surface,

$$\varepsilon(\lambda,T) = \frac{W'(\lambda,T)}{W(\lambda,T)} \quad . \tag{85}$$

Noting that $e^{C_2/\lambda T} >> 1$ for reasonable λ and T, and that a correction should be made since T_B is measured through a quartz window of transmission $\tau_Q(\lambda)$ (Figure 50),[72] the relationship between T_B and T is calculated to be

$$\mathrm{Ln}[\tau_Q(\lambda)\ \varepsilon(\lambda,T)] = \frac{C_2}{\lambda}\left(\frac{1}{T} - \frac{1}{T_B}\right) \quad . \tag{86}$$

For any desired wavelength λ with the filament at true temperature T, the emissive power is given by

$$W(\lambda,T) = \tau_Q(\lambda)\ \varepsilon(\lambda,T)\ \frac{C_1}{\lambda^5(e^{C_2/\lambda T} - 1)} \quad . \tag{87}$$

This energy is radiated into a hemisphere about the flat filament surface, preferentially in the direction normal to the surface. It decreases as the cosine of the angle to the normal for other viewing directions. As long as the cosine of the maximum viewing angle can be considered one,

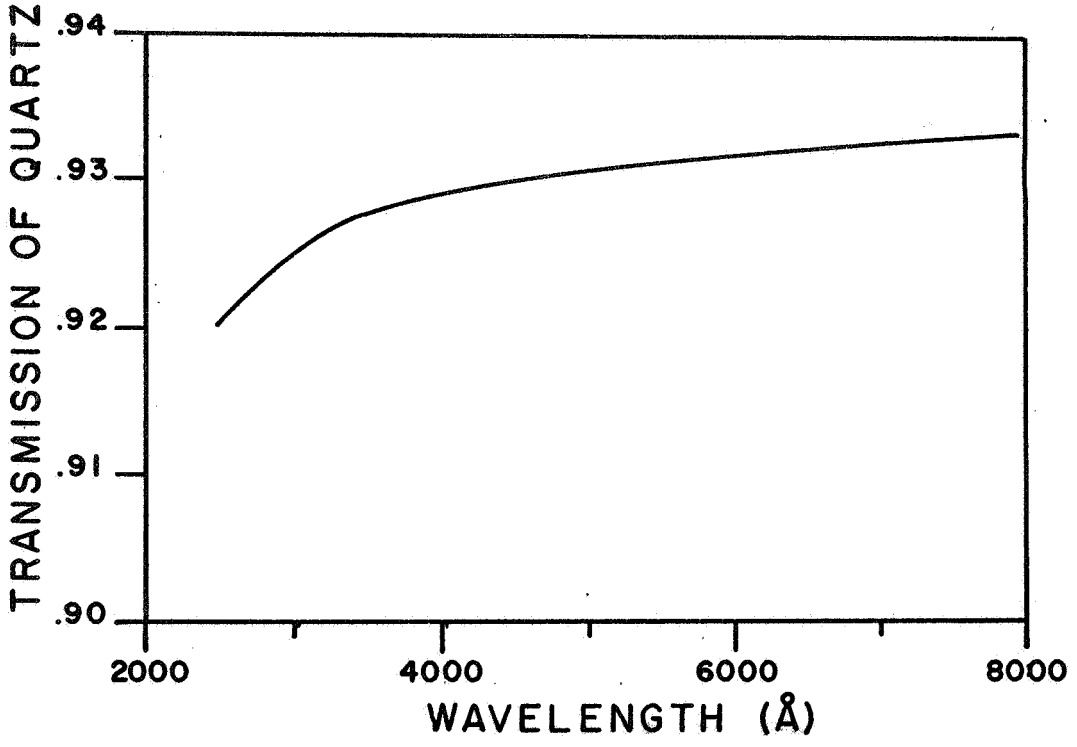

Figure 50. The transmission of fused quartz calculated from the index of refraction considering two surfaces and no absorbtion.

the surface brightness of the ribbon is given by

$$B(\lambda,T) = \frac{\tau_Q(\lambda)\ \ \varepsilon(\lambda,T)\ \ C_1}{\pi\ hc\ \ \lambda^4\ (e^{C_2/\lambda T} - 1)} \quad , \qquad (88)$$

where the division by $\frac{hc}{\lambda}$ has changed the units to photons per square centimeter per second per Ångström per steradian.

A computer program has been written which calculates $B(\lambda,T)$ for any brightness temperature (Figure 51). Table X gives the constants used for that computation. The program's use is somewhat limited, however, by the lack of sufficiently reliable measurements of the emissivity of tungsten.[73,75] For brightness temperatures of 1600°C and 1800°C, the emissivity as measured by Larrabee[75] is used. For 2200°C, the values found by DeVos[74] are used. See figure 52 for values used. The DeVos values are not corrected for scattered light and, as Larrabee points out, are probably a little high. The wavelength region extends from 2500Å to 9000Å. λ_S is 6530Å, as given on the NBS calibration sheet supplied when the lamp is absolutely calibrated.

There are two major sources of error in this system. One is obviously the values chosen for $\varepsilon(\lambda,T)$. Judging from the results shown in Figure 53, the quoted values of $\varepsilon(\lambda,T)$ vary by as much as 2 percent in the regions of interest. DeVos points out that different standards laboratories use different values. Thus, there is 2 or 3 percent uncertainty due to $\varepsilon(\lambda,T)$.

The other major source of error is in the calibration of T_B. The NBS calibration sheet gives the "uncertainties" in T_B to range from ±5° at 1100°C to ±10° at 2300°C. Considering $e^{C_2/\lambda T} >> 1$, the Planck

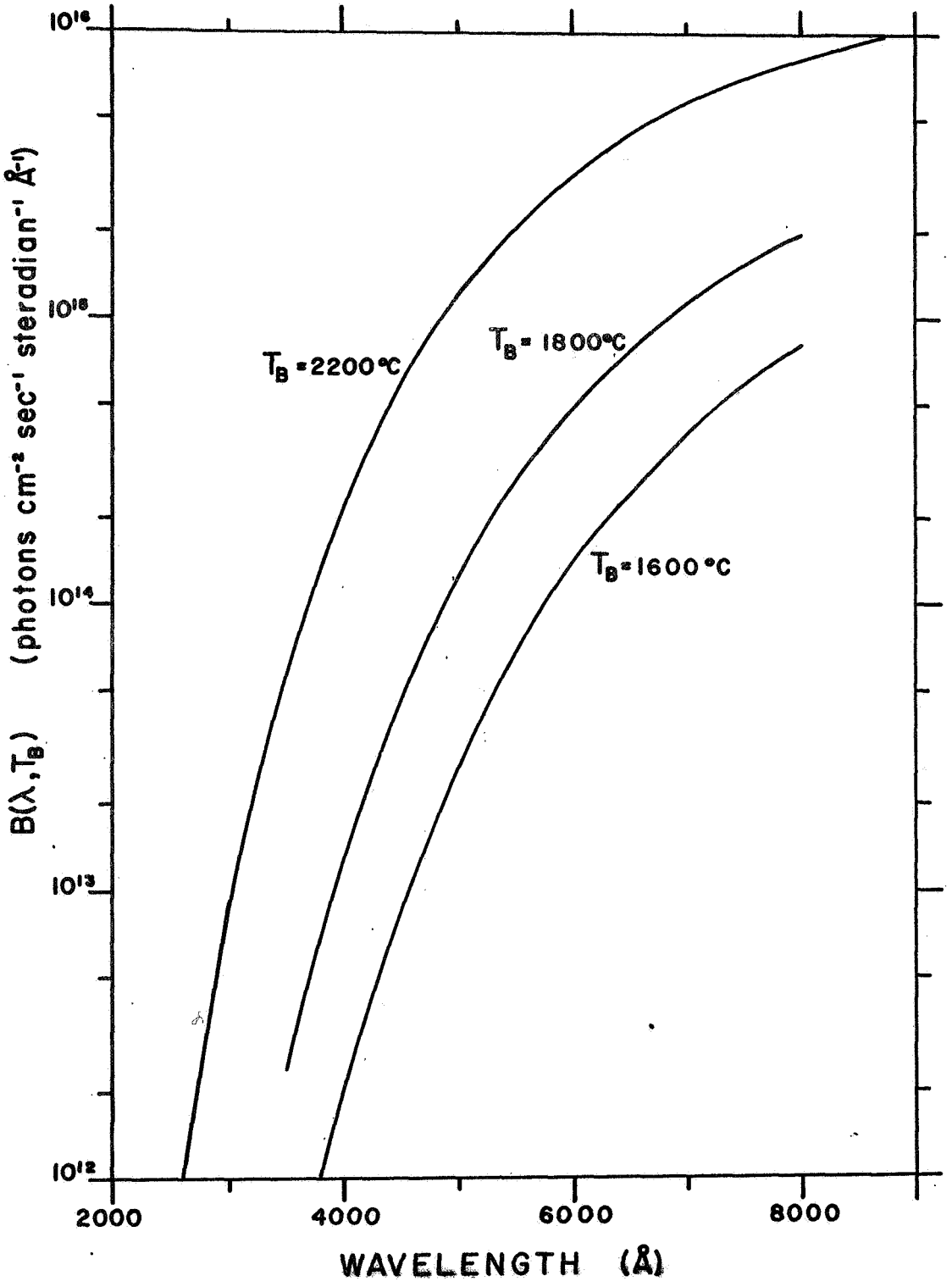

Figure 51. Surface brightness calculated for three brightness temperatures.

TABLE X

Constants used in calculation of $B(\lambda,T_B)$.

$c_1/hc = 8\ hc\ \frac{e}{4}\ \frac{1}{hc} = 1.8836 \times 10^3 cm^2/Å$

$c_2 = 1.4388\ cm°K$

$\lambda s = 6530Å$

$h = 6.6254 \times 10^{-27} erg\ sec$

$c = 2.9979 \times 10^{10} cm/sec$

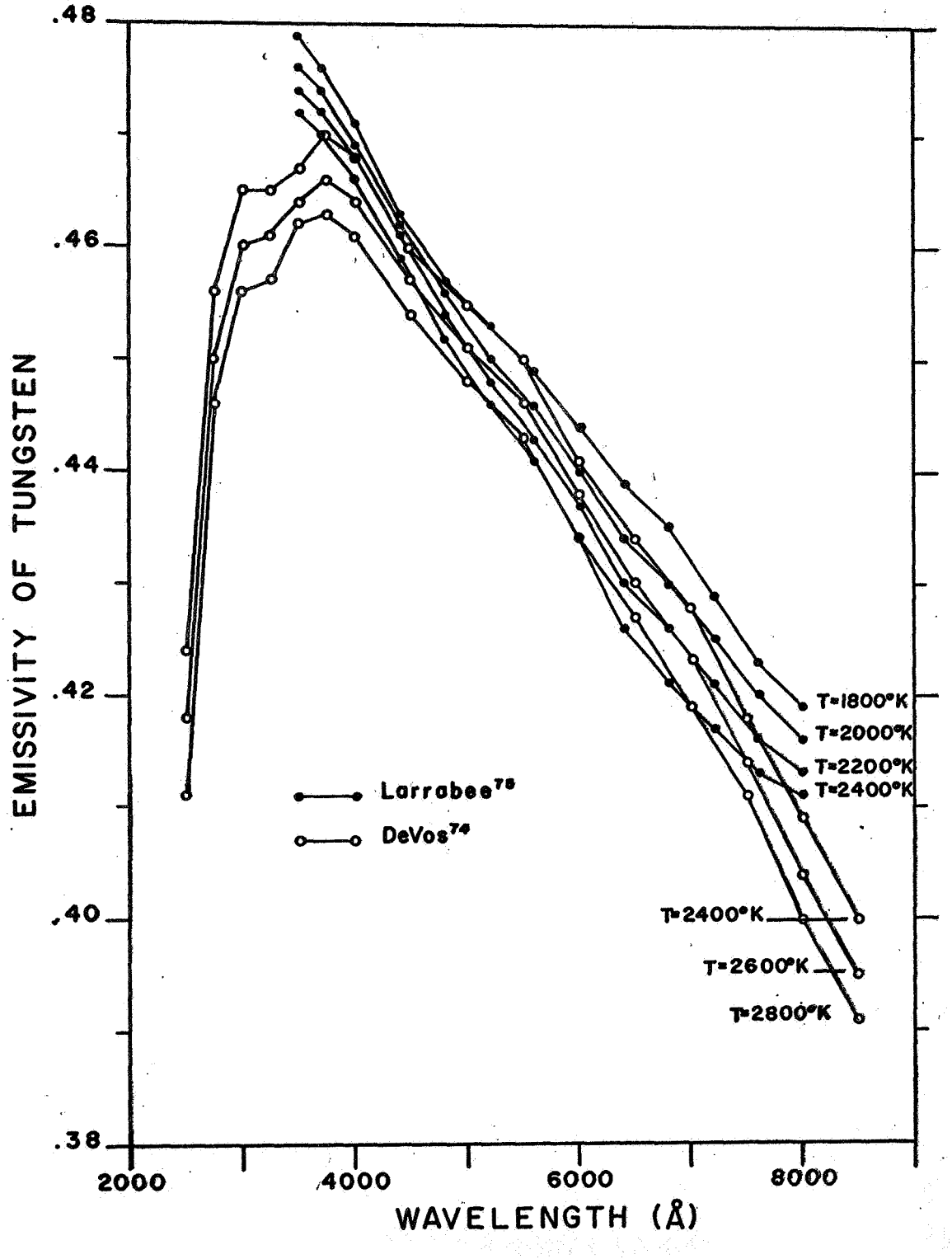

Figure 52. Values of the emissivity of tungsten used in calculating $B(\lambda)$.

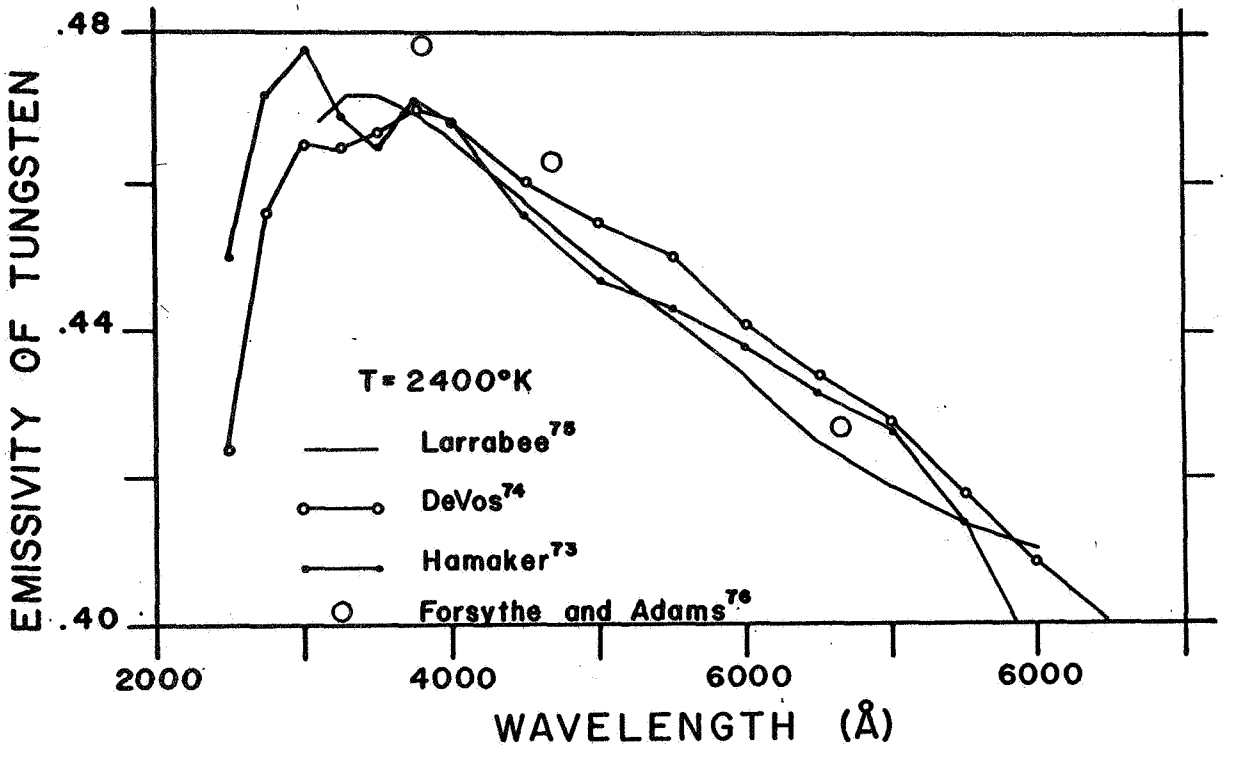

Figure 53. Various determinations of $\varepsilon(\lambda, 2400°K)$.

distribution becomes

$$W = \frac{C_1}{\lambda^5} e^{C_2/\lambda T} , \qquad (89)$$

and hence

$$\frac{dW}{W} = \frac{C_2}{\lambda T^2} dT . \qquad (90)$$

Letting dT = 5°, T = 2000°, and λ = 5000Å, this gives a percentage error of 3.5 percent. Thus in these two factors, we have upwards of 5 percent error in the absolute calibration when using the calculated $B(\lambda,T)$.

The most convenient method of using the tungsten ribbon lamp utilizes a magnesium oxide screen. The lamp is placed in a light tight housing and a quartz lens is used to focus an image of the filament on a fresh MgO screen (Figure 54). The proper angle for viewing the filament is assured by aligning the notch on the filament with an arrow etched on the back of the glass envelope of the lamp.

The photon flux through the aperture of area A at the lens from a small area a on the filament is given by

$$\phi = B(\lambda,T)\ A\ a/d^2 . \qquad (91)$$

This flux is focused on the screen over an area $(\frac{D}{d})^2 a$ and rescattered over a hemisphere about the screen. Again, the photons are preferentially scattered in the forward direction, so by viewing the screen normally, it has a surface brightness of

$$B_S = \frac{\phi}{\pi} \tau_Q(\lambda) \frac{d^2}{D^2 a} R(\lambda) \cos\theta , \qquad (92)$$

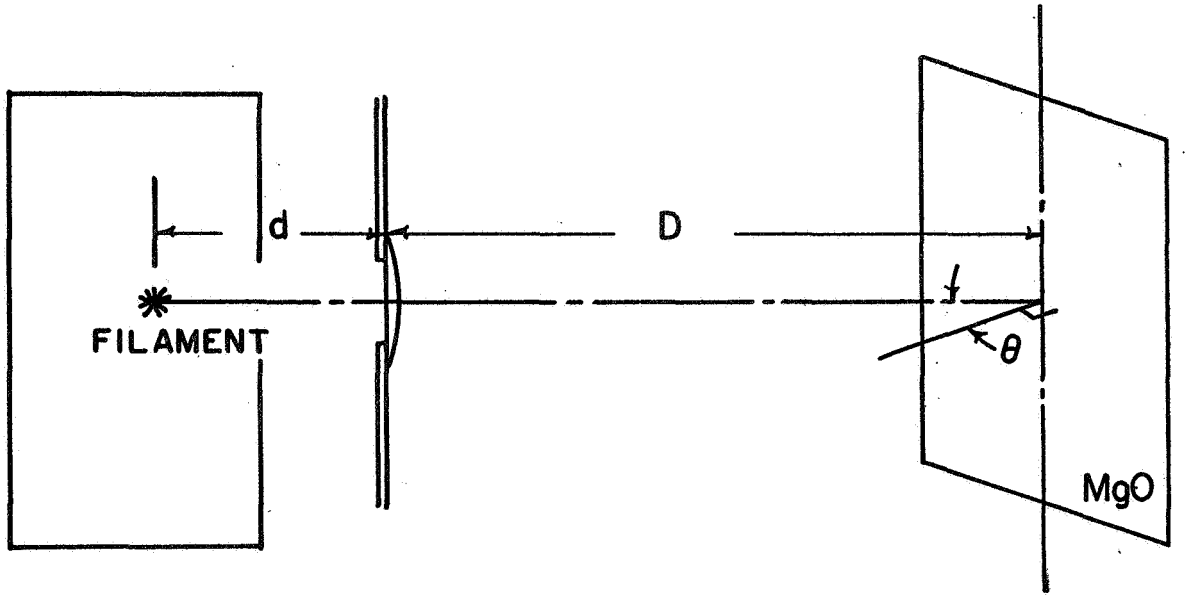

Figure 54. Standard lamp set up for use with a MgO screen.

where $R(\lambda)$ is the reflectivity of fresh MgO (Figure 55) and θ is the angle of incidence of the flux ϕ. Combining the above two equations

$$B_S(\lambda,T) = \frac{B(\lambda,T)_\perp}{\pi D^2} A \tau_Q(\lambda) R(\lambda) \cos \theta \quad . \qquad (93)$$

At this point it should be mentioned that the calibration is only for a very small portion of the filament described by the calibration sheet. Variations along the filament are not insignificant[77] and, as much as possible, only the proper portion of the filament image should be used for the calibration.

If the aperture is very small, diffraction losses can occur. Using simple diffraction theory, considering a monochromatic source at wavelength λ, and an aperture of diameter d, the radius of the first minimum seen on a screen distance D from the aperture is about $\lambda D/2d$. If the dimension of the image formed is large compared to the size of the diffraction pattern, there is no significant error.

The screen is prepared by burning magnesium ribbon onto a suitable surface such as glass or aluminum sheet. After the first uniform coat is put on, it is smudged and more magnesium is burned uniformly over the surface until no contrast is visible at the edges of the smudge. This method is used since the human eye response to contrast is much greater than its absolute response.

When the field of view of the photometer being calibrated is filled by the desired portion of the image on the screen, the photometer sees the surface brightness $B_S(\lambda,T)$ independent of its viewing angle.

This is because while $B_S(\lambda,T)$ decreases with the cosine of the viewing angle, the area viewed increases by one over the cosine.

In careful practice, the errors introduced by this method are small and the overall uncertainty of $B_S(\lambda,T)$ is not much bigger than that of $B(\lambda,T)$ itself.

For conversion from the continuum standard source to a line source, it is necessary to look at the two equations derived from Equation 69 in Appendix A. For a line source, this is Equation 77

$$N = \frac{\pi^2 a^2 a'^2}{D^2} \quad Q(\lambda_o)\ \tau^2_{lens}(\lambda_o)\ B_{line}(\lambda_o)\ \bar{\tau}(\lambda_o) \quad ; \quad (77')$$

and for a continuum, it is Equation 72

$$N = \frac{\pi^2 a^2 a'^2}{D^2} \quad Q(\lambda_o)\ \tau^2_{lens}(\lambda_o)\ B_{cont.}(\lambda_o) \quad \Delta\lambda \quad . \quad (72')$$

Thus

$$B_{line} = B_{cont.}(\lambda_o)\ \Delta\lambda/\bar{\tau}(\lambda_o) \quad , \quad (94)$$

keeping in mind the assumptions made in Appendix A to derive the above expressions for N. In practice, this is the procedure followed; but if necessary, more detailed integrations could be done using the complete expression indicated in Appendix A.

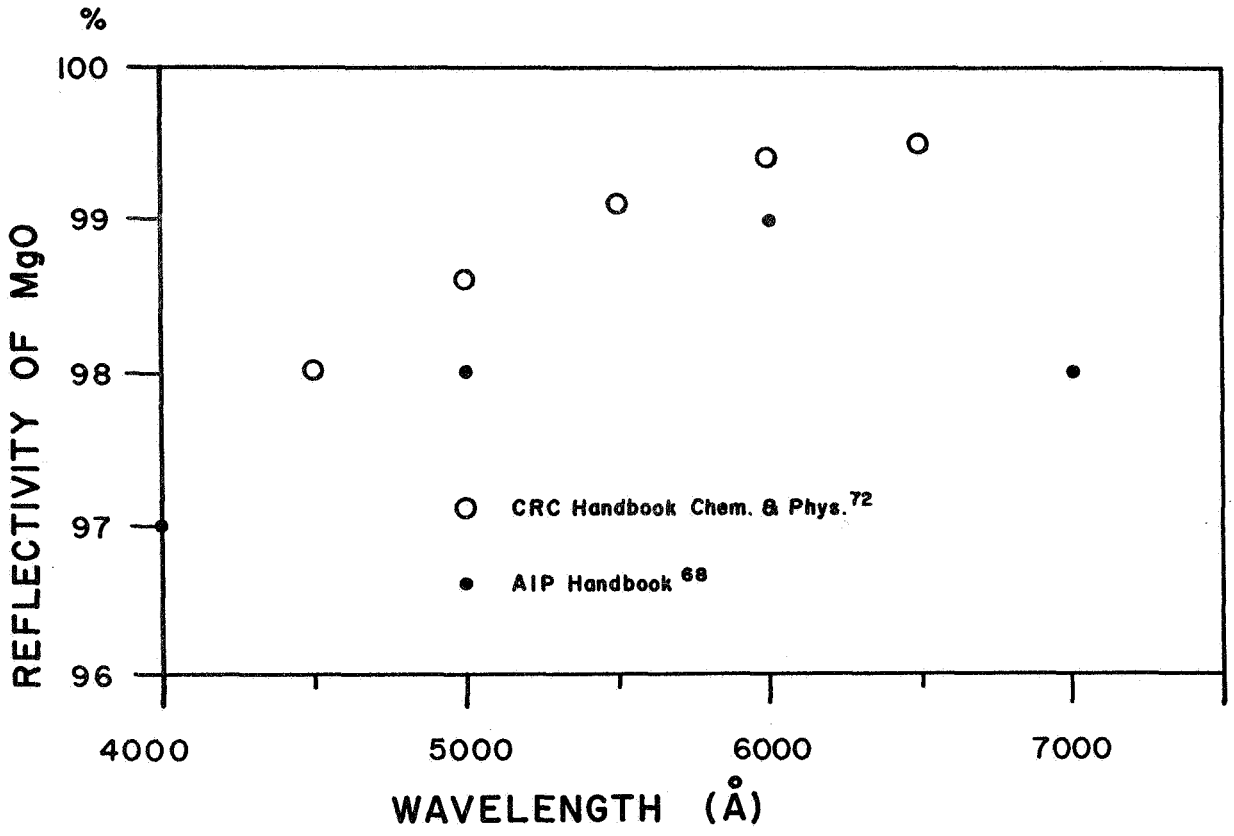

Figure 55 Reflectivity of MgO.

REFERENCES CITED

1. Chapman, S. In Aurora and Airglow. Ed. by B. M. McCormac. p. 15. New York: Reinhold Publishing Corporation, 1967.

2. Ångström, A. J. Spectrum des Nordlichts. Pogg. Ann. 137:161-163, 1869.

3. Babcock, H. D. A Study of the Green Auroral Line by the Interference Method. Astrophys. J. 57:209-221, 1923.

4. McLennan, J. C. and G. M. Shrum. On the Origin of the Auroral Green Line 5577Å and other Spectra Associated with Aurora Borealis. Proc. Roy. Soc. A108:501-512, 1925.

5. Vegard, L. Photographische Aufnahmen des Nordlichtspektrums mit einem Spectrographen von grosser Dispersion. Phys. Z. 14:677-681, 1913. A further list of his auroral papers is given by Chamberlain.[46]

6. Bates, D. R. The Intensity Distribution of the Nitrogen Band Systems Emitted from the Earth's Upper Atmosphere. Proc. Roy. Soc. A196:217-250, 1949.

7. Seaton, M. S. Hartree-Fock Equations for Continuous States with Applications to Electron Excitation of the Ground Configuration Terms of OI. Trans. Roy. Soc. (London) A245:469, 1953.

8. -----. Excitation Processes in the Aurora and Airglow; 2. Excitation of Forbidden Atomic Line in High Latitude Aurorae. J. Atmosph. Terr. Phys. 4:295-313, 1954.

9. -----. In The Airglow and the Aurorae. Ed. by E. B. Armstrong and A.Dalgarno. pp. 289-301. London: Pergamon Press. 1956.

10. -----. Oxygen Red Lines in the Airglow; II. Collisional Deactivation Effects. Astrophys. J. 127:67-74, 1958.

11. Hunten, D. M. and M. B. McElroy. Quenching of Metastable States of Atomic and Molecular Oxygen and Nitrogen. Rev. Geophysics 4:303-328, 1966.

12. Fastie, W. G., H. Crosswhite, and T. Markham. Ann. Geophys. 17:109, 1961.

13. Crosswhite, H., E. C. Zipf, and W. G. Fastie. Far-Ultraviolet Auroral Spectra. J. Opt. Soc. Am. 52:643, 1962.

14. Isler, R. C. and W. G. Fastie. An Observation of the Lyman-Birge-Hopfield System in an Aurora. J. Geophys. Res. 70:2613, 1965.

15. Miller, R. E., W. G. Fastie, and R. C. Isler. Rocket Studies of Far-Ultraviolet Radiation in an Aurora. J. Geophys. Res. 73:3353, 1968.

16. Doering, J. P. and W. G. Fastie. Experimental Measurement of the Energy Distribution of Secondary Electrons in an Aurora. Can. J. Phys. 44:2948-2951, 1966.

17. Dick, K. A. and W. G. Fastie. To be published. 1969.

18. Woodward, C. E. and C. K. Crawford. Development of a Quadropole Mass Spectrometer. Technical Report 194, Laboratory for Insulation Research, Massachusetts Institute of Technology. 1964.

19. Narcisi, R. S. and A. D. Bailey. Miniature Mass Spectrometer for Upper Atmosphere Composition Measurements. Air Force Cambridge Research Laboratory.

20. Mosharrafa, M. and H. J. Oskam. Design and Construction of a Mass Spectrometer for the Study of Basic Processes in Plasma Physics. Armed Services Technical Information Agency, AD 274249. 1961.

21. Paul, W., H. P. Reinhard, and U. von Zahn. Das electrische Massenfilter als Massenspektrometer und Isotopentrenner. Z. Physik 152:143, 1958.

22. Miller, R. E. Private communication.

23. Jacchia, L. G. Static Diffusion Models of the Upper Atmosphere with Emperical Temperature Profiles. Smithsonian Contribution to Astrophysics 8:9:215, 1965.

24. Zipf, E. C., Jr. Rocket Measurements of the Visible Dayglow. J. of Geomagnetism and Geoelectricity 18:301-331, 1966.

25. Walker, J. C. G. Analytic Representation of Upper Atmosphere Densities Based on Jacchia's Static Diffusion Model. J. Atmos. Sci. 22: 462-464, 1965.

26. Bates, D. R. Some Problems Concerning the Terrestrial Atmosphere Above About the 100 km Level. Proc. Roy. Soc. (London) A253: 451-462, 1959.

27. Anderson, A. D. and W. E. Francis. The Variation of the Neutral Atmospheric Properties with Local Time and Solar Activity from 100 to 10,000 km. J. Atmos. Sci. 23:110-124, 1966.

28. Donahue, T. M., T. D. Parkinson, E. C. Zipf, J. P. Doering, W. G. Fastie, and R. E. Miller. Excitation of the Auroral Green Line by Dissociative Recombination of the Oxygen Molecular Ion: Analysis of Two Rocket Experiments. Planet. Space Sci. 16:737-747, 1968.

29. Doering, J. P. Private communication.

30. Dick, K. A. Private communication.

31. McConkey, J. W., J. M. Woolsey, and D. J. Burns. Absolute Cross Section for Electron Impact Excitation of 3914Å N_2^+. Planet. Space Sci. 15:1332-1334, 1967.

32. McConkey, J. W. and I. D. Latimer. Absolute Cross Sections for Simultaneous Ionization and Excitation of N_2 by Electron Impact. Proc. Phys. Soc. 86:463-466, 1965.

33. Holland, R. Private communication to McConkey et al.[31]

34. Pfister, W. Auroral Investigations by Means of Rockets. Space Sci. Rev. 7:642-688, 1967.

35. Green, A. E. S. and C. A. Barth. Calculations of Ultraviolet Molecular Nitrogen Emissions from the Aurora. J. Geophys. Res. 70:1083-1092, 1965.

36. Stolarski, R. S., V. A. Dulock, Jr., C. E. Watson, and A. E. S. Green Electron Impact Cross Sections for Atmospheric Species; 2. Molecular Nitrogen. J. Geophys. Res. 72:3953-3960, 1967.

37. Stewart, D. T. and E. Gabathuler. Some Electron Collision Cross Sections for Nitrogen and Oxygen. Proc. Phys. Soc. A72:287-289, 1958.

38. Benesch, W., J. T. Vanderslice, and S. G. Tilford. Excitation and Photon Emission Rates of the Auroral Nitrogen First Positive Group. J. Atmos. Terr. Phys. 29:251-258, 1967.

39. Broadfoot, A. L. and D. M. Hunten. Excitation of N_2 Band Systems in Aurora. Can. J. Phys. 42:1212-1230, 1964.

40. Shemansky, D. E. and A. Vallance Jones. Type B Red Aurora; the O_2^+ First Negative System and the N_2 First Positive System. Planet. Space Sci. 16:1115-1130, 1968.

41. Benesch, W., J. T. Vanderslice, and S. G. Tilford. Excitation Rates in the Auroral Nitrogen Second Positive Group. J. Atmos. Terr. Phys. 28:431-438, 1966.

42. Henry, R. J. W., P. G. Burke, and A-L Sinfailam. Scattering of Electrons by C, N, O, N^+, O^+, and O^{++}. Contribution #000 from Kitt Peak National Observatory.

43. Smith, K., R. J. W. Henry, and P. G. Burke. Calculations on the Scattering of Electrons by Atomic Systems with Configurations $2p^q$. Phys. Rev. 157:51-68, 1967.

44. Zipf, E. C. Private communication.

45. Garstang, R. H. Energy Levels and Transition Probabilities in p^2 and p^4 Configurations. Monthly Notices Roy. Astron. Soc. 111: 115, 1951.

46. Chamberlain, J. W. Physics of the Aurora and Airglow. New York: Academic Press, 1961.

47. Johnson, C. Y., E. B. Meadows, and J. C. Holmes. Ion Composition of the Artic Ionosphere. J. Geophys. Res. 63:443-444, 1958.

48. Swider, W. Jr., R. S. Narcisi, and T. J. Keneshea. Auroral Ionic Composition at 100-200 km. Am Geophys. Union Trans. Abstract ST170, 1968.

49. Gilmore, F. R. The Rand Corporation, Report Number RM-4034-PR, June 1964.

50. Watson, C. E., V. A. Dulock, Jr., R. S. Stolarski, and A. E. S. Green. Electron Impact Cross Sections for Atmospheric Species: 3. Molecular Oxygen. J. Geophys. Res. 72:3961-3966, 1967.

51. Donahue, T. M. Ionospheric Reaction Rates in the Light of Recent Measurements in the Ionosphere and the Laboratory. Planet Space Sci. 14:31-48, 1966.

52. Smith, D. and C. V. Goodall. The Dissociative Recombination Coefficient of O_2^+ Ions with Electrons in the Temperature Range 180°-630°K. Planet. Space Sci. 16:1177-1188, 1968.

53. Noxon, J. F. Private communication.

54. Young, R. A. Private communication.

55. Hays, P. B. and J. C. G. Walker. Doppler Profiles of the 5777Å Airglow. Planet. Space Sci. 14:1331-1337, 1966

56. Rees, M. H., J. C. G. Walker, and A. Dalgarno. Auroral Excitation of the Forbidden Lines of Atomic Oxygen. Planet. Space Sci. 15:1097-1110, 1967.

57. Omholt, A. and L. Harang. Measurements of the Mean Lifetime of the Metastable ^1S State of the Oxygen Atom in the Upper Atmosphere During Auroral Displays. J. Atmos. Terr. Phys. 7:247-253, 1955.

58. Evans, W. F. J. and A. Vallance Jones. Some Observations of Type B Red Aurora with a Multichannel Photometer. Can. J. Phys. 43:697-704, 1965.

59. Eather, R. H. Short-Period Auroral Pulsations in λ6300 OI. To be published.

60. Akasofu, S. I. Private communication.

61. Dalgarno, A. and S. P. Khare. The 5577/3914Å Intensity Ratio in Auroras. Planet. Space Sci. 15:938-940, 1967.

62. Romick, G. J. and A. E. Belon. The Spatial Variation of Auroral Luminosity; II. Determination of Volume Emission Rate Profiles. Planet. Space Sci. 15:1695-1716, 1967.

63. Brekke, A. and A. Omholt. The Intensity Ratio I(4278)/I(5577) in Aurora. Planet. Space Sci. 16:1259-1264, 1968.

64. Biondi, M. A. Electron-Ion and Ion-Ion Recombination. Ann. Geophys. 20:3446, 1964.

65. Schmeltekopf, A. L., E. E. Ferguson, and F. C. Fehsenfeld. Afterglow Studies of Reactions He^+, $He(2^3S)$, and O^+ with Vibrationally Excited N_2. J. Chem. Phys. 48:2966-2973, 1968.

66. Ferguson, E. E. Ionospheric Ion-Molecule Reaction Rates. Rev. Geophys. 5:305-327, 1967.

67. Strong, J. Concepts of Classical Optics. pp. 253 and 582. San Francisco and London: W. H. Freeman and Company, 1958.

68. American Institute of Physics Handbook. New York: McGraw-Hill Book Company, Inc., 1957.

69. Eather, R. H. Private communication.

70. EMR Photo Electric Division, Preliminary Spec, Model 541E-01-14, March, 1966.

71. Kostkowski, H. J. and R. D. Lee. Theory and Methods of Optical Pyrometry. National Bureau of Standards Monograph 41, 1962.

72. Handbook of Chemistry and Physics, 41st Edition. Cleveland: Chemical Rubber Company, 1959.

73. Hamaker, H. C. Physica 3:561, 1936.

74. DeVos, J. C. A New Determination of the Emissivity of Tungsten Ribbon. Physica 20:690, 1954.

75. Larrabee, R. D. Spectral Emissivity of Tungsten. J. Opt. Soc. Am. 49:619, 1959.

76. Forsythe, W. E. and E. Q. Adams. Radiating Characteristics of Tungsten and Tungsten Lamps. J. Opt. Soc. Am. 35:108, 1945.

77. Leighton, L. G. Characteristics of Ribbon Filament Lamps. Illuminating Engineering LVII:121, 126, 1962.